

2-D MODELING OF SOLID PHASE EPITAXIAL REGROWTH USING LEVEL SET
METHODS

By

SAURABH MORARKA

A DISSERTATION PRESENTED TO THE GRADUATE SCHOOL
OF THE UNIVERSITY OF FLORIDA IN PARTIAL FULFILLMENT
OF THE REQUIREMENTS FOR THE DEGREE OF
DOCTOR OF PHILOSOPHY

UNIVERSITY OF FLORIDA

2010

© 2010 Saurabh Morarka

To my loving family

ACKNOWLEDGMENTS

I would like to acknowledge my advisor Dr. Mark E. Law for his support and encouragement. I was amazed to see the extent to which he was willing to help his students despite having a packed schedule. I feel fortunate to have learnt the intricacies of device and process simulation from him. I also want to thank my committee members Dr. Kevin S. Jones, Dr. Scott E. Thompson and Dr. David P. Arnold for their valuable suggestions in my thesis. This work would not have been possible without the help of Nicholas Rudawski and Sidan Jin who helped me out with transmission electron microscopy (TEM) images. Last but not the least, I'd like to thank all the past and present SWAMP group members for all their support.

TABLE OF CONTENTS

	<u>page</u>
ACKNOWLEDGMENTS.....	4
LIST OF FIGURES	7
ABSTRACT	10
CHAPTER	
1 INTRODUCTION.....	12
1.1 Metal-Oxide Semiconductor (MOS) Transistor	12
1.2 Technological Relevance of Solid Phase Epitaxial Regrowth.....	14
1.3 Motivation	15
2 LITERATURE REVIEW	20
2.1 Planar Solid Phase Epitaxial Regrowth	20
2.1.1 Introduction.....	20
2.1.2 Substrate Orientation Dependence	20
2.1.3 Doping Effect on SPER	22
2.1.4 Stress Effect on SPER.....	24
2.2 Patterned SPER	26
2.2.1 Substrate Orientation Effect and Mask-Edge Defects	26
2.2.2 In-Plane Uniaxial Stress Effect on Patterned SPER	28
2.3 SPER Modeling.....	29
2.3.1 2D Analytical Model.....	29
2.3.2 Atomistic Modeling of SPER	32
3 EXPERIMENTAL AND SIMULATION TECHNIQUES	42
3.1 Material Processing.....	42
3.1.1 Pattern Creation Using Electron Beam Lithography and Reactive Ion Etching (RIE)	42
3.1.2 Ion-Implantation	44
3.1.3 Application of In-Plane Uniaxial Stress	46
3.1.4 Temperature Calibration and Annealing.....	47
3.1.5 Cross-section Transmission Electron Microscopy Sample Preparation	48
3.2 Material Characterization	48
3.2.1 Transmission Electron Microscopy.....	48
3.3 Simulation Techniques	49
3.3.1 Level Set Methods.....	49

4	IMPLEMENTATION OF LEVEL SET METHODS FOR SOLID PHASE EPITAXIAL REGROWTH AND INITIAL RESULTS	62
	4.1 Introduction	62
	4.2 Level Set Implementation.....	62
	4.3 Experiments and Initial Simulations.....	65
	4.4 Summary.....	66
5	ROLE OF CURVATURE PARAMETER IN SOLID PHASE EPITAXIAL REGROWTH OF INTRINSIC SILICON	72
	5.1 Introduction	72
	5.2 Model for SPER Including Curvature	72
	5.3 Curvature Confirming Experiment and Simulation.....	74
	5.4 Interpretation of the Curvature Factor in SPER.....	77
	5.5 Predicting 2D Regrowth Shapes	79
	5.6 Summary.....	81
6	DOPANT EFFECT ON SOLID PHASE EPITAXIAL REGROWTH OF SILICON	88
	6.1 Introduction	88
	6.2 Experiment for Dopant Effect on SPER.....	89
	6.3 Discussion.....	92
	6.3 Linking Diffusion and SPER.....	93
	6.4 1D SPER and Diffusion.....	94
	6.5 2D SPER and Diffusion.....	95
	6.6 Summary.....	96
7	STRESS EFFECT ON SOLID PHASE EPITAXIAL REGROWTH OF SILICON	103
	7.1 Introduction	103
	7.2 Interfacial Roughening During SPER	104
	7.3 In-Plane Uniaxial Stress Experiments	106
	7.4 Simulation and Curvature Effect.....	108
	7.4 Physical Explanation of Curvature Effect	110
	7.5 Summary.....	112
8	SUMMARY AND FUTURE WORK	117
	8.1 Overview of Results.....	117
	8.2 Future Work	119
	LIST OF REFERENCES	124
	BIOGRAPHICAL SKETCH	129

LIST OF FIGURES

<u>Figure</u>	<u>page</u>
1-1 Schematic of a basic n-MOSFET transistor.	18
1-2 Cartoon of a MOS transistor with mask-edge defects.	18
1-3 (a) Mask-edge defects shown in plan-view TEM image, (b) cross-section TEM image of the initial α -c interface that creates defects after SPER.	19
1-4 Boron diffusion in amorphous Silicon (Si) is shown by the yellow line. Significant diffusion at 600 °C for 1 min. implies a high diffusivity ³⁰	19
2-1 Solid Phase Epitaxial Regrowth process	34
2-2 Two-dimensional atomistic model for regrowth ¹³	35
2-3 Band-diagram of amorphous Si and p-type doped crystalline Si.....	36
2-4 Cartoon of a patterned as-implanted amorphous trench region. The interface consists of varying substrate orientations that result in non-isotropic regrowth ¹⁸	37
2-6 TEM images showing patterned amorphous regrowth.....	38
2-7 TEM images representing patterned SPER for two Si substrates.....	39
2-8 Cartoon (based on TEM images ¹⁵) showing SPER of a sinusoidal shaped as-implanted amorphous interface.....	40
2-9 TEM images of SPER of patterned trench α -c Si interface under stress	41
3-1 Scattering effects during e-beam lithography. Figure shows the forward scattered electrons (FSE) and the back scattered electrons (BSE) ⁶⁵	53
3-2 E-beam lithography for patterned regions.....	54
3-3 A diagram of a common Reactive Ion Etch (RIE) setup. An RIE consists of two electrodes (1 and 4) that create an electric field (3) meant to accelerate ions (2) toward the surface of the samples (5). ⁶⁶	55
3-5 Schematic of a basic ion-implantation system. ⁵³	57
3-6 Cross-sectional Transmission Electron Microscopy image of an as-implanted Si sample. ...	57
3-7 Schematic of the apparatus used to induce and measure in-plane uniaxial stress in Si wafers ^{37,53}	58

3-8 Schematic of the tube furnace apparatus used for annealing and the method of temperature calibration ⁵³	58
3-9 Figure shows the initialization of the Level Set higher order function ϕ as a signed distance to the interface ⁵⁸	59
3-10 Pictorial view of level set function $\phi(x, y, t)$ on the right. Left figure shows the interface at x,y at time $t=t_1$ where $\phi(x, y, t_1) = 0$. The position of the interface is embedded in the function ϕ ⁵⁸	59
3-11 Time evolution of the level set function and extracted interface at different times. The interface is circular and expanding with a fixed isotropic velocity ⁵⁸	60
3-12 Ability of Level Set method to merge two disjoint regions :(a) level sets at $t=0$. (b) level sets at $t=1$ ⁵⁸	61
4-1 As-implanted amorphous-crystalline interface showing various substrate orientations and the surface angle (θ) for orientation dependent factor $f(\theta)$	68
4-2 Simulation of regrowth using Level Set Methods with isotropic velocity ¹⁴ . Contours represent the position of α -c interface at different times of regrowth.	69
4-3 The normalized SPER velocity, $f(\theta)$ ¹⁴ , as a function of the substrate orientation angle from [001] towards [110], θ , as measured by Csepregi <i>et al.</i> ¹³	69
4-4 Simulation of regrowth with orientation dependence included (velocity from Equation 4-3). Contours represent the α -c interface at different times of regrowth. Region outside the contour is crystalline and inside is amorphous.	70
4-5 The observed and simulated 2D SPER process in a structure with α -c interfacial pinning at the surface at $T = 500$ °C.	71
5-1 The observed and curvature-included simulated 2D SPER process in a structure with α -c interfacial pinning at the surface at $T = 500$ °C.....	82
5-2 Shows cartoons for creating a structure without α -c interfacial pinning.....	83
5-3 The observed and curvature included simulated 2D SPER process in a structure without α -c interfacial pinning at the surface at $T = 500$ °C	84
5-4 2D SPER shapes showing no dependence on temperature in a structure without α -c interfacial pinning at the surface.	85
5-5 Cartoon depicting the ledge theory argument for the 2D SPER of a structure without α -c interfacial pinning.	85
5-6 The effect of initial α -c interface curvature near the corner region on the level set simulations using both regrowth orientation and interfacial curvature dependence.....	86

5-7	The effect of initial α -c interface width-to-depth (W/D) ratio on the regrowth shapes for 2D SPER using level set simulations.....	87
6-1	As-implanted α -c interface of Si for semi-insulating, n-type and p-type samples. Si_3N_4 mask patterned to get a patterned α -c interface.	98
6-2	The observed 2D SPER process at $T=500\text{ }^\circ\text{C}$ with dopants.....	99
6-3	Figure shows the effect of dopants on Csepregi's ¹³ SPER data. Experimental results suggest shifting up of the data due to the isotropic SPER dopant enhanced velocity.	100
6-4	Level set simulations showing the effect of the curvature parameter “A” on the shape of regrowth for $t=5\text{ h.}$ and $T=500\text{ }^\circ\text{C}$	100
6-5	1D diffusion of Boron during SPER. The figure shows the SIMS profile of Boron as-implanted and after annealing at $T=550\text{ }^\circ\text{C}$ for $t=30\text{ mins.}$ ^{30,82}	101
6-6	Figure shows the effect of 2D SPER on dopant profile.....	102
7-1	XTEM images of SPER under in-plane uniaxial compression.....	113
7-2	Level set simulations of SPER with varying curvature factor A. (a), (b), (c), (d) represent SPER after 1h. at $525\text{ }^\circ\text{C}$ with values of $A = 0, 1.5\text{e-}7, 2\text{e-}7, 4\text{e-}7\text{ cm}$ respectively.....	113
7-3	Weak beam dark field (WBDF)-XTEM images of the stress-influenced SPER process in As-doped specimens ⁵³	114
7-4	XTEM images of patterned SPER under no external stress.....	115
7-5	XTEM images of patterned SPER under in-plane uniaxial stresses.....	115
7-6	Level set simulations of SPER for matching the observations shown in Figure 7-5 by varying curvature factor A	116
8-1	XTEM images of SPER at $525\text{ }^\circ\text{C}$ for 4h. under uniaxial in-plane compression into the page of the figure (or parallel to lines $\sigma_{22} \approx -300\text{MPa}$).....	122
8-2	XTEM images of SPER under uniaxial in-plane stresses into the page of the figure (or parallel to lines $\sigma_{22} \approx \pm 300\text{MPa}$)	123

Abstract of Dissertation Presented to the Graduate School
of the University of Florida in Partial Fulfillment of the
Requirements for the Degree of Doctor of Philosophy

2-D MODELING OF SOLID PHASE EPITAXIAL REGROWTH USING LEVEL SET
METHODS

By

Saurabh Morarka

May 2010

Chair: Mark E. Law

Major: Electrical and Computer Engineering

Solid Phase Epitaxial Regrowth (SPER) has a huge technological relevance in the formation of source/drain regions of MOS devices. Source/drain regions are patterned amorphous regions that need to be modeled in 2D/3D. The macroscopic velocity, v , of an interface between amorphous (α) and crystalline (c) phases (also referred to as the SPER or regrowth front/interface) is known to be a thermally-activated process with an activation energy of ~ 2.7 eV. Additionally, SPER is affected by the crystal orientation of α -Si/c-Si interface, impurities, and applied mechanical stress.

In this work, level set model was set up to model SPER. The α -c Si interface propagation velocity was computed using a substrate orientation dependent velocity term along with a local interface curvature term. This velocity was fed to the advection equation of level set formulation for simulating SPER. Simulations were checked against observed TEM images of SPER of ~ 120 nm deep, patterned amorphous trench at $T = 500^\circ \text{C}$ and at $t = 1$ h, 2 h and a good matching was observed for all times.

More experiments were done to confirm the presence of interface curvature term on SPER using structures containing both convex and concave interfaces. During SPER at $T = 500^\circ \text{C}$, the concave interface sharpened while the convex interface flattened out. The simulations were

successfully able to predict the shapes of α -c Si interface during SPER at all times. The experiment when repeated at a higher temperature of 575 °C resulted in similar regrowth shapes implying a negligible effect of temperature on the curvature factor.

Effect of n and p dopants on patterned SPER was studied in an experiment with very low resistivity (~ 0.003 ohm-cm) wafers. The results showed the isotropic nature of dopant enhancement (both p and n type) on SPER, something that extends the generalized Fermi level shifting theory (for dopant enhancement of SPER) for all substrate orientations. The results also helped de-link the curvature effect from the electronic effect of dopants on SPER. Models for dopant diffusion in amorphous Si were linked to the SPER model to get accurate dopant profile after regrowth.

Finally, the effect of uniaxial stress on patterned SPER was studied in an experiment where stresses (both tensile and compressive) upto ~ 1.3 GPa were applied. The experiments showed the strong effect of in-plane uniaxial compression on regrowth shapes that resulted in the formation of mask-edge defects. The results for the tensile case were found to be exactly the same as no-stress case, something that was observed previously for planar regrowth of (001) Si. The curvature factor was able to encapsulate the effect of external in-plane uniaxial stress and simulations matched up to the observed results. A more physical understanding of the curvature factor was explored using simulations with rough α -c Si interfaces. Ultimately, a complete 2-D model for patterned SPER was developed using level set methods for interface propagation.

CHAPTER 1 INTRODUCTION

1.1 Metal-Oxide Semiconductor (MOS) Transistor

MOS transistor has revolutionized the electronics circuits for low power and faster speeds. The scaling of the transistor size using MOS has led to circuits becoming faster and denser. The scaling of MOS transistor has been driving the semiconductor industry for four decades. As expressed in an observation from Gordon Moore¹, the transistors per square inch has been doubling every two years ever since the integrated circuits were invented. The MOS transistor is a field effect transistor (hence called MOSFET) where the current through the transistor depends upon the field in the channel region. It is unipolar meaning only one carrier is responsible for conduction. n-MOSFET has electrons as carriers for conduction while p-MOSFET has holes.

A basic structure of n-MOSFET transistor is shown in Figure 1-1. As Figure 1-1 shows, the transistor has four terminals: gate, source, drain and body. A positive gate terminal's voltage with respect to the source above a certain "threshold" voltage creates a conducting channel below the gate oxide. The conducting channel is composed of electrons for a p-body, hence it is called inversion of the channel. When a positive bias is applied on the drain side, it sweeps the carriers in the channel and there is conduction of current. It is observed that with decreasing channel length, the field in channel increases and the on-current increases. This is known as scaling.

Constant Electric field scaling and constant voltage scaling are the two ways scaling of transistor can be done. In constant field scaling, the applied voltages are scaled along with the device dimensions (most importantly "L", the channel length) so that the field in the channel stays constant. This assures that that reliability of the scaled devices does not degrade with scaling. It increases the circuit speed and reduces the power dissipation. However, the fact that

the shape of the field pattern in the channel can only be preserved if the voltage is kept constant (because the built-in potential of the source junction is independent of scaling), hence called constant voltage scaling. Constant voltage scaling increases the power dissipation though, that is a major challenge. Hence, in practice a combination of the two has been used.

Silicon has been the choice of semiconductor for the MOSFETs especially because of the presence of a stable oxide (SiO_2) that had very good physical and electrical properties for MOSFET operation. SiO_2 is used as the gate oxide for its superior interface with Si that has very less traps and recombination sites. Reducing SiO_2 thickness is one of the requirements of scaling (SiO_2 acts as a capacitor for charge build-up in the channel). However, gate leakage through the SiO_2 has given rise to high-K dielectrics like HfO_2 that have a higher dielectric constant and therefore results in more capacitance for same physical thickness.

Scaling of the MOSFET has also required the source and drain highly doped regions to become shallower and have higher dopant activation. Shallower source/drain regions are required to reduce the leakage current (during off condition). Higher dopant activation is important since, only a part of the implanted dopant becomes active and takes part in the conduction process. This has led to a search for more innovative thermal processing steps like rapid thermal annealing, flash annealing or laser annealing. These annealing processes use high temperatures (up to 1300°C) for very short times (~ 1 millisecond) that serve to create high dopant activation and ultra-shallow junctions².

Apart from scaling, applying stress to the MOSFET channel has been found to increase carrier mobility (μ) and thus boost the current drive of the transistor³. Liners of Si_3N_4 and related compounds (e.g. Oxynitrides) have been found to possess high stress depending on the way the thermal processing grows these liners. n-MOSFETs require tensile stress liners for

improving their current drive while p-MOSFETs require compressive stress liners⁴. p-MOSFETs have also utilized the addition of Ge to form $\text{Si}_x\text{Ge}_{1-x}$ source/drain regions to provide additional compressive stress in the channel⁵.

1.2 Technological Relevance of Solid Phase Epitaxial Regrowth

Solid Phase Epitaxial Regrowth (SPER) for the element Si is the process of converting amorphous Si into crystalline Si by thermal processing. The epitaxially regrown Si has the same substrate orientation as that of its seed. The process is interchangeably known as solid phase epitaxy, solid phase growth and solid phase epitaxial recrystallization.

SPER finds its technological relevance in the formation of source/drain regions of MOSFET. For SPER to happen, the crystalline source/drain Si regions are intentionally bombarded with high-energy ions to cause lattice damage to an extent that the Si become amorphous. This is followed by ion-implantation of dopant atoms like B, As or P. When the dopants are implanted in a crystalline Si, they have a tendency to channel through the lattice and form a tailing profile that is deeper than anticipated. This process is called channeling^{6,7}. Thus, implanting dopants in amorphous Si reduces channeling since the lattice structure ceases to exist in amorphous Si. This is followed by a thermal processing step to regrow the broken lattice and hence, helps in shallower junctions for the dopants. The high dose of dopants required in source/drain regions causes some heavier dopants like As to amorphize the Si without the need for pre-amorphizing implant. Thus, SPER in such cases becomes unavoidable.

SPER is also known to increase the active dopant concentration that is essential for scaled MOS transistors. The possible reason for increase in active dopant concentration is that SPER involves rearrangement of Si lattice and the dopants get incorporated during this rearrangement. The dopant incorporation is more than the solid-solubility of those dopants at the temperature SPER occurs⁸⁻¹⁰.

As mentioned in section 1.1, stress is helpful in increasing carrier mobility that results in higher on-state current. SPER has been believed to be a reason for a phenomenon called Stress Memorization. Stress memorization occurs when a pre-amorphized polysilicon gate recrystallizes under external stress from liner^{11,12}. The stress transferred from the liner through the polysilicon into the channel is retained even after the removal of the liner material. It is helpful for current enhancement in n-MOSFET devices since an out of plane stress is created that affects n-MOSFETs much stronger than p-MOSFETs.

1.3 Motivation

SPER has been studied in great detail as a bulk process where the growth front advances only in one substrate orientation. However, since SPER is used for the formation of source and drain regions in scaled MOS devices, it has to be viewed as a multidimensional process (patterned amorphous regrowth). During the regrowth of a patterned amorphous region, the advancing regrowth front velocity is temporally dependent on the immediate regrowth shape. Since, the regrowth is non-isotropic for different substrate orientations^{13,14}, it is a non-trivial problem to solve analytically; hence simulations are necessary to get the right regrowth shapes.

Previous attempts¹⁵ to model and simulate the orientation dependence of SPER in the patterned amorphized regions have been made, but have not been extended to initial α -c interfaces with any shape other than rectilinear. This somewhat limits the capability of prior models in predicting SPER evolution for different types of initial α -c interfaces and makes it difficult to gain further insight into the nature of regrowth.

In particular, predicting and modeling the evolution of 2D SPER in patterned amorphized regions is very important since mask edge defects are known to occur during this process¹⁶⁻²⁶. It is believed that mask edge defects are caused by the regrowth dependence on substrate orientation¹⁶⁻²⁶. Specifically, since the [001] and [110] directions are much faster than the [111]

direction, a portion of the α -Si near the [111] fronts can become encompassed and “pinched off” from the remaining α -Si layer via the regrowth interface collapsing upon itself. Saenger *et. al.*¹⁵ showed that the defects were created along $\langle 111 \rangle$ -type directions in both (001) and (011) wafers which suggests that impingement of the [111] front is primarily responsible for mask edge defect formation. These defects are deleterious to the device performance as they increase the leakage current. Figure 1-2 shows the presence of mask edge defects in a transistor structure. Figure 1-3(a) shows the plan-view of mask-edge defects for an as-implanted α -c interface shown in Figure 1-3(b).

Apart from substrate orientation dependence, the SPER velocity is affected by the presence of dopants²⁷. The experiments to observe the effect of dopants on regrowth have been mostly planar (001) samples^{28,29}. The dopant related enhancement of regrowth rate has been known to be an electronic process because both p and n-type dopants increase the rate when present separately and there is no enhancement when both are present together²⁷. The generalized Fermi level shifting method gives the dopant enhancement of SPER velocity^{28,29}. However, the validity of the model has not been experimentally tested in orientations other than (001) for Si.

Boron has an extremely high diffusivity in amorphous Si when compared to crystalline Si^{30,31} (Figure 1-4). This results in the diffusion of Boron competing with simultaneously occurring SPER. The final profile of Boron is a result of the time Boron spends in the amorphous Si. FLOOPS (Florida Object Oriented Process Simulator)³² has the capability of simulating ion-implantation and dopant diffusion. Thus, an implementation of SPER in FLOOPS can leverage these simulation capabilities to simulate accurate Boron profile after SPER.

Effect of uniaxial stress on planar SPER has been studied in great detail^{21,33-40}. Prior experiments have shown that hydrostatic compression and uniaxial compression (out of plane)

^{41,42} lead to an enhancement in SPER velocity for planar (001) Si α -c interface. Biaxial (in-plane) and uniaxial (in-plane) compression lead to a reduction in SPER velocity^{37,41}. Experiments done for studying the effect of stress on patterned amorphous regions have revealed that in-plane tension can result in lesser mask-edge defects^{19,22}. It has been attributed to the difference in enhancements of the side (011) and bottom (001) fronts velocity due to tension. These experiments use stresses upto ~ 250 MPa²². However, stresses in actual MOS transistors go as high as ~ 1 GPa. Thus, it would be interesting to see the effect of higher stresses on SPER.

A new SPER model can use the stress simulation capability of FLOOPS to get accurate shapes during regrowth. Prior models included an activation volume tensor to compute stress effect on SPER velocity that was based on a scattered data set. The new theory that includes nucleation and migration mechanism for SPER has invalidated the previous results that resulted in that activation volume tensor^{38,41}. Hence, a new model for SPER with correct stress effect is required.

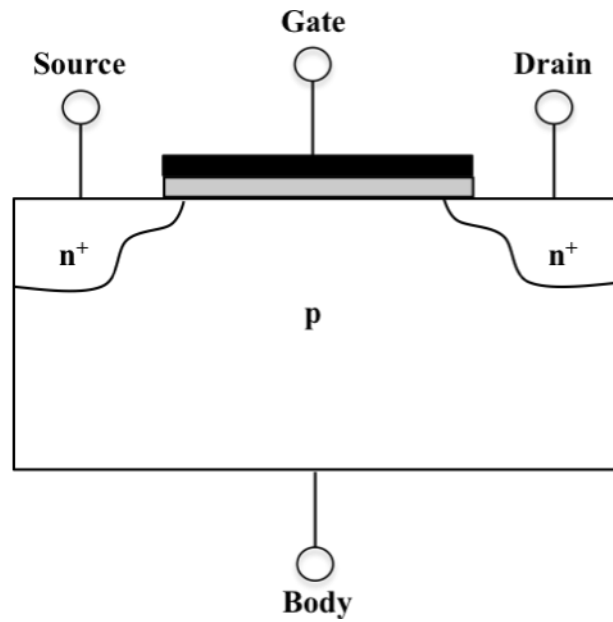


Figure 1-1. Schematic of a basic n-MOSFET transistor.

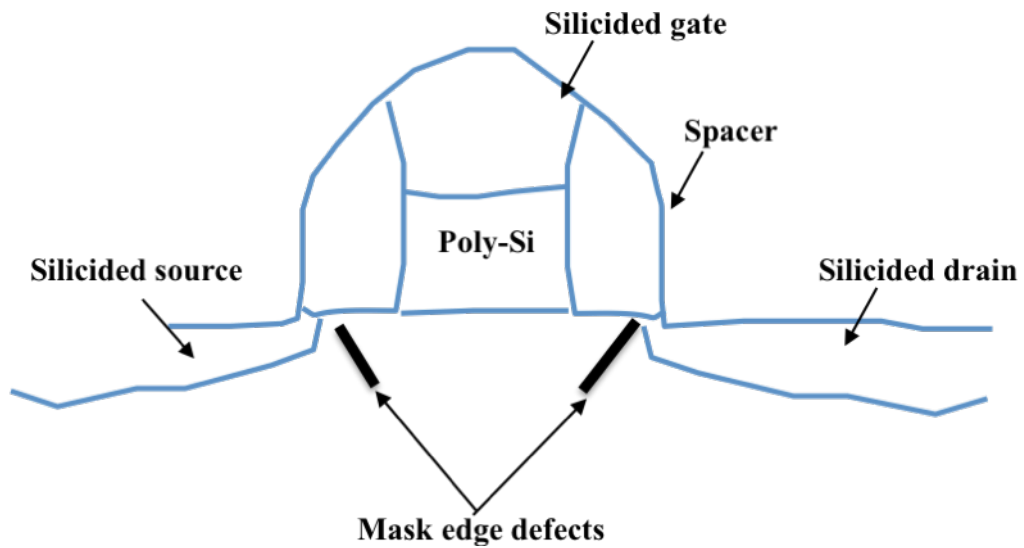


Figure 1-2. Cartoon of a MOS transistor with mask-edge defects.

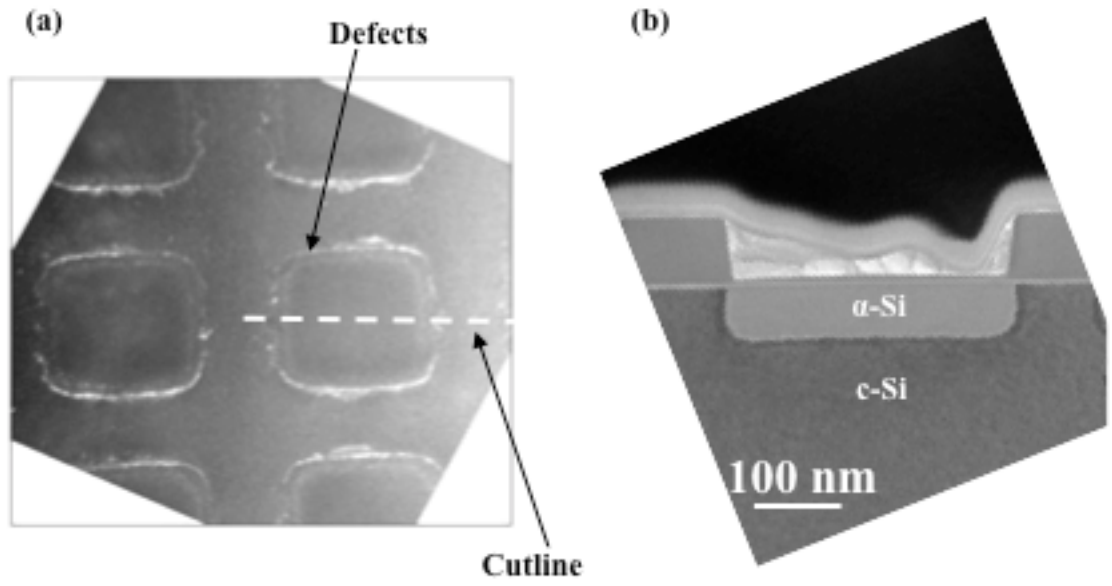


Figure 1-3. (a) Mask-edge defects shown in plan-view TEM image, (b) cross-section TEM image of the initial α -c interface that creates defects after SPER.

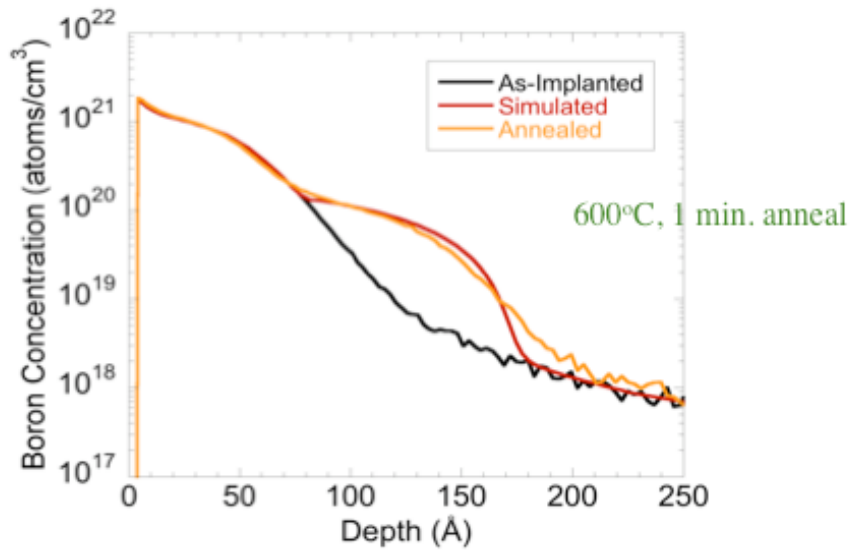


Figure 1-4. Boron diffusion in amorphous Silicon (Si) is shown by the yellow line. Significant diffusion at 600 °C for 1 min. implies a high diffusivity³⁰.

CHAPTER 2 LITERATURE REVIEW

2.1 Planar Solid Phase Epitaxial Regrowth

2.1.1 Introduction

Solid Phase Epitaxial Regrowth (SPER) for Si refers to the conversion of amorphous Si into crystalline Si when thermally activated. The regrown amorphous Si has the same substrate orientation as that of the seeding crystalline Si (Figure 2-1). The activation barrier for SPER for intrinsic Si is known to be ~ 2.7 eV²⁷. It is very interesting to note that the Si-Si bond energy is ~ 2.5 eV⁴³. Thus the regrowth mechanism has been suggested to be a mere remaking of new Si-Si bonds. The free energy of crystalline silicon is less than amorphous silicon, which is the driving force for the SPER. There have been a lot of theories about the atomistic defect that is responsible for the regrowth of the amorphous material into crystalline. Lu *et al.*⁴² have shown that dangling bonds or kink sites (special case of dangling bonds) at the amorphous-crystalline (α -c) interface are the two plausible mechanisms (defects) that govern regrowth. The other defects that include interstitials, vacancies etc. have been studied for regrowth governing mechanisms. However, their rate of creation and transport to the (α -c) interface does not match up with the measured activation energy of SPER. Hence, they have been rejected as the possible mechanisms governing SPER. SPER is known to be a process of bond rearrangement at the α -c interface. Thus, any dependence of SPER on doping, stress or substrate orientation needs to be known only at the α -c interface during regrowth.

2.1.2 Substrate Orientation Dependence

Substrate orientation dependence has a strong influence on SPER. Figure 2-2(a) shows an atomistic view of SPER process on a (001) Si substrate (cross-sectional view is shown in the figure with $\langle 110 \rangle$ direction into the plane of the shown image). Csepregi *et al.*¹³ suggested that

every atom in the amorphous phase requires two bonds in the crystalline region to be considered as regrown. Figure 2-2(a) clearly shows how atom *A* would be the first to regrow. Regrowth of atom *B* is dependent on *A* being regrown. Thus *A*'s regrows first followed by *B*, then *C* and finally *D*. It is interesting to note that the 2-dimensional image shows the position of *D* and *B* to be in equal proximity to *A*. However, because of the face-centered cubic (FCC) structure of Si, *D* takes longer than *B* to regrow. This forms the basis for the orientation dependence of SPER in Si. Csepregi's data¹³ shows that regrowth velocity in $\langle 001 \rangle$ direction is almost thrice that of $\langle 110 \rangle$ direction and ~25 times bigger than in $\langle 111 \rangle$, as shown in Figure 2-2(b). The data was collected by regrowing planar substrates with orientations ranging from (001) upto (110) (a full 90° tilt).

Csepregi's model¹³ encapsulates the orientation dependence in a sinusoidal function with the angle calculated from the (111) front. The model predicts the substrate orientation effect on SPER from (001) to (111) range correctly. However, it predicts a zero velocity (that implies no regrowth possible) for (111) substrate that is not correct. Moreover, it fails to explain the increasing regrowth rate for the substrate orientations from (111) to (110).

A more complicated model to understand the orientation dependence on regrowth was given by Narayanan *et al.*⁴⁴. In the model, Narayanan shows a 3D image of the crystal structure for the three main substrate orientations (001), (110) and (111). The model suggests the completion of a hexaring in the (111) plane as the basis for the conversion of amorphous into crystalline silicon. The formation of hexaring is shown to be much easier in (001) when compared to (110) and (111) substrates. Every atom on these substrates faces a number of combinations in which it can either join or not join a crystalline site⁴⁴. These available combinations are much more for (001) substrates followed by (110) and then (111). Hence, the

effect of substrate orientation on SPER was explained for all the orientations ranging from (001) to (110).

2.1.3 Doping Effect on SPER

Dopants (both electrically active and inactive) have been known to have a significant impact on the SPER rate^{27-29,45-47}. Olson *et al.*²⁷ showed the effects of various dopants on regrowth rate for bulk (001) substrates using Rutherford Backscattering Mechanism (RBS). Dopants of the III and V group of periodic table like B, P and As increase the regrowth rate significantly²⁷. These electrically active dopants are mostly used for the formation of highly doped p and n types source/drain regions for CMOS devices. It has also been shown that if equal concentrations of p-type and n-type dopants are present in Si, the regrowth rate returns to its intrinsic value²⁷. Thus, the effect of electrically active dopants on SPER is believed to be an electronic process. The regrowth rate enhancement from Boron can reach up to ~30 times the intrinsic rate, while for Phosphorus can reach up to ~8 times for $T=625^{\circ}\text{C}$ ²⁷.

Since the electrically active dopants have been known to affect the Fermi level of Si, a generalized Fermi level shifting (GFLS) model of dopant enhanced SPER was proposed^{28,29,47}. The theory suggests the presence of “kink-like” growth sites that possess electronic energy levels within the band gap. The Fermi level in amorphous silicon is assumed to be pinned at the mid band. For aligning of the Fermi levels, the bands on the crystalline side bend, as shown in Figure 2-3. The regrowth velocity is assumed to be proportional to the concentration of the “kink-like” growth sites²⁹. For intrinsic Si, the regrowth rate is proportional uncharged kink sites C_0 (independent of doping) concentration, since the charged kink sites (C_i) are negligible. However, for doped semiconductor, regrowth rate is proportional to the sum of uncharged kink sites C_0 (independent of doping) and the charged kink sites (C_p). The ratio of charged sites to

uncharged sites at the growth interface is given by the Fermi-Dirac statistics that becomes Maxwell-Boltzmann approximation for dilute dopant concentration²⁹.

$$\frac{C_p}{C_0} = g \exp\left(\frac{E_n^p - E_F}{kT}\right), \quad (2-1)$$

where E_n^p is the energy level at the growth interface of a positively-charged defect, E_F is the Fermi level of the material, and g is the degeneracy factor. In case of lightly B-doped material,

$$E_F = E_F^i - kT \ln\left(\frac{C_B}{n_i}\right), \quad (2-2)$$

where E_F^i is the Fermi level in intrinsic material, C_B is the B concentration at the growth interface and n_i is the intrinsic carrier concentration at T. Combining equations (2-1) and (2-2) and under the approximation that charged kink sites in intrinsic Si are much less than uncharged kink sites,

$$v = v_i \left[1 + \frac{C_B}{n_i} g \exp\left(-\frac{E_F^i - E_n^p}{kT}\right) \right], \quad (2-3)$$

where v_i is the intrinsic value of v at T ²⁹. A similar expression can be derived for n-type doping. The key point of the above equation is that v should increase linearly with the concentration of the dopant (till the dopant is active). This has been confirmed by experiments⁴⁵.

Electrically-inactive impurities like H, O, C and N tend to reduce the regrowth velocity⁴⁶. The notion is that these impurities do not affect the Fermi level of the semiconductor and do not affect the nucleation kinetics. However, they slow down the migration kinetics much more than the electrically-active impurities do because of their slowness to accommodate on the Si lattice sites. However, there is no comprehensive theory regarding the effect of electrically-inactive dopants on SPER. F is another impurity that decreases the regrowth velocity and it is important from device perspective since it is added along with B in the form of BF_2 for the

formation of highly doped source/drain regions of PMOS transistors³¹. B enhances the regrowth rate and F reduces it. The overall effect is that the regrowth rate does not change much from the intrinsic value²⁷.

Ho *et al.*⁴⁸ studied the effect of B and P enhancement of SPER velocity in (001), (110) and (111) substrate orientations using RBS. The enhancement from P was found to be isotropic, while B was observed to have a higher enhancement on (001) substrate compared to (110) and (111). However, the data on B for (110) substrate had data scattering (upto ~17%) and (111) substrates were plagued by the formation of twin defects that can offset measurement of velocity⁴⁸.

2.1.4 Stress Effect on SPER

Stress effect on SPER has been extensively studied for planar (001) Si substrates^{21,33,34,36-38,41,42,49-51}. The first attempts to study stress during SPER was done by Nygren *et al.*³⁶. The influence of pure hydrostatic stress on SPER kinetics was studied using Rutherford Backscattering Mechanism (RBS). It was found that the regrowth velocity, v , was exponentially enhanced by compressive stress. Thus, v as a function of σ takes the form,

$$v = v(0) \exp\left(\frac{\Delta V_h^* \sigma}{kT}\right) \quad (2-4)$$

where $v(0)$ is the unstressed velocity, $\Delta V_h^* = (-0.28 \pm 0.03)\Omega$ is the activation volume for pure hydrostatic stress and $\Omega = 12.1 \text{ cm}^3/\text{mol}$ is the atomic volume of Si. Negative activation volume suggests the reduction in the net volume associated with the transition state which may be due to the lower density of α -Si as compared to c-Si⁵².

Following the hydrostatic stress effect on SPER, Aziz *et al.*⁴¹ conducted a series of experiments to study the role of in-plane uniaxial stress (σ_{11}) on SPER. It emerged from a

scattered data set that tension was increasing the v while compression was reducing it. In line with Equation (2-4), Aziz⁴¹ advanced v as a function of σ_{11} as,

$$v = v(0) \exp\left(\frac{\Delta V_{11}^* \sigma_{11}}{kT}\right) \quad (2-5)$$

where $\Delta V_{11}^* = (0.15 \pm 0.01)\Omega$. The expression was then generalized to take into account arbitrary stress σ_{ij} as⁴¹,

$$v = v(0) \exp\left(\frac{\Delta V_{ij}^* \sigma_{ij}}{kT}\right) \quad (2-6)$$

where ΔV_{ij}^* is the activation volume tensor such that $\Delta V_{ij}^* = 0$ for $i = j$ due to symmetry constraints. The effect of shear stresses on SPER is thus assumed to be negligible. Also, SPER is assumed to be a single timescale process implying ΔV_{ij}^* is a sum of nucleation and migration processes in SPER.

Furthermore, the activation volume for normal uniaxial stress (ΔV_{33}^*) was calculated based on the hydrostatic and in-plane stress measurements. It was predicted that $\Delta V_{33}^* = -0.58\Omega$ ⁴¹ implying an enhancement in v under normal compression (and more than the hydrostatic compression). However, the experimental values for ΔV_{33}^* were found to be $(-0.15 \pm 0.01)\Omega$ much lower than the predicted value.

Recently Rudawski *et al.*^{21,39} attempted to reproduce the results of in-plane stress effects on SPER by applying high stresses using a novel wafer bending technique (as explained in section 3.1.3). Cross-sectional Transmission Electron Microscope images were used to accurately determine the position of the interface for the purpose of calculating SPER velocity. It was observed that in-plane tension in $\langle 110 \rangle$ directions did not affect the SPER velocity even for stresses upto ~ 1.5 GPa. It was also observed that in-plane compression (in $\langle 110 \rangle$ directions)

reduced the SPER velocity till it reached a factor of half at ~0.5 GPa, at which the rate reduction saturated. Thus, an “S-shaped” curve was observed^{21,39}. This contradicted the prior theory of a single timescale process from Aziz *et al.*⁴¹.

The results were explained by Rudawski *et al.*^{21,22,38,39,50} by the nucleation and migration kinetics model for SPER process. The model matches the experimental data very well and the results of the model are shown in Figure 2-5. SPER is assumed to be a two-step process that includes island nucleation and subsequent ledge migration. Under no-stress conditions, nucleation process is assumed to be rate limiting. Stress is assumed to affect only the migration process. In-plane tension increases the migration velocity thereby not affecting the SPER velocity since nucleation is rate limiting. However, compression is believed to reduce migration velocity³⁹. For a (001) Si substrate the compression reduces migration of ledges in the direction of applied stress and slowing down the SPER process. Its effect saturates once it has reduced the migration velocity of ledges in the direction of applied stress (one out of the two orthogonal $\langle 110 \rangle$ directions) to zero³⁹.

In addition to rate-reduction due to in-plane compression, interface roughness was also observed during regrowth⁵³. This led to the formation of defects on the cusps of roughened interface. For a rough starting interface, the roughness was found to increase due to compression and reduce in tension⁵³. The reasons for it are still not wholly understood.

2.2 Patterned SPER

2.2.1 Substrate Orientation Effect and Mask-Edge Defects

As mentioned in section 2.1.2 the substrate orientation strongly affects the regrowth velocity. A patterned amorphous region is replete of various substrate orientations especially around the corner of the pattern as shown in Figure 2-5. The effect of these orientations manifests itself in the form of a non-isotropic regrowth velocity for the α -c interface. The first

experiments on patterned regrowth were done by Cerva *et al.*^{17,18} with a high-energy As⁺ implant causing amorphization. Figure 2-6(a) shows the as-implanted α -c interface for (001) Si with $\langle 110 \rangle$ in-plane directions¹⁸. Figure 2-6(b) shows the interface after partial regrowth. It can be readily observed that the bottom interface (001) regrew the fastest, followed by the side front (110). The notch at the corner formed by (111) and neighboring fronts is noticeable suggesting a very slow regrowth in that direction¹⁸. These observations match completely with the orientation effect data from Csepregi *et al.*¹³ mentioned in section 2.1.2.

Figure 2-6(c) shows the fully regrown Si along with the presence of a defect created along the notch direction ($\langle 111 \rangle$ direction). The defect is believed to be formed when the edges of the notch approach each other during further annealing, resulting in the generation of corner defects due to the mismatch between the merging interfaces²⁴⁻²⁶. These defects are called mask-edge defects because they normally occur below the edge of the mask. The theory about mask-edge defects formation due to mismatch of merging interfaces is supported by prior experiments⁵⁴ which showed the formation of “clamshell” defects when two interfaces of a buried amorphous layer merge on the completion of SPER.

Some later experiments from Shin *et al.*²⁴⁻²⁶ with a similar structure as Cerva *et al.*¹⁸ suggested the formation of vacancy-related half loop defects in the corners without the formation of a notch. These were attributed to the presence of As⁺ in the samples. Thus, to confirm the effect of orientation on the formation of notch in the corner followed by the mask-edge defect formation, Saenger *et al.*¹⁵ created the patterned amorphous regions by Ge⁺ implantation. Upon regrowth, the pinching of the corners was observed followed by formation of mask-edge defects. Experiment was done on (001) and (011) substrates (Figure 2-7 (a), (b) respectively). For (001) substrates, the defects were angled at $\sim 54^\circ$ from the bottom (001) front while they were $\sim 35^\circ$

from the bottom (011) front for (011) substrates. Thus, the defects on the two substrates were clearly angled in the $\langle 111 \rangle$ directions (Figure 2-7 (c))¹⁵.

Another noticeable factor in all the experiments^{15,18,26,55,56} done for patterned regrowth is that the regrowth interface contacting the SiO₂ layer just under the masking constricts SPER at that point. The reason was attributed to the fact that the bonds between amorphous Si and O are stable and do not allow Si to recrystallize at the contacting interface⁵⁵. Hence, these samples are usually referred to as having the regrowth interface subjected to surface pinning. The effect of surface pinning is that the regrowth interface on the side front bows inwards in the regrowth direction. The possibility of surface pinning affecting the formation of mask-edge defects is not clearly understood.

2.2.2 In-Plane Uniaxial Stress Effect on Patterned SPER

Stress effect on planar SPER has been studied in great detail as shown in section 2.1.4. Stress effect on patterned SPER was first observed by Barvosa-Carter *et al.*³⁴ with (001) Si α -c interface patterned like a sinusoidal wave of small amplitude ~25 nm and ~400 nm wavelength (Figure 2-8(a)). It was observed that in-plane uniaxial compression increased the amplitude of the sinusoidal interface during regrowth while corresponding tension decreased the amplitude (Figures 2-8(b), (c)). The results were explained by the difference in stress experienced by the peaks and the valleys of the interface. It was suggested that for compression, the valleys find themselves under stress concentration while the peaks have stress relaxation³⁴. Thus, if in-plane compression reduces the interface mobility⁴¹, the perturbations would amplify. The reverse is true for in-plane tension.

The results of stress-effect on sinusoidal wave shaped α -c interface suggested that different interface shape would play a big role in how it evolved under stress. This was further confirmed

when Shin *et al.*²⁴⁻²⁶ conducted experiments with SPER for rectilinear α -c interfaces with and without stress from a SiO₂ layer on (001) Si with $\langle 110 \rangle$ in-plane directions. High tensile stressed plasma-enhanced chemical vapor deposited (PE-CVD) SiO₂ layer led to the formation of mask-edge defects while no defects were observed in low stress case. The formation of defects was attributed to the creation of notch in the corners. The presence of high shear stress near the trench corners was believed to create the notch. Following Shin's work, Ross *et al.*¹⁹ studied the Si₃N₄ mask induced stress effect on SPER. Tensile stressed Si₃N₄ created tension in the amorphous trench. This led to reduction in the formation of mask-edge defects compared to no-stress case.

Furthermore, Rudawski *et al.*²² conducted wafer bending experiments with in-plane compressive and tensile stress (~250 MPa) in an effort to control the regrowth velocity of interfaces in two-dimensional α -Si. The results from the experiment are shown in Figure 2-9(a-i). The evolving interface angle between the $\langle 110 \rangle$ and $\langle 100 \rangle$ regrowth fronts was observed to increase with increasing tensile stress. Thus, in-plane tension was found to reduce the formation of pinching corners and thereby reducing the possibility of mask-edge defects. Compression, however led to stronger pinching of the corners and thus more possibility of formation of mask-edge defects²².

2.3 SPER Modeling

2.3.1 2D Analytical Model

The first comprehensive modeling for regrowth was done by Phan *et al.*⁵⁷. Transition state theory (TST) was used to describe the phase transformation at the Si α -c interface. The assumption of the model is that a single, unimolecular, defect mediated mechanism controls the silicon crystal to amorphous transition rate. The growth rate normal to the interface for a (001) Si substrate at any point of the interface can be given by⁵⁷

$$v = v_0(\theta) \exp\left(\frac{\sigma V^* - E^*}{k_B T}\right) \sinh\left(\frac{\Delta G_{ac}}{2k_B T}\right) \quad (2-7)$$

where, $v_0(\theta)$ is the orientation dependent regrowth as shown in Figure 2-2(b) where θ is angle between the normal to the α -c interface and the $\langle 100 \rangle$ direction. The first exponential factor in equation (2-9) represents the thermal dependence of the interface mobility. $E^* = 2.68$ eV is the activation energy known from literature, V^* is the activation strain tensor, σ is the stress at the interface evaluated at the crystal side, T is the temperature, and k_B is the Boltzmann constant. The stress is believed to affect the activation barrier. The assumption is that the stress state on the amorphous side does not influence the growth rate. The “sinh” term is the free energy driving force with ΔG_{ac} being the difference between amorphous and crystalline silicon. The free energy term is composed of three terms,

$$\Delta G_{ac}(T, \kappa, \sigma) = \Delta G_{ac}^0(T) + \Delta G_{\kappa} + \Delta G_{\sigma} \quad (2-8)$$

where $\Delta G_{ac}^0(T)$ is the temperature-dependent free energy per unit volume from amorphous to crystalline silicon. The second term represents ΔG_{κ} represents the change in free energy due to interface curvature. The third term ΔG_{σ} includes the changes in the total energy of the crystal when a volume of materials is crystallized. Under stress, the free energy change will be affected because the system must do work against these forces. The term also includes change in the internal strain energy when a volume of material crystallizes. Further explanation of the free energy terms can be found elsewhere⁵⁷.

Advanced numerical methods were used to solve a system of equations. Level Set Methods⁵⁸ were used to propagate the initial α -c interface with the velocity given by equation (2-7). For the stress simulation, the crystalline side is considered to be elastic and for the amorphous side three cases are used: stress free amorphous, viscous amorphous, elastic amorphous⁵⁷. After

every time-step for regrowth using level set equations, the stress simulation was done using a fairly complicated set of equations from Symmetric-Galerkin boundary integral analysis. The results of the simulations show that the viscous amorphous case fits the best to the data.

However, the large scatter in the data puts some of the predictions in question. The model is able to correctly predict that for an initial sinusoidal wave like α -c interface would grow in amplitude for a uniaxial stress in-plane compression and would dampen in tension case and the no-stress case^{34,51}.

However, as shown in section 2.1.4, Rudawski *et al.*^{21,37,53} have shown the inability of the activation strain tensor to predict the in-plane uniaxial stress effects. In Phan's model⁵⁷ effect of stress on the mobility of atoms in the interface is strongly affected by the term σV^* in equation 2-9. The model predicts exponential increase of the SPER velocity for in-plane uniaxial tensile stress while the experiments have shown no increase in velocity for tensile stresses up to ~1.5 GPa (Figure 2-4)²¹. This has put a question mark on the validity of the model.

Moreover, the curvature effect as a free energy term is suggested to have a negligible effect on SPER⁵⁷. However, the fact that the model was never applied to highly curved interfaces, it is difficult to confirm the negligible effect of curvature effect on SPER. Phan's model is however the first and one of the only attempts to analytically model 2D SPER.

Experiments from Drosd *et al.*⁵⁹ have shown that curvature effect on SPER is significant for radius of curvature smaller than 20 μm . The curvature effect was observed to be more important on (001) Si substrates and in $\langle 011 \rangle$ direction of regrowth because of the formation of $\langle 111 \rangle$ fronts. $\langle 111 \rangle$ fronts require the nucleation and migration of ledges for regrowth. An implication of the results from⁵⁹ would be that concave interface that has some built in ledges

(more than a planar interface) will have a higher SPER velocity than its planar counterpart.

However, this effect has not been captured in the simulations yet.

2.3.2 Atomistic Modeling of SPER

Marques *et al.*^{60,61} did an atomistic study to explain the defect mechanism that controls the recrystallization process. Their results suggested the agglomeration of defects called I-V pairs (interstitial-vacancy pair) as the cause of amorphization. This defect is essentially a bond defect that creates five-member and seven-member rings in Si⁶² instead of the six-member rings (a misnomer since there are no interstitials and vacancies for an amorphous region). Incomplete recombination of a migrating interstitial and vacancy results in the formation of this I-V pair⁶². Marques argued that the presence of these I-V pairs above a threshold concentration results in amorphization. The process of recrystallization is then given by the thermal energy disentangling these I-V pairs. The activation barrier for the dissolution of a single I-V pair is 0.43 eV^{61,63}. However, the presence of neighboring I-V pairs increases this barrier. Thus, the activation barrier of these I-V pairs ranges between 0.43 eV for an isolated I-V pair to 5 eV⁶⁰ for a fully coordinated I-V pair. The dependence of the activation barrier for recrystallization on the coordination number of I-V pairs is given by,

$$E(n) = 0.6 + 0.2n + 0.0012n^3 \text{ (in eV) for } n > 0 \quad (2-9)$$

and $E(0) = 0.43$ eV for $n=0$.

The maximum value of $n=12$ (coordination limit). For a planar α -c interface $n=7$ and the activation barrier is 2.44 eV⁶⁰ that is fairly close to the generally accepted value of 2.7 eV. For patterned amorphous trench regions as discussed in section 2.2.1 the corner of amorphous region is encompassed by crystalline region. This results in a lower coordination number of I-V pair and thus should have a faster regrowth. It also corroborates the curvature effect observed by Drosd *et*

al. ⁵⁹. Marques's ⁶⁰ atomistic model is not appropriate for continuum simulators because of the high simulation time it takes. The time-steps during simulation fluctuate quite a bit resulting in significant simulation time.

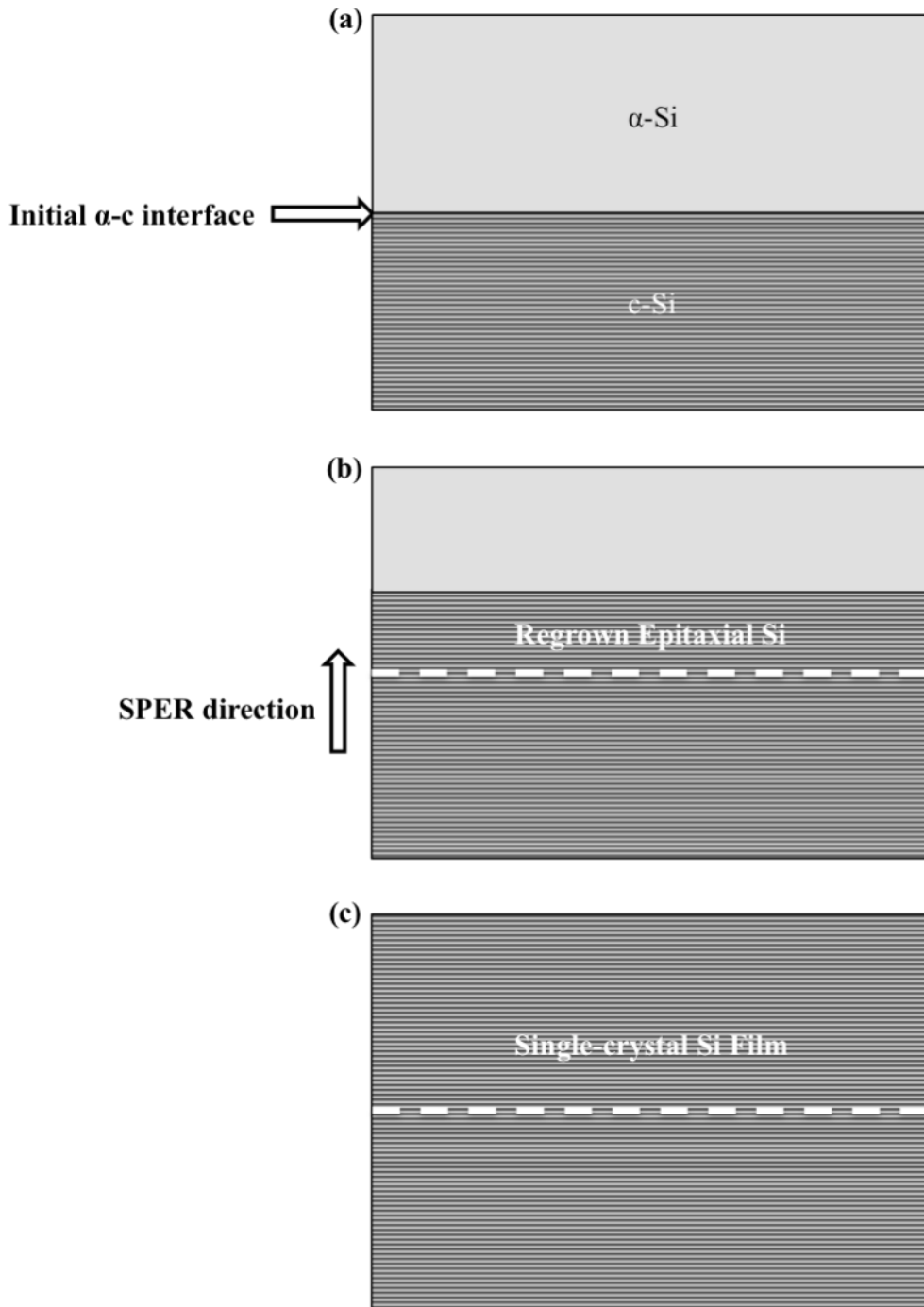


Figure 2-1. Solid Phase Epitaxial Regrowth process. (a) shows the as-implanted α -c interface, (b) shows partial regrowth, (c) shows complete regrowth where the α -Si is converted in to c-Si with the same orientation as the seed.

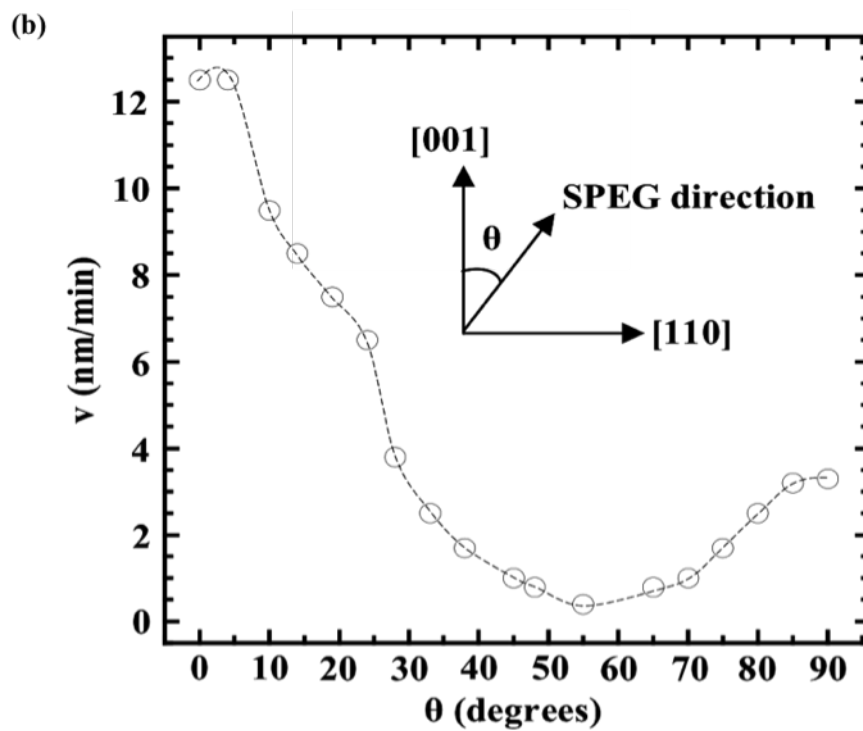
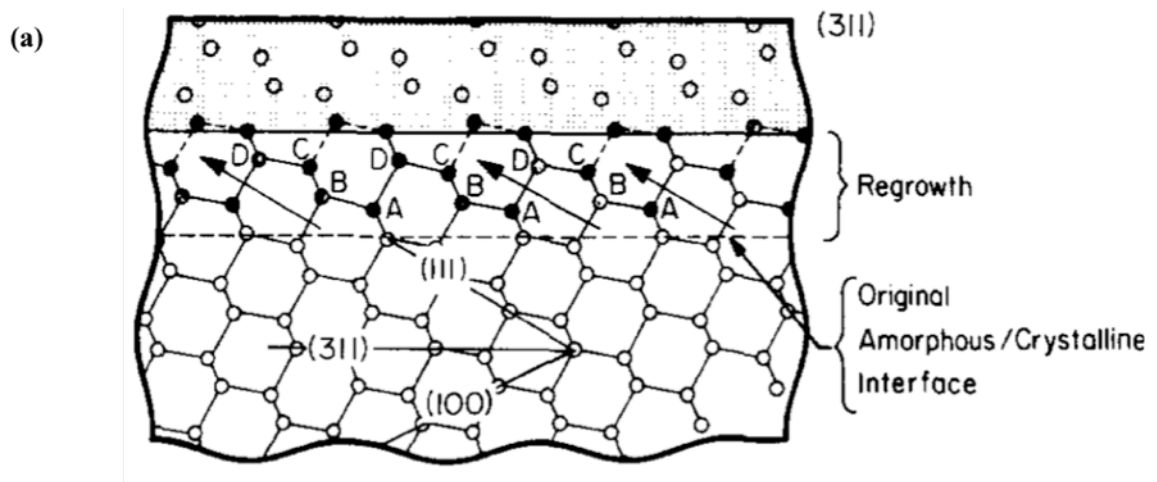


Figure 2-2. Two-dimensional atomistic model for regrowth¹³. (a) Reprinted with permission from Csepregi *et al.*, *Journal of Applied Physics*, 49(7), 3906 (1978). Copyright © 1978, American Institute of Physics. (b) Csepregi's data¹³ on substrate orientation dependence of SPER.

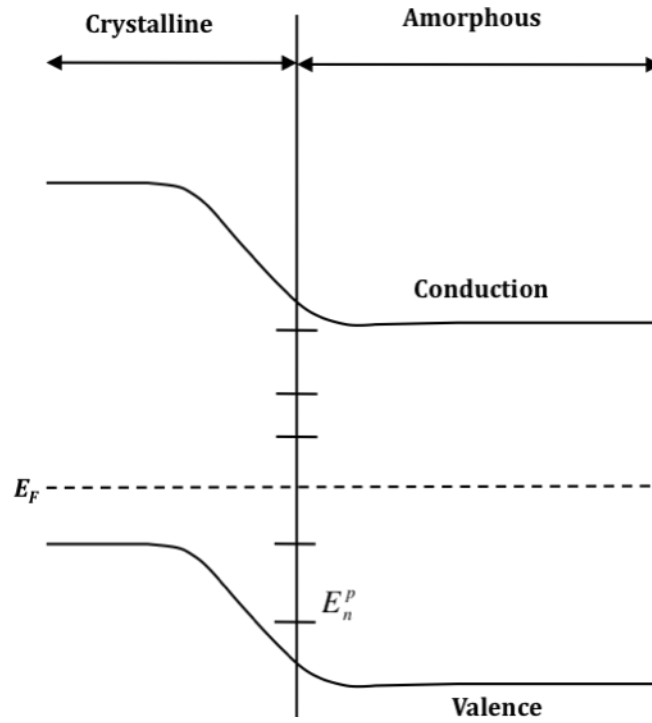


Figure 2-3. Band-diagram of amorphous Si and p-type doped crystalline Si. The Fermi level is pinned at the mid-level for amorphous Si and band bending occurs in the crystalline region²⁹. E_n^p is the energy level of acceptor defect level at the α -c interface.

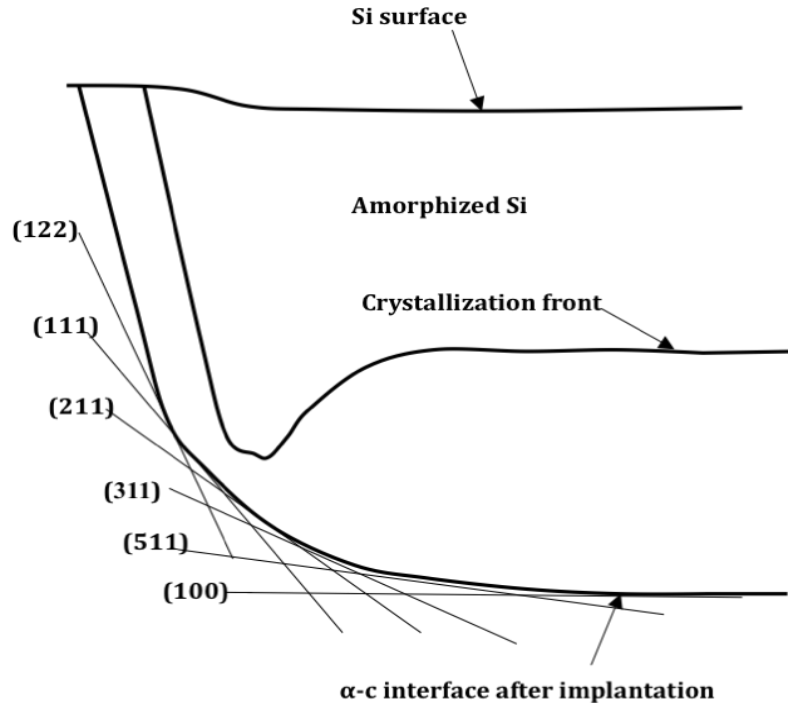


Figure 2-4. Cartoon of a patterned as-implanted amorphous trench region. The interface consists of varying substrate orientations that result in non-isotropic regrowth¹⁸.

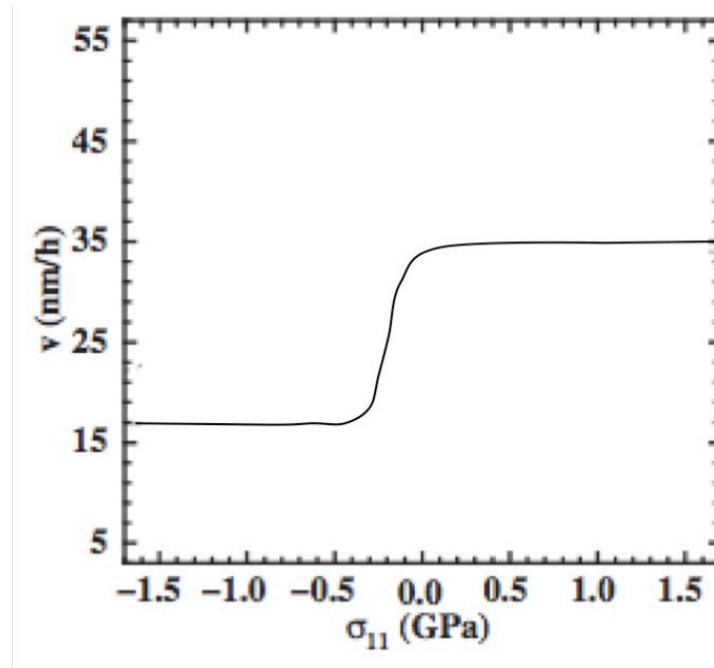


Figure 2-5. Effect of externally applied in-plane uniaxial stress on SPER velocity²¹.

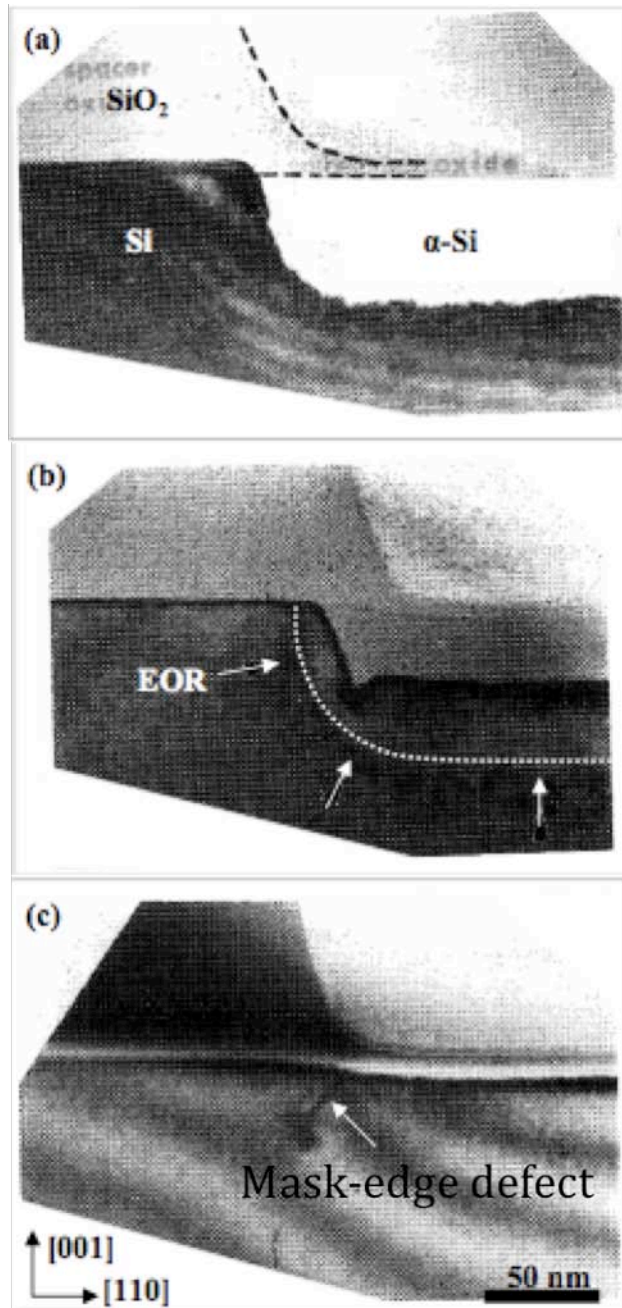


Figure 2-6. TEM images showing patterned amorphous regrowth. (a) as-implanted α -c interface, (b) notch formation at corner due to non-isotropic regrowth, (c) mask-edge defect after SPER¹⁸. Reprinted with permission from Cerva *et al.*, Journal of Applied Physics, 66(10), 4723 (1989). Copyright © 1989, American Institute of Physics.

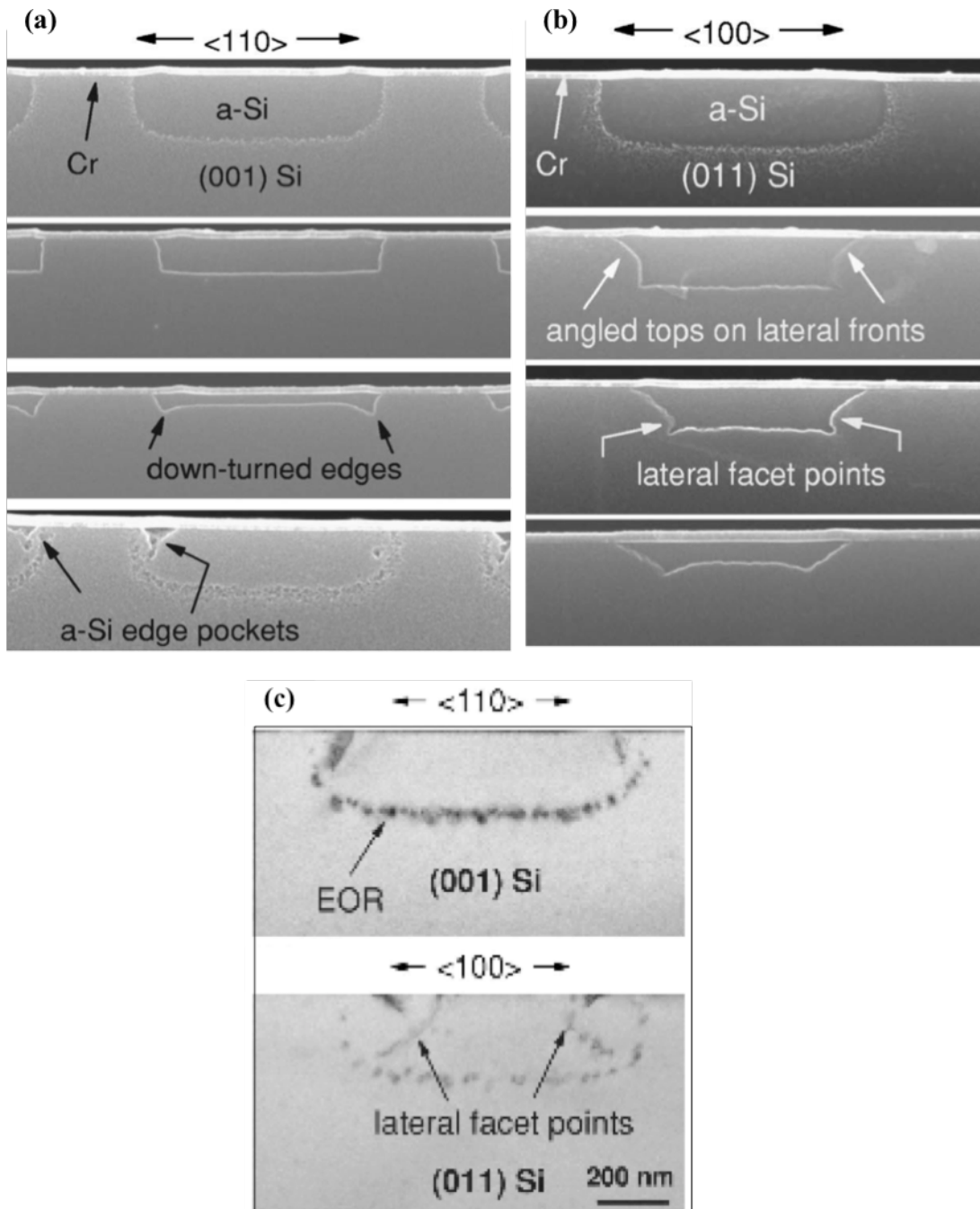


Figure 2-7. TEM images representing patterned SPER for two Si substrates. (a) SPER splits at various times for (001) Si with in-plane $\langle 110 \rangle$ directions, (b) SPER splits corresponding to (a) for (011) Si with in-plane $\langle 100 \rangle$ directions. (c) After completion of SPER, mask-edge defects left behind for the two substrates.¹⁵ Reprinted with permission from Saenger *et al.*, *Journal of Applied Physics*, 101(10), 104908 (2007). Copyright © 2007, American Institute of Physics.

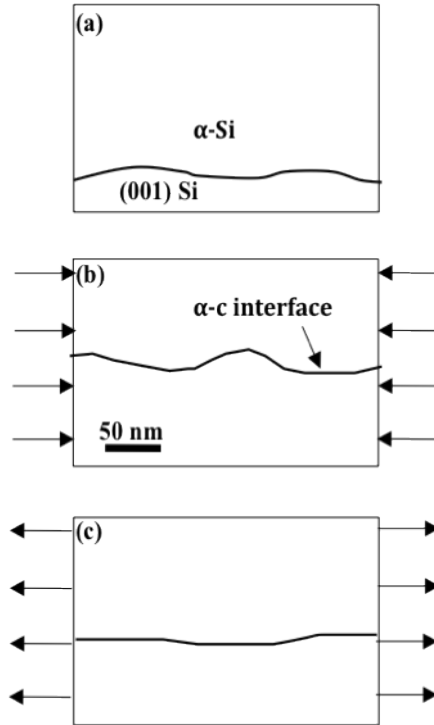


Figure 2-8. Cartoon (based on TEM images ¹⁵) showing SPER of a sinusoidal shaped as-implanted amorphous interface: (a) As-implanted α -c interface, (b) partial SPER under in-plane uniaxial compression shows increase in interface perturbation, (c) partial SPER under in-plane uniaxial tension shows decrease in interface perturbation

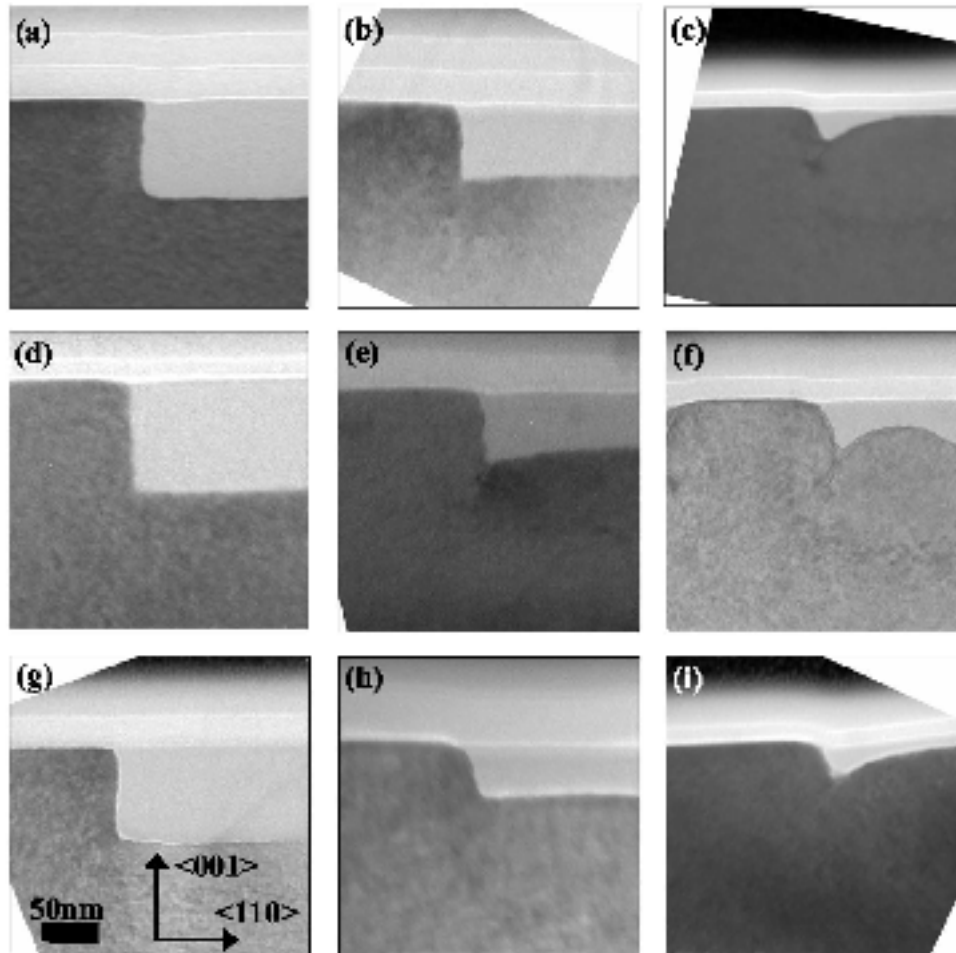


Figure 2-9. TEM images of SPER of patterned trench α -c Si interface under stress, (a), (d), (f) are identical as-implanted α -c Si interfaces; (b), (c) show SPER for increasing times with no external stress applied; (e), (f) show SPER for increasing times under in-plane compressive stress of ~ 250 MPa; (g), (i) show SPER for increasing times under in-plane tension stress of ~ 250 MPa. Stress affects the regrowth shapes and tension case shows no formation of mask-edge defects²². Reprinted with permission from Rudawski *et al.*, Applied Physics Letters, 89(8), 082107 (2006). Copyright © 2006, American Institute of Physics.

CHAPTER 3
EXPERIMENTAL AND SIMULATION TECHNIQUES

3.1 Material Processing

3.1.1 Pattern Creation Using Electron Beam Lithography and Reactive Ion Etching (RIE)

When focused beam of electrons are used to form patterns with high resolution, it is referred to as Electron Beam Lithography (EBL)⁶⁴. As opposed to optical lithography that uses light for creating patterns, the EBL uses focused beam of electrons accelerated to ~10-50 keV potential. The high energy allows electrons to have a shorter wavelength, thus creating patterns with resolution as small as 10 nm. While diffraction is the limiting factor for optical lithography, resist scattering the limiting factor for EBL. The collision of electrons with the material causes them to penetrate the material but lose energy at the same time. These collisions can cause the striking electrons to 'scatter'. The electrons can be backscattered in this process, but more often they proceed forward through small angles with respect to the original path (Figure 3-1)⁶⁵.

As the electron beam interacts with the resist and substrate atoms, it scatters. This scattering has two main effects: 1) the incident electron beam broadens while penetrating, 2) the back-scattered electrons from the substrate add to the ones in the resist and hence the total dose of electrons in resist increases. This results in wider and blurrier images than what would be ideally expected from EBL.

Moreover, if the mask lines are closely spaced, the effect of exposed areas on adjacent lines can add up under the unexposed areas to create a phenomenon known as 'proximity effect.' For the presented study, the spacing of the adjacent lines used were ~0.5 μm and were not strongly affected by proximity effect⁶⁵.

Electron lithography uses positive and negative resists that are sensitive to electron beams. The resist used for the presented work was PMMA A4 (polymethylmethacrylate, anisole 4)

which is a positive resist implying that it softens on interaction with electron beam. A thin layer (~200 nm.) of PMMA was spin-coated on the Si wafer and baked on a hot plate at 175 °C for 15 mins. Subsequently, e-beam lithography was done on the 100×100 μm² squares that were distributed on a 2×2 cm² sample (Figure 3-2). Since, the electron beam lithography is very slow compared to optical lithography, only a small area out of the total sample area was exposed. The electron beam was accelerated at 10 keV from a working distance of 7 mm (above the sample surface) and an aperture of 30 μm. For a PMMA thickness of ~200 nm exposure dose of 75 μC/cm² was used. PMMA was developed using MIBK (methyl isobutyl ketone) 1:3 solvent.

After the patterning of PMMA, the Si was etched using Reactive ion etching (RIE)⁶⁶, an etching technology commonly used in microfabrication. It is a dry etch technology used for creating anisotropic etches. It uses chemically reactive plasma to remove material deposited on wafers. The plasma is generated under low pressure by an electromagnetic field. High-energy ions from plasma attack the wafer surface and react with it (Figure 3-3)⁶⁶. A typical (parallel plate) RIE system consists of a cylindrical vacuum chamber, with a wafer platter situated in the bottom portion of the chamber. The wafer platter is electrically isolated from the rest of the chamber, which is usually grounded. Gas enters through small inlets in the top of the chamber, and exits to the vacuum pump system through the bottom. The types and amount of gas used vary depending upon the etch process; for instance, SF₆ is commonly used for etching silicon. Gas pressure is typically maintained in a range between a few millitorr and a few hundred millitorr by adjusting gas flow rates and/or adjusting an exhaust orifice.

The structures shown in Chapter 7 used Deep Reactive Ion Etching (DRIE)⁶⁷ which is a subclass of RIE and used to etch deep structures (~20 μm for DRAM capacitors) with highly vertical sidewalls. Bosch process is the most commonly used DRIE process that includes SF₆ for

etching (Si) and C_4F_8 for creating a passivation layer to protect the mask. These two processes of etching and deposition alternate to create very high aspect ratio etches. However, for the study in Chapter 7, the etch required was only 150 nm. Thus, a very slow continuous recipe was used with the parameters as: $C_4F_8 = 90$ sccm, $SF_6 = 40$ sccm, RF = 700 W, bias = 32 W, time = 25 sec.

Other types of RIE systems exist, including inductively coupled plasma (ICP) RIE. In this type of system, the plasma is generated with an RF powered magnetic field. Very high plasma densities can be achieved.

A combination of parallel plate and inductively coupled plasma RIE is possible. In this system, the ICP is employed as a high density source of ions which increases the etch rate, whereas a separate RF bias is applied to the substrate (silicon wafer) to create directional electric fields near the substrate to achieve more anisotropic etch profiles. For etching $Si_3N_4 \sim 150$ nm (for structure shown in Chapter 6, Figure 6-1), ICP/RIE etch was used with the parameters as: $CHF_3 = 40$ sccm, Pressure = 10 torr, $ICP_1=50$ W, $ICP_2=300$ W, time = 1 min 40sec. Figure 3-4 shows the complete process of e-beam lithography, RIE etch and resist stripping to get the required structure.

3.1.2 Ion-Implantation

Ion-implantation process is the preferred method of introducing dopants into Si wafers during device processing. It offers several advantages that include dopant profile control, high repeatability and the ability to introduce dopants into highly localized portions of a Si wafer (e.g. halo implants for MOS devices). In ion-implantation, atoms with mass, m , to be implanted are first ionized from a gas source using an ionizing coil to acquire a net electric charge, q , and accelerated through a potential difference, V . Then, an analyzing magnet is used to isolate the desired ions for implantation from any possible impurities and the ions are then directed towards

the Si target (Figure 3-5). The relationship between m , q , V , and the velocity of the incoming ions, v_{ion} , is given by

$$\frac{1}{2}mv_{ion}^2 = qV, \quad (3-1)$$

where $qV = E_0$ is defined as the kinetic energy acquired by the ion. As ions travel through the crystal, their collisions with the lattice can be nuclear or electronic. Nuclear collisions make the implanted ions lose their kinetic energy and they finally come to rest⁶⁸. The implantation process is known to be statistical in nature (and thus simulated by probability events using Monte Carlo simulations) and the collisions suffered by each ion would be different. For a given ion, the distance, R , the ion will travel into the substrate is given by

$$R = \int_{E_0}^0 \frac{1}{dE/dx} dE \quad (3-2)$$

where the quantity dE/dx is defined as the incremental energy loss with respect to distance traveled by the implanted ion. For the case of one-dimensional ion-implantation, R_p is defined as the mean variance of R and is referred to as the ion projected range. The standard deviation of R gives the straggle, ΔR_p . Typically, the concentration of implanted ions, $N(x)$ as a function of the distance into the substrate, x , can be approximated as Gaussian function given by

$$N(x) = \frac{Q}{\Delta R_p \sqrt{2\pi}} \exp\left(-\frac{(x - R_p)^2}{2\Delta R_p^2}\right) \quad (3-3)$$

where Q is the implant dose. This is valid for an ideal case of uniform and amorphous target, with the collision frequency and energy transfer per collision being random. For crystalline target, the distribution is somewhat different. Certain directions in the crystal structure allow for channeling of ions i.e. fewer collisions and there is deeper penetration of incoming ions⁶⁹.

The nuclear collisions between the incoming ions and the Si lattice leads to displacement of Si atoms from their lattice. These displaced atoms acquire enough energy to displace more lattice atoms and this leads to, what is known as a damage cascade⁷⁰. A large number of vacancies and interstitials are created (known as point defects) as the lattice atoms are displaced. If the dose of ions is sufficiently high, the damage can displace a percentage of the lattice atoms (over 10%⁷¹, creating amorphous region (α -Si). This process is highly sensitive to the type of ions being implanted. Large, heavier ions such as Xe⁺, Ge⁺, or Si⁺ cause amorphization at lower doses ($< 1 \times 10^{15} \text{ cm}^{-2}$) while lighter ions such as B⁺ amorphize at higher doses ($> 1 \times 10^{16} \text{ cm}^{-2}$) since heavier ions tend to form denser damage cascades⁷².

In the presented work, the generation of continuous α -Si films on Si substrates was effected via Si⁺-implantation at vacuum of $\sim 8 \times 10^{-8}$ torr into single-crystal (001) Si substrates. All implants in this study were done on patterned Si₃N₄ or patterned Si. A sequence of Si⁺ implants with energies of 20, 60 and 160 keV to doses of 1×10^{15} , 1×10^{15} , $3 \times 10^{15} \text{ cm}^{-2}$, respectively, generated an undulating α -Si layer ~ 270 nm thick. A band of defective Si just beyond the initial α /crystal interface, known as the end-of-range (EOR) damage, was observed for all samples (Figure 3-6). Upon annealing, this region evolves into extended defects (dislocation loops and rod-like 311 defects) which have been thoroughly studied in the literature⁵⁴. However, the temperatures used in this work were low ($500\text{-}575^\circ \text{C}$) and no evolution of EOR or their interaction with the regrowth process was observed.

3.1.3 Application of In-Plane Uniaxial Stress

As shown in Chapter 2, stress plays a major role in SPER process. It affects the planar regrowth growth velocity and in addition it affects the regrowth shape of the corners in patterned amorphous regions. To delineate the effects of various components of stress on regrowth,

uniaxial stress was applied in the plane of the regrowth interface (only $\sigma_{11} \neq 0$). It is well known that stress is a product of Young's modulus (E) and strain (ϵ) under the elastic limit (Hooke's law).

$$\sigma_{11} = E_{11} \cdot \epsilon_1 \quad (3-4)$$

where E_{11} for this study is in the $\langle 011 \rangle$ crystal orientations (since they are the in-plane directions for (001) Si substrate).

The method for applying the uniaxial in-plane stress involves the use of a quartz self-supported bending apparatus (Figure 3-7). This was first implemented by Rudawski *et al.*^{21,37,38}. The experiments in this study using that apparatus have been completely based on his study. For more information on the apparatus, refer to Rudawski's thesis⁵³.

The amorphous interface in for prior experiments using the bending apparatus were planar⁵³. Presented study, however involves stress on patterned amorphous regions. For applying uniaxial in-plane stress, the patterned lines were placed perpendicular to the stress direction in most cases as shown in Chapter 7. In some cases the lines were parallel to the stress direction (see Chapter 7). It must be noted that in both cases the stress application was in the $\langle 011 \rangle$ directions that were the in-plane directions.

3.1.4 Temperature Calibration and Annealing

SPER process is a thermally activated process and the temperature needs to be accurately measured. Even a variation of temperature from 525 to 530 °C results in a regrowth velocity increase of ~28%²⁷. To ensure temperature correctness, the quartz tray (shown in Figure 3-8) was inserted in the tube furnace and the temperature on the tray was measured using a thermocouple after temperature stabilization. The tray with the samples was inserted at the same spot. The tensile, compressive and non-stressed samples were annealed simultaneously and kept

close to each other to avoid any temperature variation amongst them. The error in all T measurements was estimated to be ± 2 °C as per the accuracy of the thermocouple device. N_2 gas was flowed at ~ 1 l/min through the tube furnace for all annealing to prevent thermal oxidation. For the present study, $T = 500 - 575$ °C was used with anneal times of 2-10 h.

As mentioned in Chapter 2, it is possible for the applied stress to relax depending on the annealing temperature, time and applied stress. The experiments done in this study assume that there is no stress relaxation in the samples. To confirm that no stress relaxation happened during annealing, the radius of curvature was measured for the annealed strips. No measureable difference was seen in the radius when compared to before annealing case. Thus, it can be safely assumed that the strips retained the applied stress during annealing.

3.1.5 Cross-section Transmission Electron Microscopy Sample Preparation

A focused ion beam (FIB) system was used to prepare site-specific transmission electron microscopy samples from the strips. The patterns created by e-beam lithography were located at a specific distance from the strip end and had 100 μm side lengths. In this method, a focused beam of Ga^+ ions from the FIB system is accelerated to 30 keV and used to mill away small portions of the wafer^{73,74}. A 100 - 200 nm-thick 10 μm -long, electron-transparent specimen is produced which is lifted out externally and placed on a grid for imaging. Since, the Ga^+ ions charge the surface of the sample, a thin C film ~ 30 nm was evaporation-coated on the sample before FIB processing. Subsequently, a layer of Pt ~ 1 μm thick was FIB-deposited over the area of interest to protect the sample from beam damage during sample preparation.

3.2 Material Characterization

3.2.1 Transmission Electron Microscopy

Transmission electron microscopy (TEM) is widely used for microstructural characterization. In TEM, a beam of electrons is accelerated using a thermionic emission source

across a potential difference of ~200 keV and directed at the specimen. Electrons at such high energies show wave-like behavior and according to de Broglie's hypothesis an accelerating voltage ~200 keV creates a wavelength $\lambda \sim 2.5 \times 10^{-12}$ m. Small λ allows for resolution of nanometer-scale features in TEM samples.

In the case of α -Si, since no distinct crystalline planes exist, the scattering of the incident beam would be different as compared to c-Si. This gives rise to contrast between the two phases during imaging. It is possible to increase this contrast between α -Si and c-Si phases by selectively allowing certain electrons to contribute to the generated image (using selected area diffraction). More analysis of the TEM instrument and imaging conditions can be found in⁵³.

For all work presented in this study, $B = [1\bar{1}0]$ (orthogonal to the wafer orientation) was used for TEM imaging. This TEM imaging style is known as cross-sectional TEM (XTEM), since the wafer structure is being observed from the side. A sample XTEM image from the study is shown in Figure 3-6.

3.3 Simulation Techniques

3.3.1 Level Set Methods

Level Set Methods are computational techniques that were proposed by Sethian and Osher to track the evolution of a moving interface in 2D/3D⁵⁸. These methods work on embedding the solution of the equation, i.e. the position of the interface, in a higher order function. This higher order function is solved using a partial differential equation (convection equation) given, the initial position of the interface and the velocity of interface propagation (normal to the interface). The reason this technique became popular was the failure of traditional interface tracking techniques like the marker/string methods in cases of sharp corners.

The marker/string methods use the standard Lagrangian form of the equations of motion. In this approach, the parameterization is discretized into a set of marker particles whose positions

at any time are used to reconstruct the front. The problem with the marker method is that it has a positive feedback on error. The way the error grows is quoted by Sethian⁵⁸ as:

(1) A small error in approximate marker positions produces, (2) local variations in the computed derivatives leading to (3) variation in computed particle velocities causing (4) uneven advancement of the markers, which yields (5) larger errors in approximate marker positions.

Hence, within a few time steps the small oscillations grow and solution becomes unbounded. The other problem with marker methods comes in computing derivatives of curves that have singularities. The derivative of singularities leads to the growth of oscillations and cannot be controlled.

Level Set Methods on the other hand do not compute the interface position. They compute a higher-dimensional function that embeds the interface position in it. For our case, the function is the signed distance. The initialization is done by allotting all the points on the level set grid as the signed distances to the original interface as shown in Equation (3-5) (Figure 3-9).

$$\phi(x, y, z, t = 0) = \pm d \quad (3-5)$$

where ϕ is the higher-dimensional function.

Equation (3-5) implies that the value of ϕ is zero at the interface. Rest of the grid points get a value of ϕ equal to their distance from the interface (positive on one side and negative on the other side of interface).

The function ϕ then evolves using a convection Equation (3-6) that contains a velocity that controls the interface propagation.

$$\phi_t + F |\nabla \phi| = 0 \quad (3-6)$$

where F is the velocity of interface, ϕ_t is the time derivative of ϕ and $\nabla \phi$ is the spatial derivative of ϕ . The derivation of the above equation can be found elsewhere¹⁸. Since, the

above equation needs to be discretized for solving on the level set grid, it is necessary to know if the operators (spatial and temporal) need to be backward, forward or centered. The time-derivative is definitely a forward difference operator as we are trying to find the value of ϕ at the next time instant.

For the spatial derivative, the operator needs to have the “upwinding” scheme for getting the correct results⁵⁸. For $F>0$, the backward operator needs to be used and for $F<0$, the forward operator needs to be used. This scheme is called upwinding because it uses values upwind of the direction of information. This is done so that the numerical solution matches up with the analytical solution. More analysis on the use of upwinding scheme can be found in¹⁸. The final update of ϕ is given by

$$\phi_i^{n+1} = \phi_i^n - \Delta t [\max(F_i, 0) \nabla^+ + \min(F_i, 0) \nabla^-] \quad (3-7)$$

where $\nabla^+ = [\max(D_i^{-x}, 0)^2 + \min(D_i^{+x}, 0)^2]^{1/2}$ and $\nabla^- = [\max(D_i^{+x}, 0)^2 + \min(D_i^{-x}, 0)^2]^{1/2}$

Here $D_i^{+x} = D_i^{+x} \phi_i^n$.

Figure 3-10 gives an example as to how ϕ is one dimension more than its solution. Figure 3-11 shows the propagation of the interface with time given the velocity of the interface is constant and positive. It can be seen how the interface is embedded in the function ϕ .

Level Set Methods have been extensively used in simulating etching, deposition, surface diffusion etc. They have several key advantages that include:

- 1) Sharp corners are handled effectively and do not create instability,
- 2) Ability to merge two disjoint surfaces as shown in Figure 3-12⁵⁸, analogous to two oil drops merging to become one bigger drop,
- 3) Accuracy and ease in computation of normals and curvatures at the interface using the function ϕ .

1) and 3) are very important for SPER of patterned region because formation of the pinching corner is the key feature of regrowth as shown in Chapter 2. 2) is helpful for the regrowth of buried amorphous layers in which two regrowing fronts move towards each other and finally merge. It is also important for lateral solid phase epitaxy in which the two disjoint regrowing fronts from the sides eventually merge to complete regrowth. The computation of normal and curvature, is given as follows:

$$\text{Normal } n_{ij}^* \equiv \frac{\phi_x, \phi_y}{(\phi_x^2 + \phi_y^2)^{1/2}} \quad (3-8)$$

where ϕ_x is the spatial derivative of ϕ with respect to x, ϕ_y is the spatial derivative of ϕ with respect to y. First, the one-sided difference approximations to the unit normal in each possible direction are formed. All four limiting normals are then averaged to give the approximate normal at the corner. Normalizing n_{ij}^* , gives the normal n_{ij} .

$$\text{Curvature } \kappa = \nabla \cdot \frac{\nabla \phi}{|\nabla \phi|} = \frac{\phi_{xx}\phi_y^2 - 2\phi_x\phi_y\phi_{xy} + \phi_{yy}\phi_x^2}{(\phi_x^2 + \phi_y^2)^{3/2}} \quad (3-9)$$

Similar expressions for normal and curvature can be made for three dimensions as well ⁵⁸.

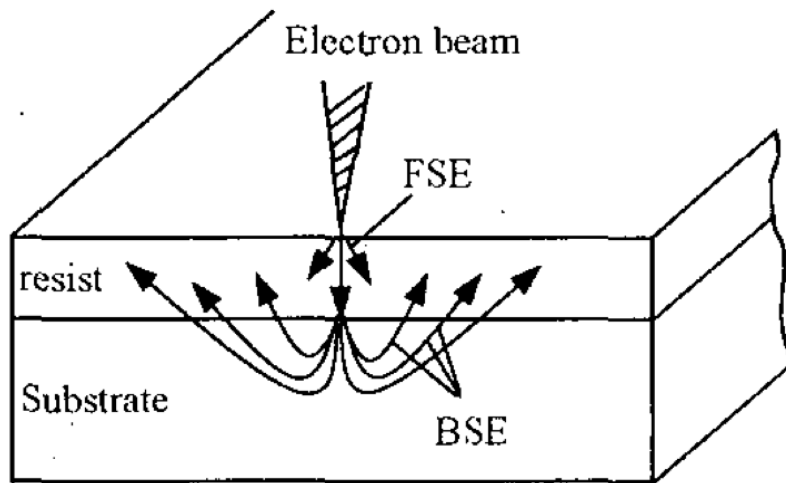


Figure 3-1. Scattering effects during e-beam lithography. Figure shows the forward scattered electrons (FSE) and the back scattered electrons (BSE) ⁶⁵.

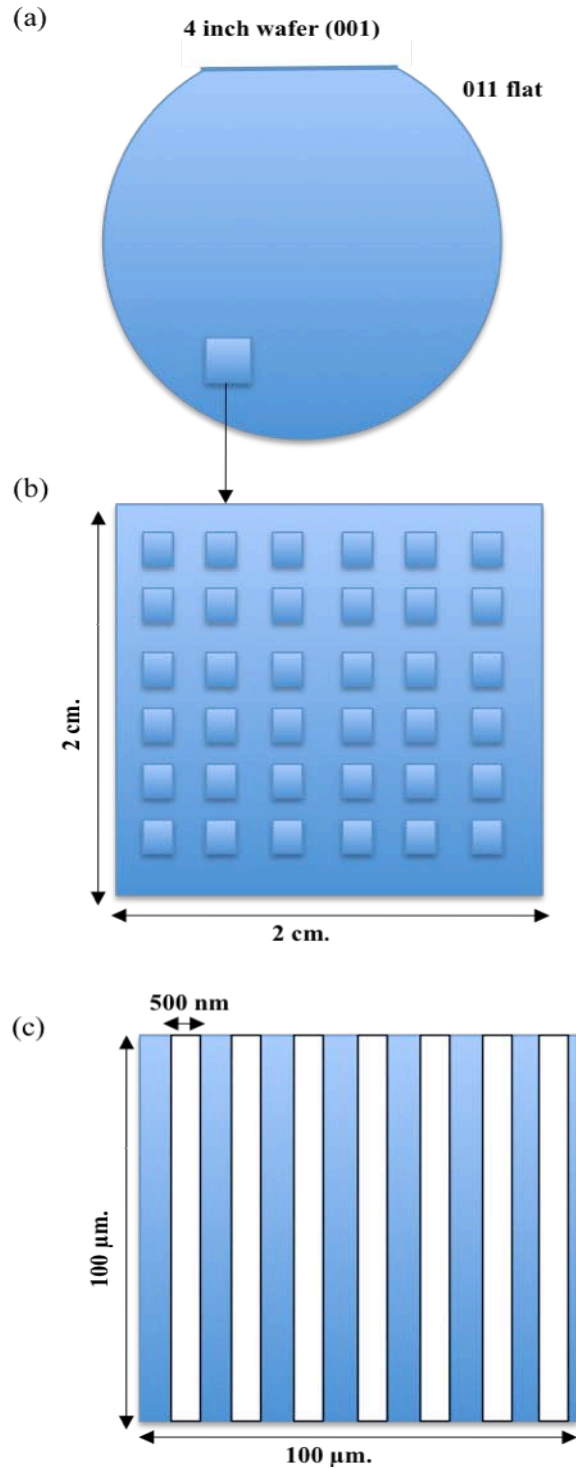


Figure 3-2. E-beam lithography for patterned regions : (a) shows the patterned square on the (001) Si wafer with $\langle 110 \rangle$ in-plane orientations. (b) shows the $2 \times 2 \text{ cm}^2$ piece that contained patterned squares. (c) shows the $100 \times 100 \text{ μm}^2$ squares that had the pattern of lines created by e-beam lithography.

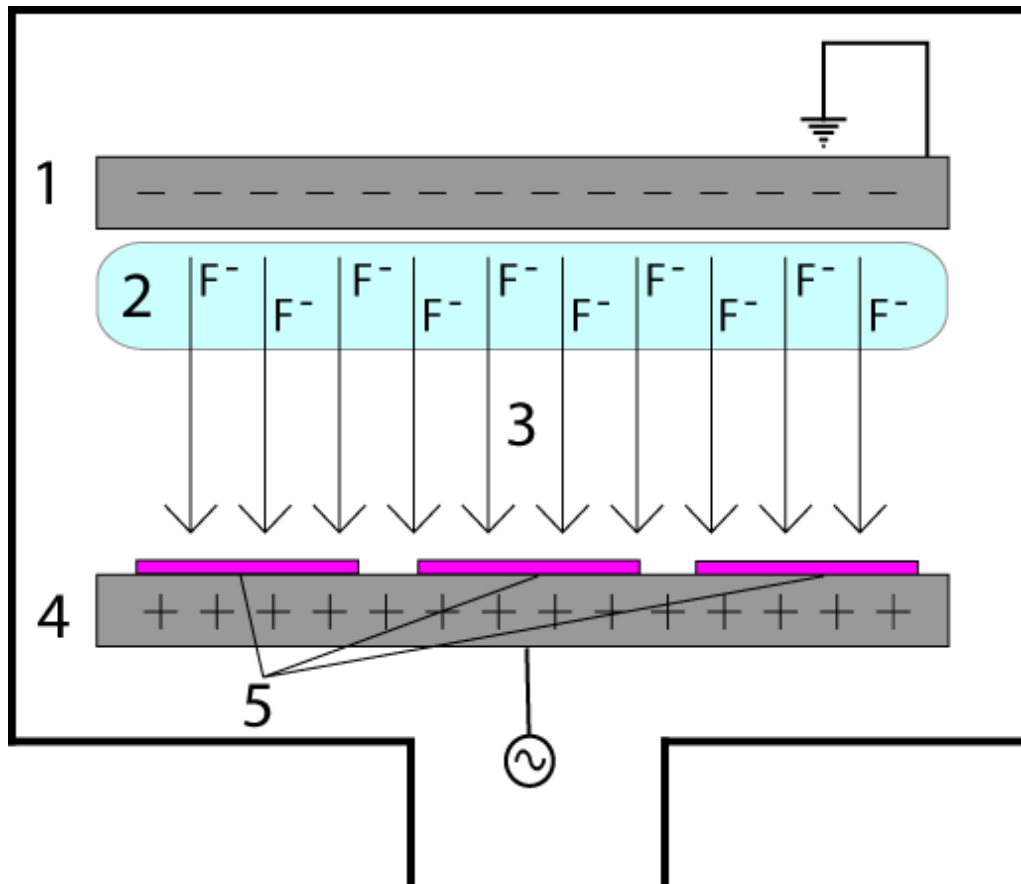


Figure 3-3. A diagram of a common Reactive Ion Etch (RIE) setup. An RIE consists of two electrodes (1 and 4) that create an electric field (3) meant to accelerate ions (2) toward the surface of the samples (5).⁶⁶

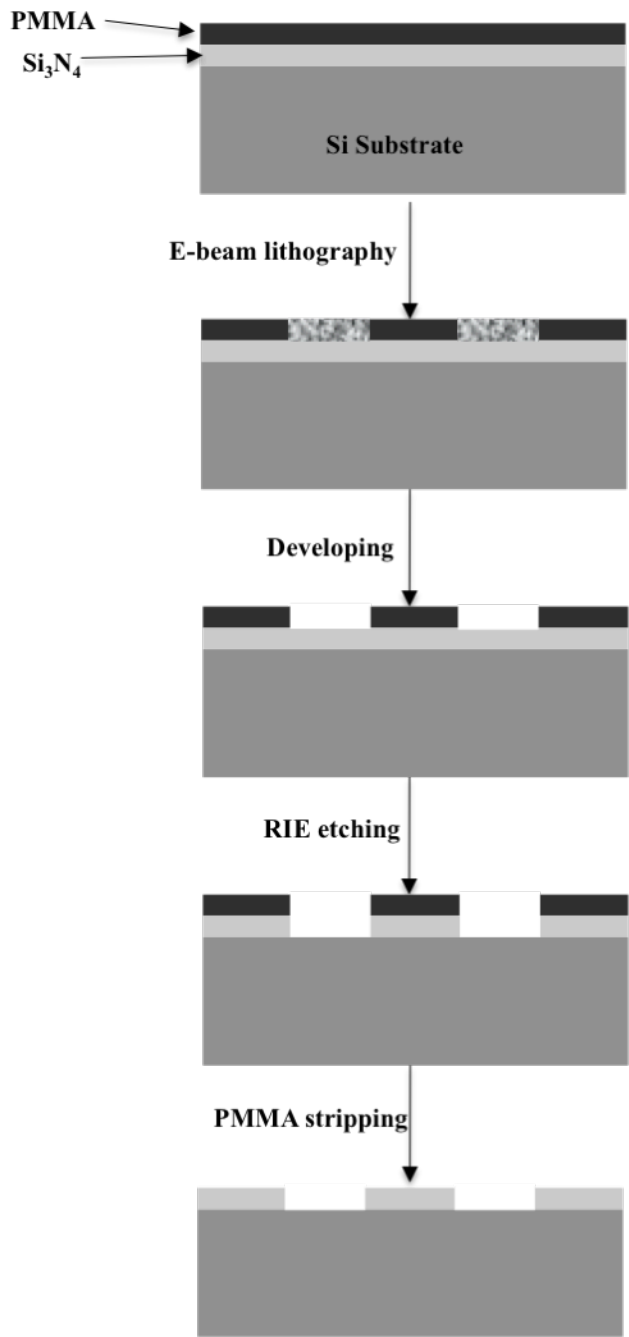


Figure 3-4. Complete process of pattern formation using E-beam lithography and RIE etching.

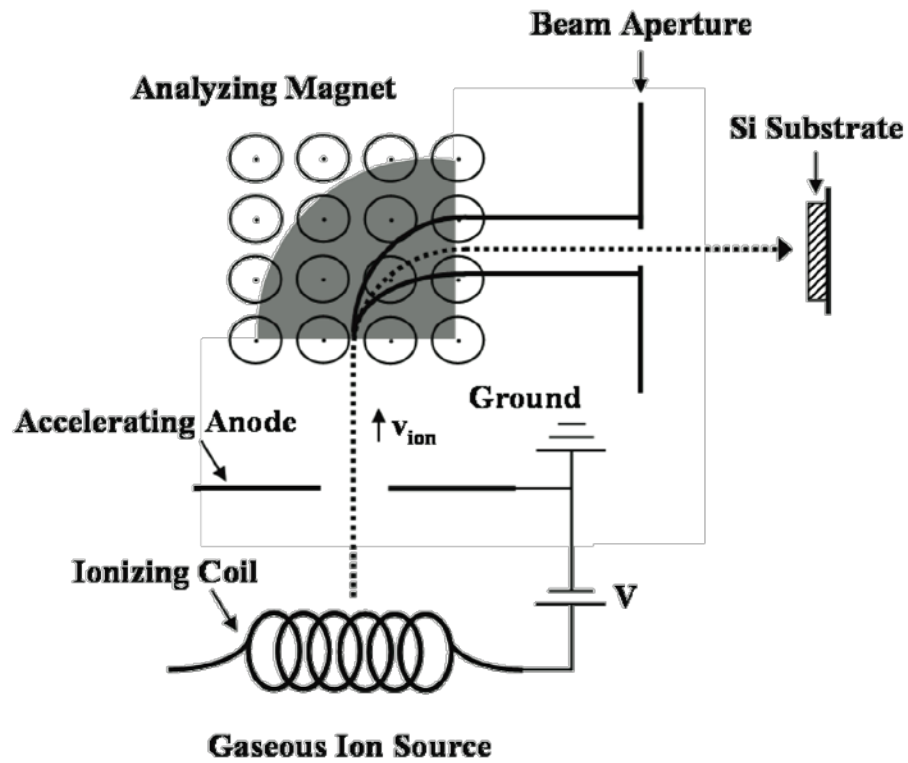


Figure 3-5. Schematic of a basic ion-implantation system.⁵³

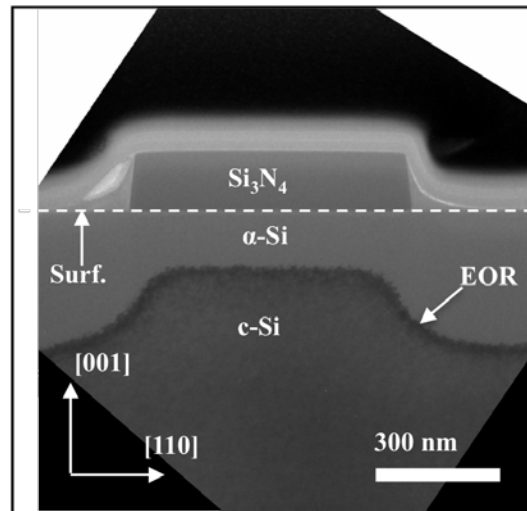


Figure 3-6. Cross-sectional Transmission Electron Microscopy image of an as-implanted Si sample. The Bright field image also shows the end of range (EOR) defects, a band of defective Si just beyond the initial α /crystal interface⁵⁶.

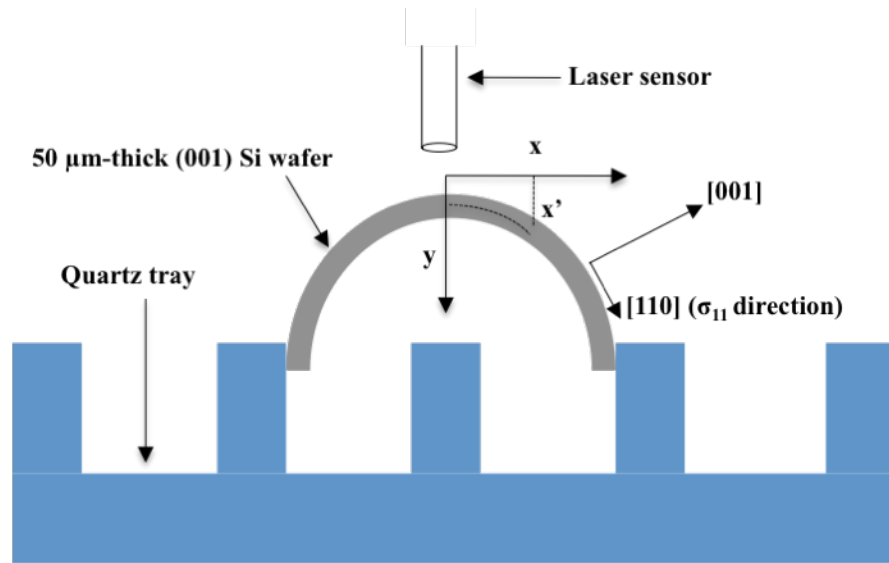


Figure 3-7. Schematic of the apparatus used to induce and measure in-plane uniaxial stress in Si wafers^{37,53}. Reprinted with permission from Rudawski, PhD. Thesis, University of Florida. Copyright © 2008, Nicholas G. Rudawski.

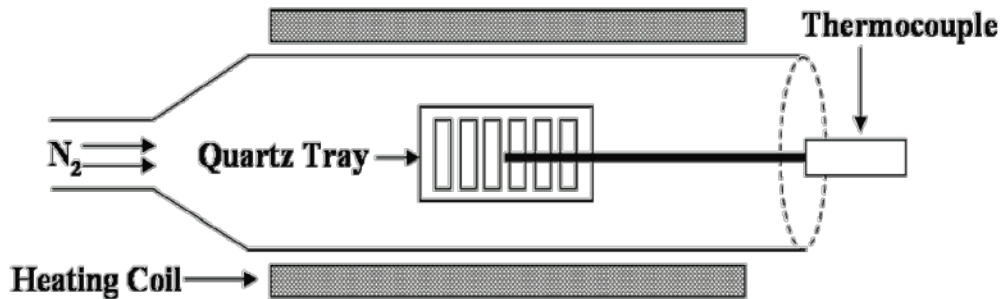


Figure 3-8. Schematic of the tube furnace apparatus used for annealing and the method of temperature calibration⁵³. Reprinted with permission from Rudawski, PhD. Thesis, University of Florida. Copyright © 2008, Nicholas G. Rudawski.

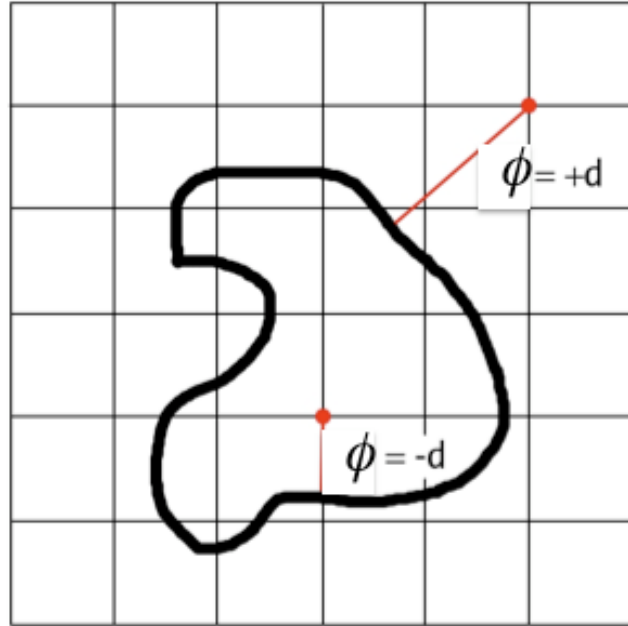


Figure 3-9. Figure shows the initialization of the Level Set higher order function ϕ as a signed distance to the interface⁵⁸.

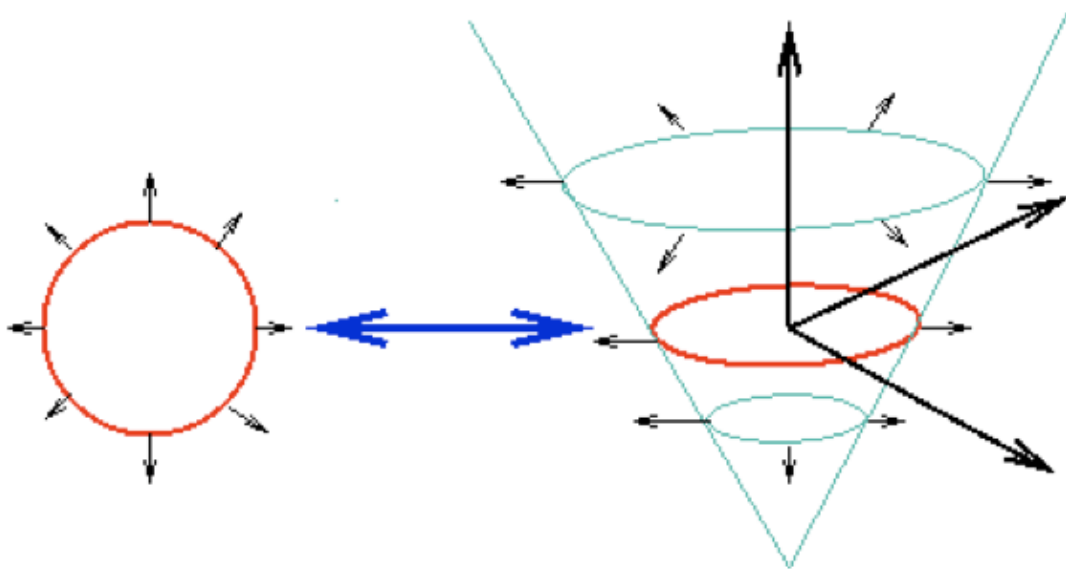


Figure 3-10. Pictorial view of level set function $\phi(x, y, t)$ on the right. Left figure shows the interface at x, y at time $t=t_1$ where $\phi(x, y, t_1) = 0$. The position of the interface is embedded in the function ϕ ⁵⁸.

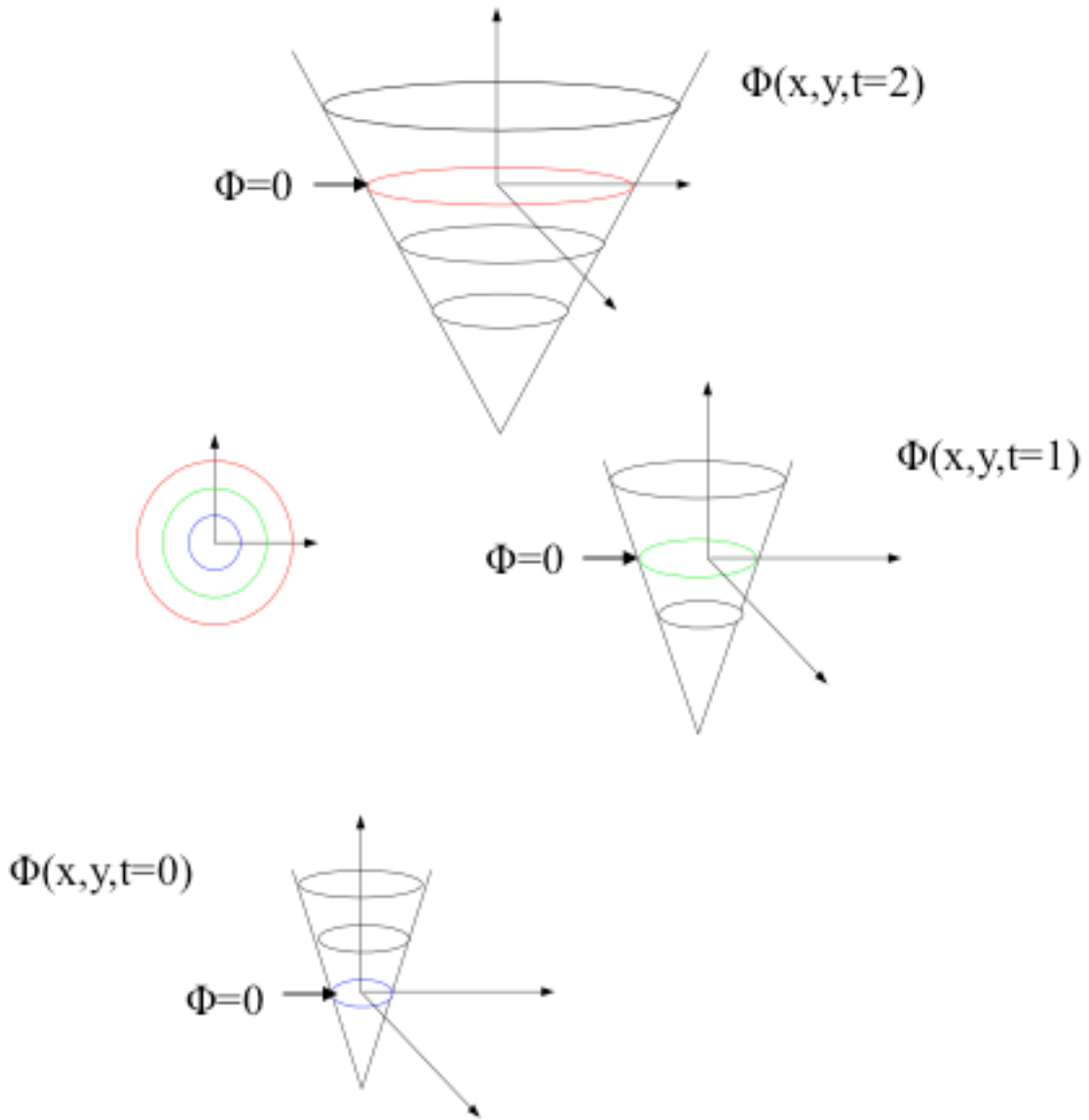


Figure 3-11. Time evolution of the level set function and extracted interface at different times. The interface is circular and expanding with a fixed isotropic velocity⁵⁸.

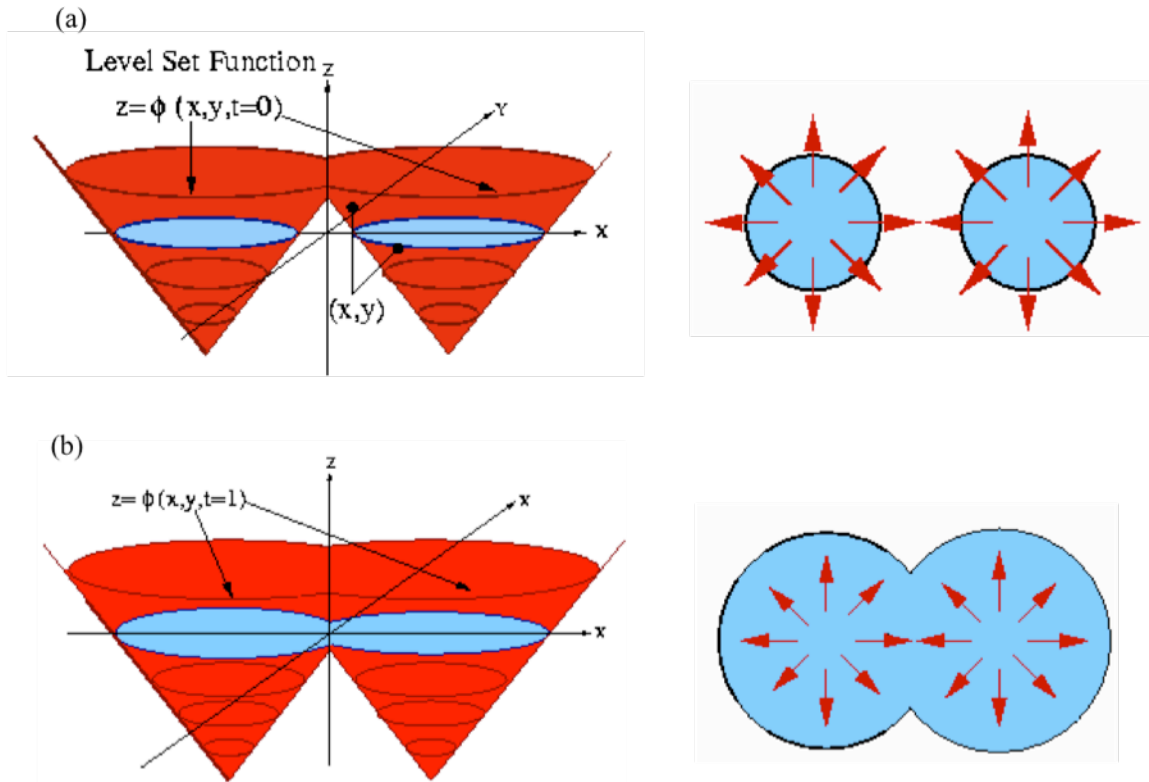


Figure 3-12. Ability of Level Set method to merge two disjoint regions :(a) level sets at $t=0$. (b) level sets at $t=1$ ⁵⁸.

CHAPTER 4 IMPLEMENTATION OF LEVEL SET METHODS FOR SOLID PHASE EPITAXIAL REGROWTH AND INITIAL RESULTS

4.1 Introduction

As mentioned in the Literature review section, the Level Set Methods provide a very stable numerical technique for the implementation of interface evolution. For their implementation, the interface velocity is required. For solid phase epitaxial regrowth (SPER) the velocity could be dependent on an isotropic velocity function (normal to the interface)²⁷ and curvature of interface^{14,56}. SPER is also known to be dependent on a lot of other factors that include temperature²⁷, orientation of the amorphous-crystalline (α -c) interface¹³, stress (or pressure)^{19,34,53,57}, dopant concentration^{28,29,47} etc. This chapter focuses on implementing Level Set Methods for regrowth of patterned amorphous intrinsic Silicon (Si). It also includes the results of experiments done on regrowing patterned amorphous intrinsic Si regions. The initial simulation results from Level Set Methods are matched to the experimental results. The chapter provides a starting point for the work shown in future chapters.

4.2 Level Set Implementation

Implementation of Level Set model for regrowth involved setting up the grid first. Rectangular grid was found to be the best one for Level Set discretization. Level sets are computed by solving an advection equation as given by (same as Equation 3-6),

$$\phi_t + F |\nabla \phi| = 0 \tag{4-1}$$

where F is the velocity normal to the interface and ϕ is the level set function that is being solved for. As mentioned in chapter 3, ϕ represents the higher order function that contains the interface location (x, y, z) using Equation 3-5. ϕ in our case was defined as the signed distance from the α -

c interface. Planar regrowth velocity for intrinsic Si has been known to have a thermal activation barrier of ~ 2.7 eV²⁷ and is given by

$$v_{[001]} = v_0 \exp(-E_a/kT) \quad (4-2)$$

where $v_{[001]}$ is the value of v along [001] direction, v_0 is the prefactor from [], $v_0 = 3.1 \times 10^8$ cm s⁻¹.

However, a patterned amorphous region contains fronts that have varying orientations to the wafer normal (001 for our case) as shown in Figure 4-1. Csepregi's data¹³ showed that for Si, orientations affect the regrowth velocity of α -c interface. Figure 4-2 shows the simulation of regrowth of patterned amorphous region with an isotropic planar velocity and no orientation dependence. The outermost contour represents the initial α -c interface. The other contours represent the position of interface at different times of regrowth (the innermost contour being the longest time). It is clear from the TEM images of regrowth from prior experiments (shown in Figures 2-6 and 2-7) that these regrowth simulations do not match up in shape with them. Hence, it was important to add the orientation dependence on the regrowth velocity.

The normalized regrowth velocity, $f(\theta)$, as a function of the substrate orientation angle from [001] towards [110] (θ) was measured by Csepregi *et al.*¹³ as shown in Fig. 4-3 with the fastest regrowth velocity along [001] (corresponding to $f(\theta) = 1.0$). Thus, v as a function of θ , is given by

$$v(\theta) = v_{[001]} f(\theta) \quad (4-3)$$

where $v_{[001]}$ is the value of v along [001] and $f(\theta)$ is temperature-independent and accurately fit using a least-squares fifth-order polynomial¹⁴. The [001] regrowth velocity is ~ 25 times faster than the slowest regrowth direction of [111] and almost ~ 3 times faster than the [110] direction.

This orientation dependence was also observed in studies using patterned amorphized wafers^{15,18,22}.

The polynomial for orientation dependence factor is given by:

$$f(\theta) = A_1 \times \theta^5 + A_2 \times \theta^4 + A_3 \times \theta^3 + A_4 \times \theta^2 + A_5 \times \theta + A_6 \quad (4-4)$$

where $A_1 = 5.3e-10$, $A_2 = -2.0e-7$, $A_3 = 2.4e-5$, $A_4 = -8.9e-4$, $A_5 = -1.4e-2$, $A_6 = 1.02$ and θ is the angle in degrees¹⁴. $f(\theta)$ is valid for θ sweeping from 0 to 90° which was sufficient for covering the entire as-implanted α -c interface in our case (for (001) wafer and <110> in plane directions). Since $f(\theta)$ is unitless, the units of A_1 - A_6 are accordingly (e.g. A_5 has unit degrees⁻¹). $f(\theta)$ being temperature-independent implies that the intermediate regrowth shapes are not a function of temperature. Temperature independence of the orientation effect was shown by Csepregi's experiments¹³ for temperature between 500-600 °C. Thus, the regrowth times would scale with temperature (for intrinsic Si) isotropically.

As a proof of concept, a simulation of regrowth (Figure 4-4) for a patterned amorphous trench region (0.2 μm deep and 0.2 μm wide). The velocity expression given in Equation 4-3 was substituted as F in Equation 4-1 for solving the level set equation. Rectangular grid was used with a constant spacing of 0.002 $\mu\text{m} \times 0.002 \mu\text{m}$ and bounding box area of 0.3 $\mu\text{m} \times 0.3 \mu\text{m}$. The boundary conditions for the simulation were: 1) The left and right grid boundaries were reflecting. For the computation of normal and curvature of the boundary nodes, both backward and forward spatial derivatives were required for averaging as shown in chapter 3. Hence, reflecting boundary condition was required so that the boundary nodes would not regrow differently from their neighboring nodes, otherwise, oscillations could start at the boundary. 2) The top surface was not allowed to regrow. The top layer of grid represents the surface of the silicon that usually has native oxide or nitride mask above it. The presence of any material other

than c-Si on the top stops the regrowth of the top surface^{23,55}. This boundary condition had the tendency to create grid dependence for the regrowing side-front near the top surface. But the formation of (111) fronts near the top surface made the regrowth rate became very small (orientation dependence¹³) and thus there was no noticeable grid dependence. 3) The bottom surface was free to regrow depending on the value of function ϕ (though for our case the bottom surface was already c-Si and did not affect the regrowing interface).

Figure 4-4 shows the regrowth patterned amorphous regrowth at various times. The outermost contour is the as-implanted interface of α -c Si. It also shows the pinching of corners in the $\langle 111 \rangle$ directions and a hump in $\langle 001 \rangle$ bottom front. They seem to qualitatively show the same regrowth shapes that were observed in previous studies^{15,18}.

4.3 Experiments and Initial Simulations

For this study, a polished 750 μm -thick impurity-free (001) Si wafer with room temperature resistivity of $\sim 200 \Omega\text{-cm}$ was used. Masked regions consisted of lines $\sim 0.5 \mu\text{m}$ wide aligned along $\langle 110 \rangle$ in-plane directions with 150 nm of Si_3N_4 ($\sim 1 \text{ GPa}$ intrinsic tensile stress) on $\sim 10 \text{ nm}$ of SiO_2 separated by $\sim 0.5 \mu\text{m}$ wide unmasked area between adjacent lines. Samples were Si^+ -implanted at 20 and 60 keV with doses of $1 \times 10^{15} \text{ cm}^{-2}$. This produced an α -Si layer $\sim 120 \text{ nm}$ deep with a rounded α -c interface under the mask edge as shown in the cross-sectional transmission electron microscopy (XTEM) image presented in Figure 4-5a.). From the work of Burbure *et al.*⁵⁵, it is expected that the regrowth interface contacting the SiO_2 layer just under the masking will constrict SPER at that point. Hence, these samples are referred to as having the regrowth interface subjected to surface pinning.

The samples were annealed at a temperature of $T = 500 \text{ }^\circ\text{C}$ in N_2 ambient for times of 0.5 – 4.0 h. Anneal times were chosen to see different points during the regrowth process when the

regrowth evolution showed important changes. Bright-field (BF) cross-sectional transmission electron microscopy (XTEM) imaging using a g_{022} two-beam condition was used to image the regrowth of the α -Si layers and the formation of mask-edge defects. Specimens were prepared via focused ion beam milling (see Chapter 3 for details).

Figures 4-5(a) – (c) present XTEM images of the 2D SPER process at $T = 500$ °C. After annealing for 1 h, the α -c interface has taken on a rectangular shape with the initially round corner area becoming very sharp as shown in Figure 4-5(b). After annealing for 2 h, the regrowth interface near the corner regions has further sharpened as shown in Figure 4-5(c). The level set SPER simulations after 1 and 2 h of annealing based on the orientation dependent regrowth velocity from Equation 4-3 (using $v_{[001]} = 27$ nm/h from Equation 4-2) are shown in Figures 4-5 (e) and (f), respectively, with $v = 0$ specified for the point at which the interface contacts the SiO_2 layer. It is evident from Figure 4-5 that the portions of the regrowth fronts near the corner regions do not match the XTEM images. Specifically, it appears regrowth along $[111]$ is slower in the simulations than actually observed. Furthermore, enhancing the relative regrowth velocity of the $[111]$ direction from ~ 25 times slower than $[001]$ to ~ 15 times slower (as per results from Csepregi *et al.*¹³ who indicated two different velocities for $[111]$ SPER) did not appreciably change the simulated SPER process (not presented). Thus, it appears that differences in the relative regrowth rates of different crystallographic fronts cannot entirely account for the observed SPER evolution.

4.4 Summary

In summary, level set model was implemented for simulating solid phase amorphous regrowth for Si. Simulations done using an isotropic regrowth velocity did not show any qualitative agreement with prior studies^{15,18,26}, thus highlighting the need for adding the effect of

substrate orientation on regrowth. Simulations done including the orientation dependent velocity (by encapsulating the orientation dependence data in a curve fitted factor, $f(\theta)$) did show good qualitative matching with the XTEMs from prior studies^{15,18,26}. An experiment to accurately match the simulations to the XTEMs was done. The simulations showed some differences with the TEM images near the $\langle 111 \rangle$ corners, where the actual regrowth was slower than the simulations showed. Thus, some critical parameter is missing in the simulations that can take into account the mismatch around the corners during regrowth.

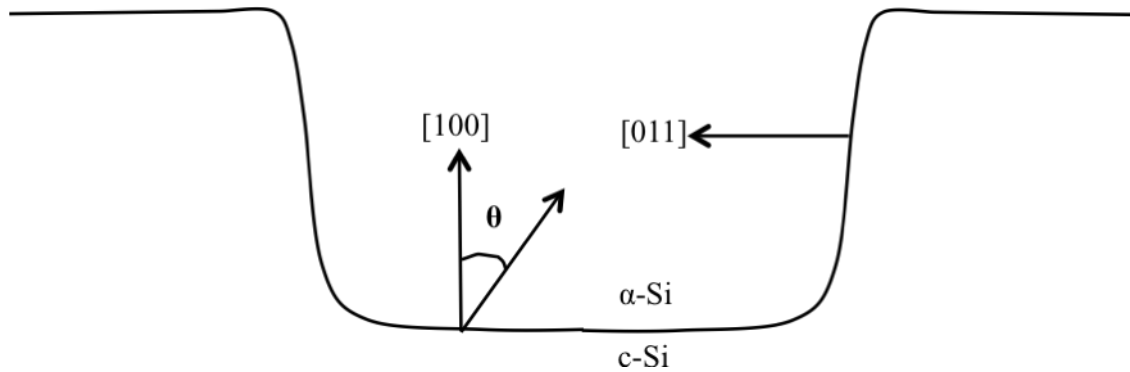


Figure 4-1. As-implanted amorphous-crystalline interface showing various substrate orientations and the surface angle (θ) for orientation dependent factor $f(\theta)$.

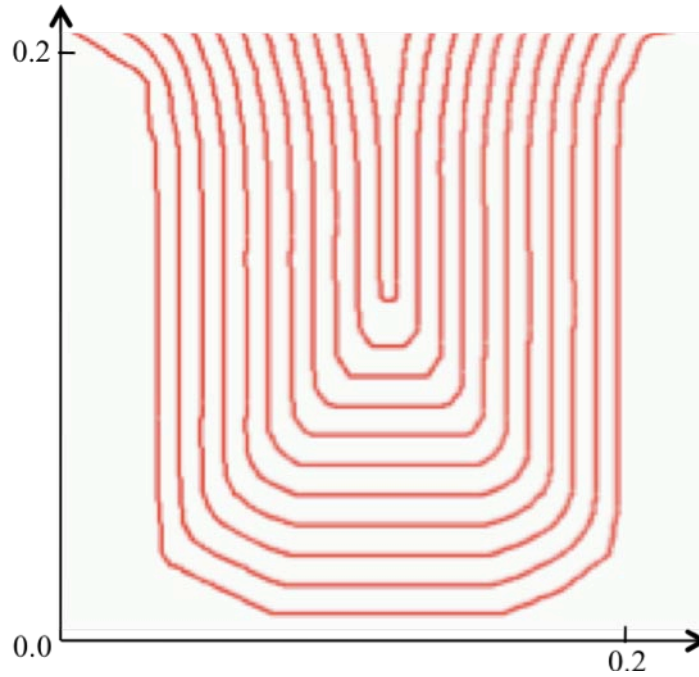


Figure 4-2. Simulation of regrowth using Level Set Methods with isotropic velocity¹⁴. Contours represent the position of α -c interface at different times of regrowth.

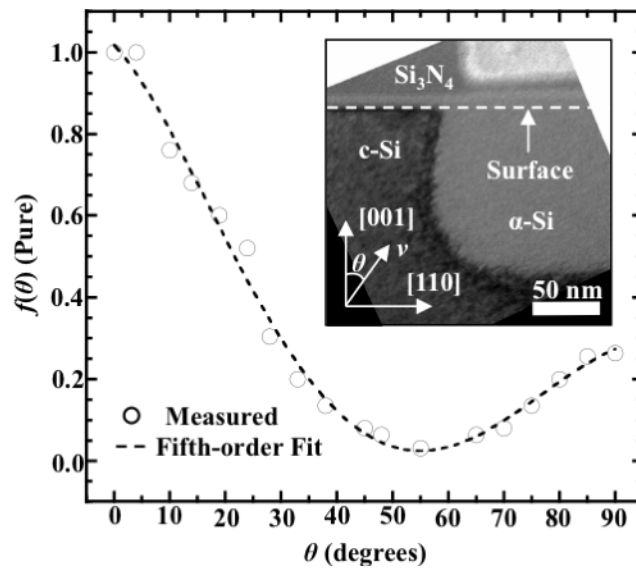


Figure 4-3. The normalized SPER velocity, $f(\theta)$ ¹⁴, as a function of the substrate orientation angle from [001] towards [110], θ , as measured by Csepregi *et al.*¹³. Inset shows an XTEM micrograph of a typical 2D structure where the SPER process occurs.

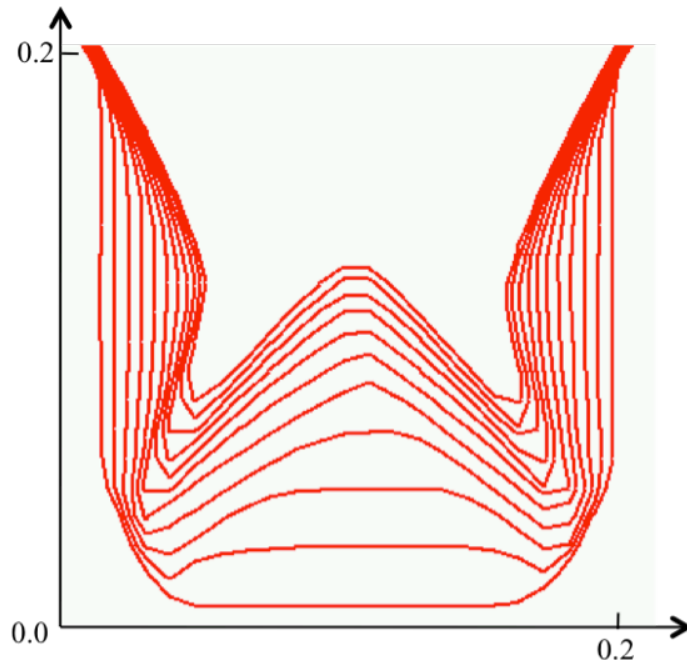


Figure 4-4. Simulation of regrowth with orientation dependence included (velocity from Equation 4-3). Contours represent the α -c interface at different times of regrowth. Region outside the contour is crystalline and inside is amorphous.

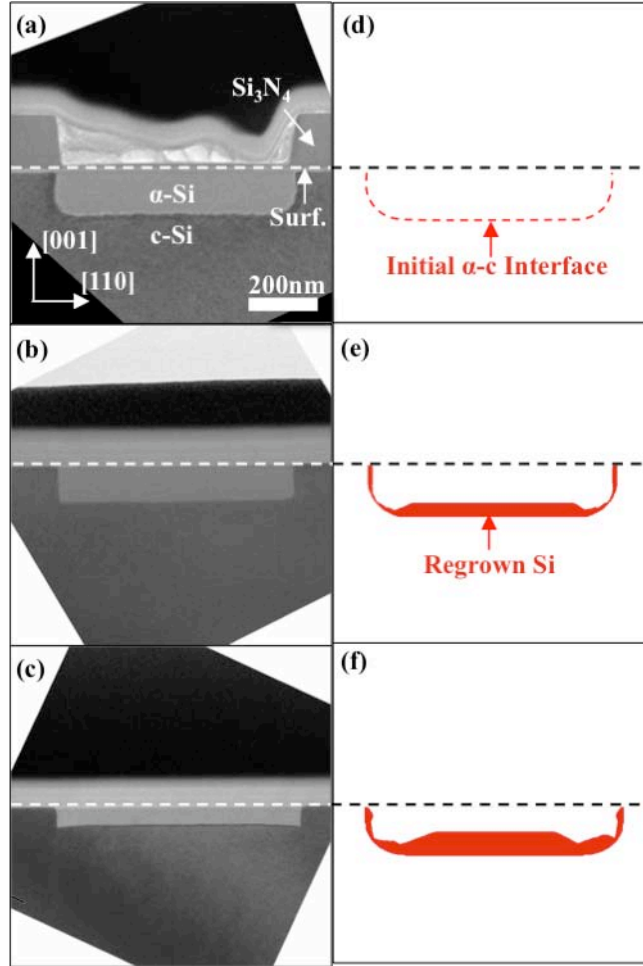


Figure 4-5. The observed and simulated 2D SPER process in a structure with α -c interfacial pinning at the surface at $T = 500$ °C: XTEM images of the structure a) as-implanted, b) after 1 h of annealing and c) after 2 h of annealing. Level set simulations of the structure evolution using only regrowth orientation dependence [Equation (4-3)] d) as-implanted, e) after 1 h of annealing, and f) after 2 h of annealing¹⁴.

CHAPTER 5 ROLE OF CURVATURE PARAMETER IN SOLID PHASE EPITAXIAL REGROWTH OF INTRINSIC SILICON

5.1 Introduction

As was demonstrated in chapter 4, orientation dependence is an important parameter in the simulations for getting the correct shapes of regrowth time-splits. However, it alone is not sufficient for accurately matching the observed results. There seems to be a missing parameter in the velocity function shown in Equation 4-3.

Some of the prior studies^{57,59} have mentioned the role of local interfacial curvature in the regrowth process for Si. This chapter attempts to implement the curvature parameter in the level set simulations and match them up with the observed results of chapter 4. It also critically examines the prior models⁵⁷ that have suggested the role of curvature as a driving force in the regrowth process.

Furthermore, the structure in experiment from chapter 4 includes the α -c interface surface pinning that could affect regrowth shapes. This chapter includes results of an experiment with no interface surface pinning to resolve that issue. The model for 2D SPER of semi-insulating proposed in this chapter also attempts to predict regrowth shapes for various starting α -c interfaces.

5.2 Model for SPER Including Curvature

Chapter 4 highlighted the mismatch of experiments and simulations (with only orientation dependent velocity taken into account) especially around the corner regions. These corner regions are composed {111} and neighboring fronts. Furthermore, these regions are curved implying that they contain some built-in ledges that may move faster than a planar front for the same substrate orientation. This idea was shown in prior work from Drosd *et al.*⁵⁹ where it was observed that local interfacial curvature, κ , affected the regrowth rate of {111} planes. It was

attributed to the fact that {111} interface is smooth and should grow by nucleation and migration of atomic ledges. Hence, if a portion of c-Si is encompassed by α -Si (negative or convex curvature), SPER should be retarded while if the α -Si is encompassed by c-Si (positive or concave curvature) as shown in Figure 5-1, SPER should be enhanced. Furthermore, it was shown that when the radius of curvature, $r = 1/\kappa$, was below $\sim 20 \mu\text{m}$, a measurable increase in regrowth rate occurred. In the presented cases (and in Chapter 4), the growth interface has portions where $r \sim 0.1 \mu\text{m}$. The curvature parameter was implemented as a small component of the driving force in the SPER velocity functions as shown in Equations 2-7 and 2-8 by Phan *et al.*⁵⁷. The model was however never tested in cases of high interface curvature (i.e. very small radius of curvature). In most of those relatively planar structures, the effect of curvature factor was overwhelmed by the orientation dependence or the external stress factors. When Equation 2-7 was tested against experimental results of Chapter 4, it could not reproduce the corners (the same way as Equation 4-3 could not). The curvature parameter in Equation 2-7 was too small to have any effect on the regrowth shapes. Thus, a new model for curvature was needed. A simplistic linear function for modeling curvature was tested using level set simulations. The Equation 4-3 was thus modified to include curvature as following

$$v(\theta, \kappa) = v_{[001]} f(\theta) (1 + A\kappa) \quad (5-1)$$

where A is a constant with units of length. For the presented work $A = 2.0 \times 10^{-7} \text{ cm}$ was used. Equation (5-1) was used for level set simulation of the 2D SPER process at $T = 500 \text{ }^\circ\text{C}$ in samples with surface regrowth interface pinning as shown in Figure 5-1. After annealing for 1 h, the XTEM image and level set simulation of SPER shown in Figures 5-1(b) and 5-1(f) are in good agreement. This is also the case after annealing for 2 h as shown in Figures 5-1(c) and 5-1(g) as well as after annealing for 4 h as shown in Figures 5-1(d) and 5-1(h). The pinching of the

corners leading to the formation of mask-edge defects is also noticeable in Figure 5-1(h) something that has been seen in previous works as well^{15,18,19,22}. The annealing was done with and without the Si₃N₄ mask to alienate the effect of stress from the Si₃N₄ mask on SPER. The regrowth shapes (not presented) did not show any difference in the two cases. Since, stress is known to affect regrowth rates^{22,37,41} as well as regrowth shapes²² in patterned wafers, the result presented above suggests that the stress transferred from the Si₃N₄ mask to the regrowing Si was small.

5.3 Curvature Confirming Experiment and Simulation

The implication of Equation (5-1) is that portions of the regrowth interface with $\kappa > 0$ ($\kappa < 0$) should have enhanced (reduced) velocity. It is evident from Figure 5-1 (surface interfacial pinning) that Equation (5-1) appears to be valid for the case of $\kappa \geq 0$ since most of the regrowth front is of this type. However, the converse is not necessarily evident.

For confirming the validity of the model in case of $\kappa < 0$, another experiment was done. Cartoon in Figure 5-2(a) shows the patterned and amorphized wafer from experiment described in section 4.3 that was used as the starting wafer for further processing. The samples were Si⁺-implanted at 160 keV with a dose of 3×10^{15} cm⁻² to generate an undulating α -Si layer ~100 nm thick under the masking and ~300 nm thick in the open areas as shown in Figure 5-2(c). In this case, the regrowth interface is not in contact with any portion of the surface and is therefore not subjected to any surface pinning. Thus, these samples are referred to as being without regrowth interface pinning.

To test the influence of $\kappa < 0$ on the 2D SPER process, structure lacking interfacial pinning, shown in Figure 5-3, was annealed at $T = 500$ °C in a N₂ ambient up to 10 h. It can be readily seen that both concave and convex portions of the regrowth interface exist in this structure and both are oriented in the same direction (close to <111> direction). After annealing

for 2.5 h, shown in Figure 5-3(b), the concave portion of the interface becomes sharp while the convex part begins to flatten. After annealing for 5.0 h, as presented in Figure 5-3(c), mask edge defects started to form as the corner region of the interface has impinged upon itself. Following annealing for 10.0 h, shown in Figure 5-3(d), two triangular α -Si regions remained under the mask edge. It is noticeable in all the XTEM images that mask edge defects show up only when the corner becomes very sharp and the angle between the two merging fronts becomes equal to or less than 90° . This experiment also proves that the regrowth shape and the defect formation are not related to the α -c interface being pinned at the Si-SiO₂ interface (because that constraint was removed in this experiment and the defects still formed).

Level set simulation of the 2D SPER process at $T = 500^\circ\text{C}$ in structures without interfacial pinning was done assuming Equation 5-1 to be valid. In all cases of annealing, the simulated SPER process, shown in Figures 5-3(f) – (h), matches very well with the corresponding XTEM images, shown in Figures 5-3(b) – (d). The simulations did not take into account the regrowth rate reduction (if any) due to the formation of mask-edge defects. However, the parameters used in the simulations were enough to predict the shapes of regrowth before and after the formation of mask-edge defects. This suggests that mask-edge defects do not lead to the creation of pinching corners but it is vice-versa. It also suggests that mask-edge defects do not significantly affect the regrowth rate.

The TEM images also showed a suppression of the SPER velocity below the Si₃N₄ pad near the Si interface. This is consistent with some prior work⁴⁰ which attributed the slowing down to two probable effects: 1) The rigidity of the Si₃N₄ could reduce the mobility of the Si atoms at the underlying α -Si/Si interface, slowing the rate at which they arrive at the lattice sites appropriate for recrystallization. 2) The SPER might be slowed down by a higher concentration

of Si-H bonds under the Si_3N_4 features, since Si_3N_4 can act as a source of H that is lost during the densification process of Si_3N_4 . The suppression of SPER velocity due to the presence of H has been well documented^{75,76}. However, the regrowth rate showed (not presented) the same slowing down even with the Si_3N_4 pads stripped off before annealing. Thus, some other effect was responsible for the slowing down.

As mentioned in section 2.1.3, nitrogen (N) is known to suppress SPER rate⁴⁶. Thus, the presence of N recoils during the last amorphizing implant (Si^+ 160 keV energy, $3 \times 10^{15} \text{ cm}^{-2}$ dose) could be responsible for the effect. CTRIM (crystal trim of formerly called software ISE-FLOOPS) simulations were done to figure out the concentration and depth of the N profile created during amorphization. The simulations showed N profile tails off within 60 nm of the Si surface. Literature values⁴⁶ were used to incorporate slowing down of the regrowth in the presence of N atoms as shown in Figures 5-3 (f)-(h) and they had a perfect matching with the TEM images as shown in Figures 5-3 (b)-(d). It is also notable that since N profile is far from the areas of high curvatures (both concave and convex), the slowing down of regrowth near the surface did not in any way affect the evolution of regrowth in high curvature areas. Thus, the effect of N on curvature (if any) did not have to be taken into account. The effect of dopants on curvature parameter has been further discussed in Chapter 6.

The 2D SPER process in samples without interface pinning was also examined at $T = 575$ °C using XTEM to see the effect of temperature on regrowth shapes and hence on the curvature parameter. The results are shown in Figure 5-4. In this case, the SPER evolution was faster (as expected due to the thermally-activated²⁷ nature of SPER) but the shape of the regrowth interface was nearly identical to the case of $T = 500$ °C. The presence of mask-edge defects at the same depth is another indication that the pinching of the corners happened at the same depth.

The implication is that the apparent influence of interfacial curvature on SPER is nearly temperature-independent. Beyond this temperature, the regrowth would be very fast and it would not be possible to take various time-splits during regrowth.

5.4 Interpretation of the Curvature Factor in SPER

Even though curvature factor was implemented as a fitting parameter, some prior atomistic modeling work on regrowth by Marques *et al.*^{60,61} supports the idea of curvature. As shown in Chapter 2, the model suggests the presence of bond-defects as the reason for amorphization. The bond-defect is also known as I-V pair or Interstitial-Vacancy pair because of the inability of an interstitial and a vacancy (migrating towards each other) to recombine in a crystalline semiconductor. The activation energy for the recombination of an isolated I-V pair is 0.43 eV^{60,61}, which would imply a very fast recombination of the interstitial and a vacancy. The activation energy, however, becomes larger as more I-V pairs surround the I-V pair. The accumulation of these I-V pairs leads to the formation of amorphous region. The activation energy dependence on the neighboring I-V pairs is given in Equation 2-9. It is evident from the model that a planar interface would regrow faster than a convex interface (a portion of c-Si is encompassed by α -Si) because the planar interface would have less neighboring I-V pairs than the convex interface. The converse is true for a concave interface (a portion of α -Si is encompassed by c-Si). Comparison between the I-V pair model and the one presented in Equation 5-1 is difficult. The linear interpolation of I-V pairs to the curvature would give different results in the two cases, since the I-V pair model would then include the curvature term in the activation energy. This would mean different effect of the curvature at different temperatures (with respect to planar). However, experiments done at different temperatures (Figure 5-4) suggest no difference in the regrowth shapes and the mask-edge defect depth. Hence, only qualitative agreement is sought from the I-V pair model for the curvature parameter.

Another supportive argument for the curvature implementation comes from the ledge based regrowth theory (recently confirmed by Rudawski *et al.*^{21,37-39}). The theory states that regrowth is mediated by crystal island nucleation with subsequent island ledge migration. It also states that in-plane migration involves the coordinated motion of atoms along a growing island ledge. Figure 5-5 shows the formation and migration of ledges. The fact that the bottom front propagates by nucleation and migration of ledges leads to a sharpening of the corner at the concave curvature. However, on the upper front near the convex curvature, the ledge migration does not help the regrowth of the corner. Instead, it makes the convex front more planar and leads to the formation of (111) fronts that are slow regrowing. The above process can be simulated on a macroscopic scale using the curvature factor along with orientation dependence as shown in Equation 5-1.

Prior simulation work by Phan *et al.*⁵⁷ advanced that the curvature of a regrowth interface does not influence the activation barrier for SPER. Additionally, Phan *et al.*⁵⁷ addressed the influence of curvature on the driving force for recrystallization and determined it produced a negligible impact on the regrowth kinetics. However, though thermodynamic considerations may be negligible, it does appear from the work presented herein that interfacial curvature is altering SPER kinetics. Perhaps no curvature effect was observed because of the relatively planar nature of the structures used in the prior work.

In terms of explaining the apparent linear dependence of the SPER velocity with interfacial curvature observed herein, it is useful to consider the likelihood of the α -c interface having an inherent amount of internal tension as has been suggested by others^{77,78}. Thus, it is foreseeable that portions of an interface with non-zero curvature would experience localized stresses much different from the case of an interface with zero curvature. Furthermore, it has

been well established that stress on the regrowth interface can significantly alter the kinetics of SPER due to changes in volume associated with the process^{19,34,40,41,51,53,79}. Hence, it is possible that interfacial curvature is influencing the localized stress states on the interface and altering regrowth.

5.5 Predicting 2D Regrowth Shapes

The 2D SPER model from section 5.2 has successfully simulated regrowth shapes for different as-implanted α -c interfaces for various temperatures. Thus, the capability was tested to predict the regrowth shapes of some other α -c interfaces that would be helpful in device engineering.

Figure 5-6 shows the simulated 2D SPER process in samples with surface interface pinning at different initial values of r under the mask edge with the same initial α -Si thickness of ~ 150 nm. As r increases, it is more difficult for the regrowth interface to collapse upon itself (and thus form mask edge defects). In fact, this prediction is verified by a prior study in which a sine wave-type regrowth interface with very low amplitude completely flattened after sufficient annealing and exhibited no defects^{34,51}. Thus, the model can be used to successfully predict the formation of mask edge defects depending on the initial α -c interface shape. The result is very important from the semiconductor industry perspective, for reducing the mask-edge defects that have known increase leakage current⁸⁰. Angled implants are very common during CMOS device fabrication for the formation of source-drain extension implants or halo implants. Thus, creation of initial amorphous shapes as shown in Figure 5-6 for alleviating mask-edge defects can be easily integrated in the device fabrication process.

The model described in section 5.2 gives some insight into the regrowth when the amorphous trench depth or width is varied. It is intuitive to see that increasing or decreasing the

width (W) or depth (D) of the amorphous region while keeping the width-to-depth (W/D) ratio constant will not affect the regrowth shapes. However, varying the W/D ratio leads to very different regrowth shapes. Figure 5-7 shows different starting α -c interfaces with varying W/D ratios (W varying, D stays constant). The contours represent the various stages of regrowth starting with a perfectly rectilinear amorphous shape. The first noticeable feature of regrowth in all four cases is that the pinching of the corners takes place at same depths. The pinching of the corners happens due to the merging of the side and the bottom fronts and the inability of the encompassed regrowing α -Si corner to add to both the fronts while maintaining a perfect atomic registry. However, that is totally dependent on the starting α -c interface shape and the amorphous depth as was shown in Figure 5-6.

Nevertheless, the regrowth beyond the pinching of the corners is highly dependent on W/D ratio. Figure 5-6 (a) shows the case with $W/D = 2.5$ and represents all the cases where $W/D > 2$ (all will have similar regrowth shapes). The figure shows the flat bottom (001) front reaching the surface as a flat (001) front. The side fronts composed of (110) planes can be seen encroaching from the sides and the pinching of the (111) corners can also be seen. The flat bottom reaching the top surface leaves behind two triangular amorphous regions composed of (111) fronts that finally regrow very slowly and with defects. This has been observed in prior experiments^{15,22}.

Figures 5-6 (b) and (c) show regrowth with $W/D = 2$ and $W/D = 1.5$ respectively. The bottom regrowing front in the two cases is not able to reach the surface a flat front. Instead, it converts into two slow regrowing (111) fronts that slow down the regrowth at the center of the pattern.

Figure 5-6 (d) shows regrowth for $W/D = 1$ and is representative of the regrowth shapes for cases with $W/D < 1$. In this case, the regrowth was controlled by the side fronts which collapsed into each other to create an inverted V-shape of amorphous region at the center that is composed of slow growing (111) fronts. Since, the propagation of the α -c interface can influence the dopant profile by dopant segregation⁸¹, diffusion^{30,31,82} etc. it is essential to know the α -c interface shapes during regrowth.

5.6 Summary

In summary, a model for 2D SPER for semi-insulating Si was proposed. The model from Chapter 4 considered only orientation dependence of regrowth, but that approach failed to accurately predict the evolution of regrowth process in structures where the regrowth interface was pinned at the surface. However, modifying the orientation dependent regrowth model to also be linearly dependent on local interface curvature did accurately account for regrowth evolution. This same curvature dependence was also successful in predicting the regrowth evolution in structures where regrowth interface pinning was not present. Interestingly, the apparent linear dependence of regrowth kinetics on interface curvature was temperature insensitive. The regrowth model was also used to predict the regrowth for different starting α -c interfaces. This included varying the initial curvature of the α -c interfaces and varying the width-to-depth (W/D) ratio of the amorphous region. The simulations gave an insight about the evolution of regrowth shapes and how different starting α -c interfaces could be used for the betterment of device fabrication and performance.

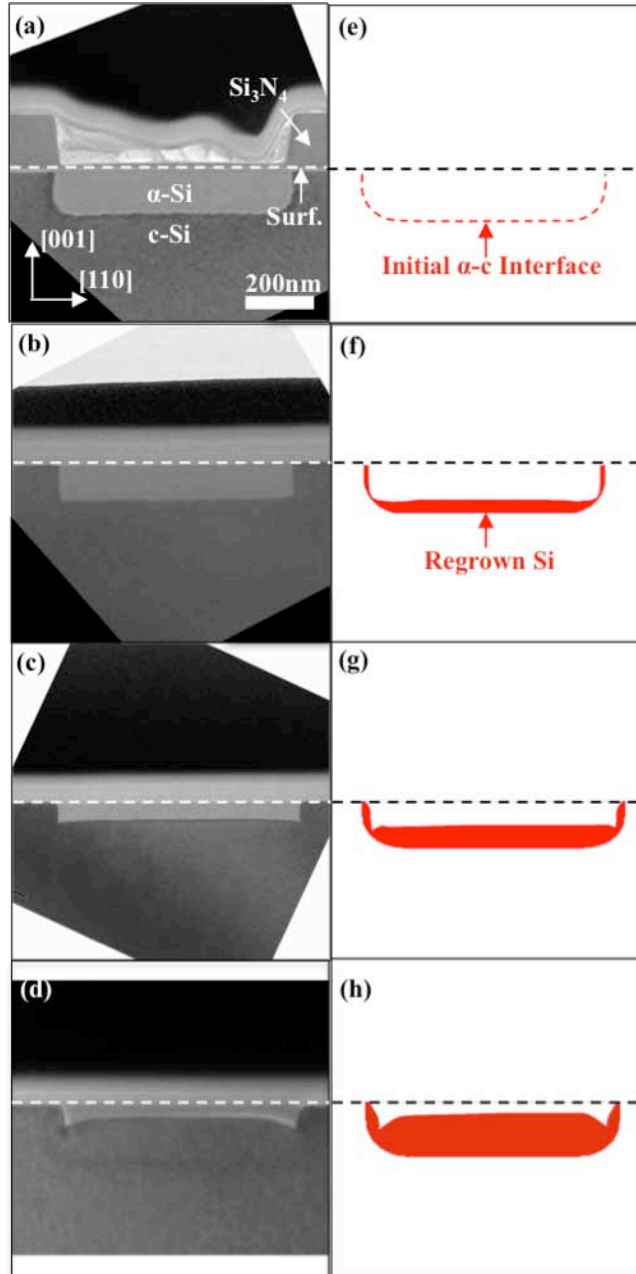


Figure 5-1. The observed and curvature-included simulated 2D SPER process in a structure with α -c interfacial pinning at the surface at $T = 500$ °C: XTEM images of the structure a) as-implanted, b) after annealing for 1 h, c) after annealing for 2 h, and d) after annealing for 4 h. Level set simulations of the structure evolution using both regrowth orientation and interfacial curvature dependence [Equation 5-1] for e) as-implanted f) after annealing for 1 h, g) after annealing for 2 h, and h) after annealing for 4 h.⁵⁶

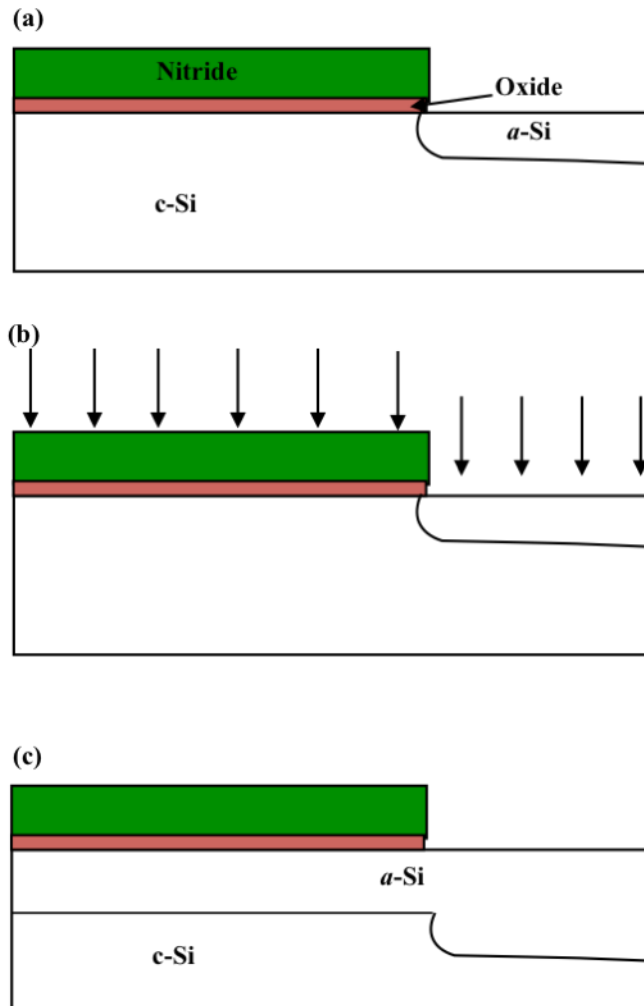


Figure 5-2. Shows cartoons for creating a structure without α -c interfacial pinning: a) The starting wafer with patterned amorphous region with α -c interfacial pinning, b) Ion-Implantation of the wafer by Si^+ with 160 keV energy and $3 \times 10^{15} \text{ cm}^{-2}$ dose (with the mask still present), c) The as-implanted structure without α -c interfacial pinning with an undulating α -Si layer $\sim 100 \text{ nm}$ thick under the masking and $\sim 300 \text{ nm}$ thick in the open areas.

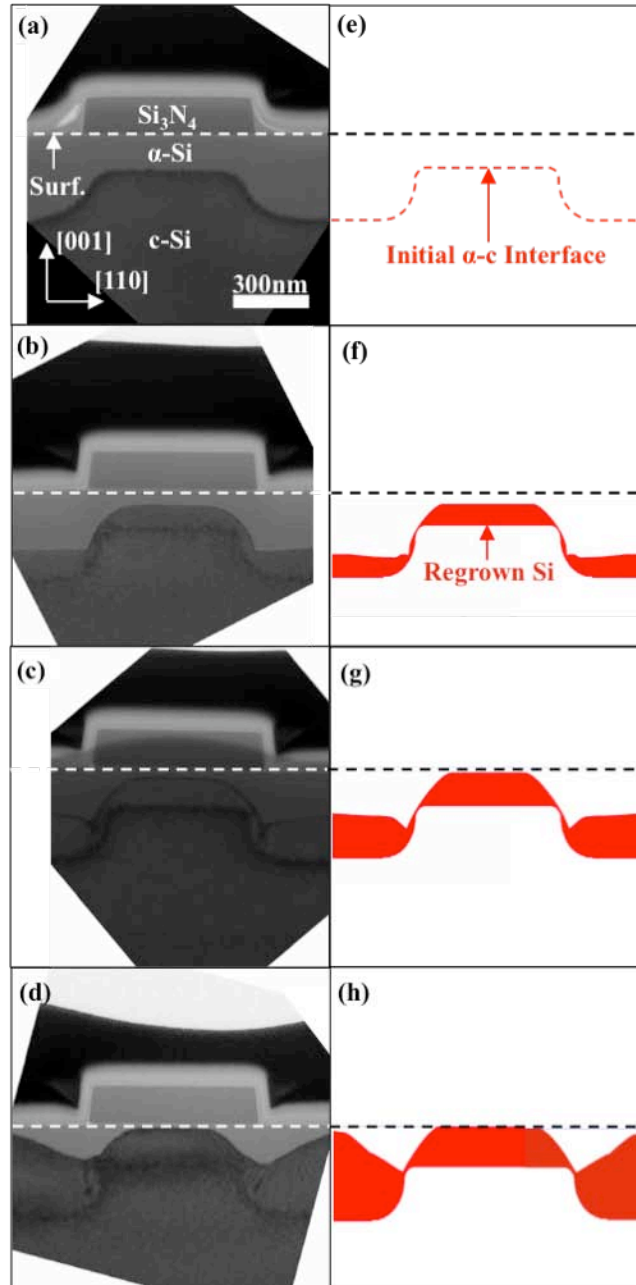


Figure 5-3. The observed and curvature included simulated 2D SPER process in a structure without α -c interfacial pinning at the surface at $T = 500$ °C: XTEM images of the structure a) as-implanted, b) after annealing for 2.5 h, c) after annealing for 5.0 h, and d) after annealing for 10.0 h. Level set simulations of the structure evolution using both regrowth orientation and interfacial curvature dependence [Equation 5-1] e) as-implanted, f) after annealing for 2.5 h, g) after annealing for 5.0 h, and h) after annealing for 10.0 h ⁵⁶.

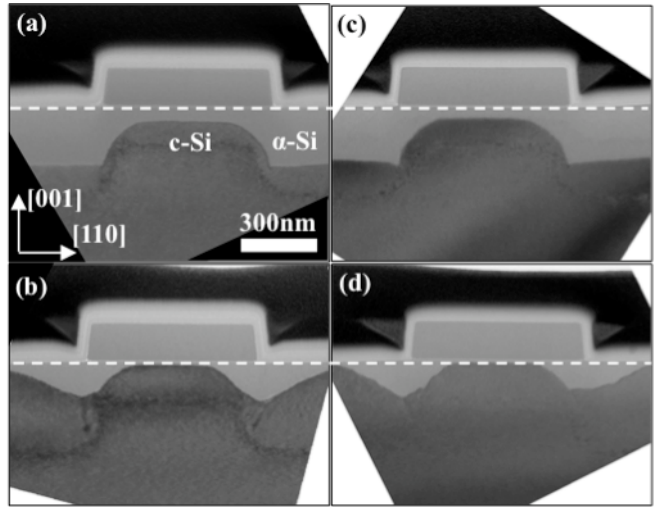


Figure 5-4. 2D SPER shapes showing no dependence on temperature in a structure without α -c interfacial pinning at the surface: XTEM images of the structure for $T = 500 \text{ }^\circ\text{C}$ a) after annealing for $t = 2.5 \text{ h}$, b) after annealing for $t = 10 \text{ h}$, for $T = 575 \text{ }^\circ\text{C}$ c) after annealing for $t = 10 \text{ mins.}$, d) after annealing for $t = 20 \text{ mins.}$

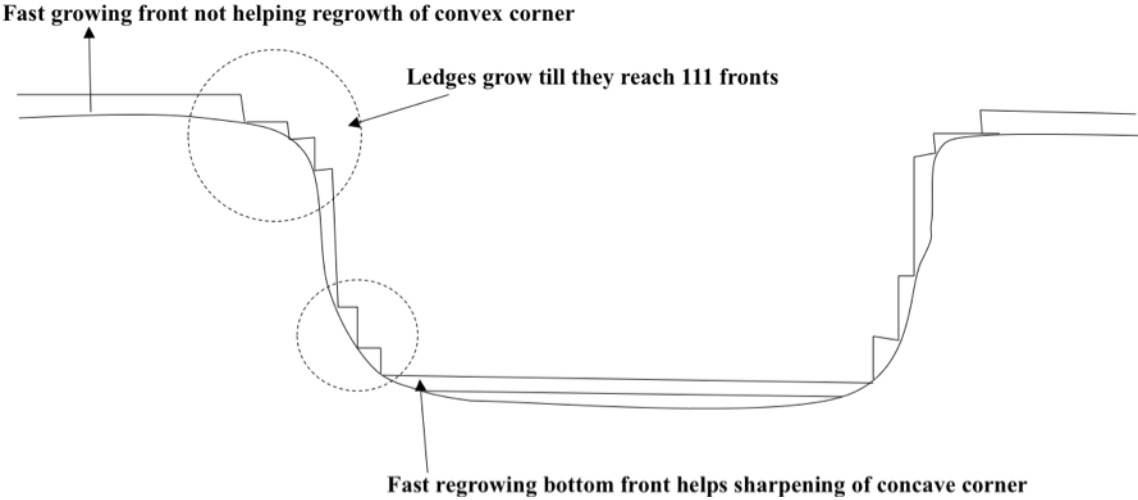


Figure 5-5. Cartoon depicting the ledge theory argument for the 2D SPER of a structure without α -c interfacial pinning.

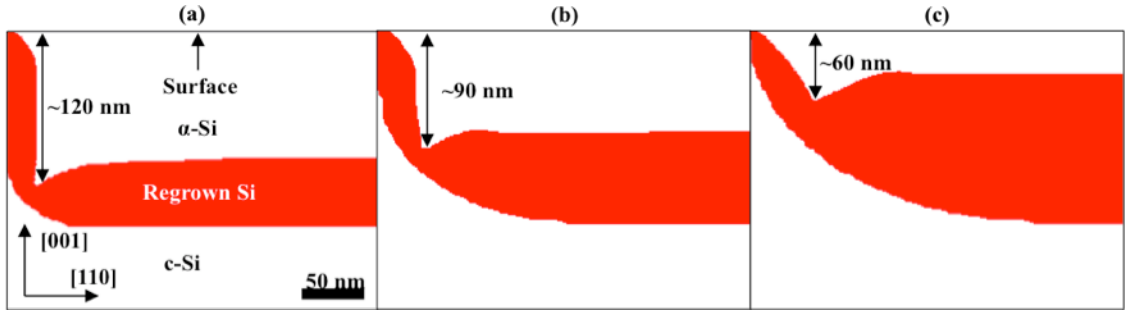


Figure 5-6. The effect of initial α -c interface curvature near the corner region on the level set simulations using both regrowth orientation and interfacial curvature dependence [Equation 5-1] of the 2D SPER process in a structure with α -c interfacial pinning at the surface: $r =$ a) 40 b) 80 and c) 120 nm⁵⁶.

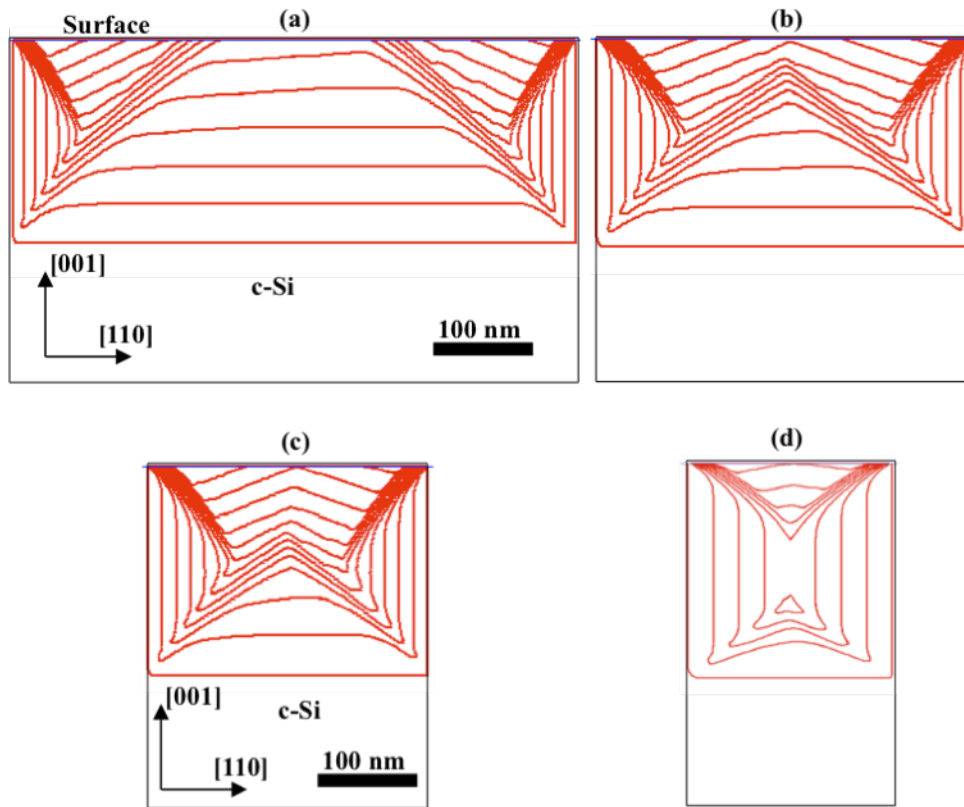


Figure 5-7. The effect of initial α -c interface width-to-depth (W/D) ratio on the regrowth shapes for 2D SPER using level set simulations [Equation 5-1], a) W/D = 2.5, b) W/D = 2, c) W/D = 1.5, d) W/D = 1.

CHAPTER 6 DOPANT EFFECT ON SOLID PHASE EPITAXIAL REGROWTH OF SILICON

6.1 Introduction

Chapters 4 and 5 provide the velocity expression for SPER of semi-insulating Si. However, the source and drain regions where SPER is typically known to happen in a CMOS device are heavily doped. It was also mentioned in the Chapter 2 that dopants of both n and p-type strongly enhance the SPER velocity in Si. The dopant related enhancement of SPER velocity has been known to be an electronic process because both p and n-type dopants increase the rate when present separately and no enhancement is observed when both are present together. The GFLS (generalized Fermi level shifting) model^{28,29,47,75,76} attributes the enhancement of SPER velocity to the increase in the density of charged defects.

However, most of the experimental work in studying the dopant effect on SPER has been on planar interfaces^{28,29,47,75,76}. Only a few prior studies have studied the effect of dopants on patterned regrowth²⁰. These studies suffer from the non-uniformity of dopant profiles in the depth direction because of ion-implantation of dopants. Subsequently, the various regrowth fronts in the patterned α -c interface are affected by different dopant concentration. In addition to that the dopants suffer from diffusion during regrowth in case of non-uniform doping. Also, in light of the curvature factor suggested in Chapters 4 and 5, it is extremely important to have a constant doping in the structure to make any useful conclusions about the effect of doping on patterned SPER. This Chapter shows the effect of Arsenic (n-type) and Boron (p-type) on the velocities of various substrate orientations. In addition to that, the effect of dopants on the curvature effect is also studied.

Apart from the dopants affecting the SPER, the SPER also affects the dopant profile by diffusion and segregation^{30,31,81,82}. Some dopants like Boron (B) have known to diffuse

significantly more in the amorphous Si as compared to crystalline Si (diffusivity difference ~five order of magnitude)^{30,31,82}. Thus, SPER was simulated simultaneously with dopant diffusion in FLOOPS and some interesting results were seen.

6.2 Experiment for Dopant Effect on SPER

For this work the experimental design was similar to the one shown in section 5.3. However, semi-insulating wafer ($\rho \sim 250 \text{ } \Omega\text{-cm}$) was used as a control for the p-type ($\rho \sim 0.003\text{-}0.004 \text{ } \Omega\text{-cm}$) and n-type ($\rho \sim 0.003\text{-}0.004 \text{ } \Omega\text{-cm}$) wafers. The n and p-type wafers were chosen with very low resistivity to see the maximum effect of dopants on regrowth shapes. These 500- μm thick (001) Si wafers were patterned using masked regions that consisted of lines $\sim 0.5 \text{ } \mu\text{m}$ wide. The lines were aligned along $\langle 110 \rangle$ in-plane directions with 150 nm of Si_3N_4 separated by $\sim 0.5 \text{ } \mu\text{m}$ wide unmasked area between adjacent lines (due to some under etch, the unmasked areas had $\sim 20 \text{ nm}$ nitride left as shown in Fig. 6-1. We will still refer to it as unmasked region for clarity). All the samples were Si^+ -implanted at 20, 60, and 160 keV with doses of 1×10^{15} , 1×10^{15} , and $3 \times 10^{15} \text{ cm}^{-2}$ to generate an undulating α -Si layer $\sim 70 \text{ nm}$ thick under the masking and $\sim 230 \text{ nm}$ thick in the unmasked areas as shown in Fig. 6-1. As with the prior experiment⁵⁶, this as-implanted regrowth interface includes both convex and concave curvatures. The regrowth interface is not in contact with any portion of the surface and is therefore not subjected to any surface pinning effect which would constrict the regrowth of interface contacting the Si_3N_4 ⁵⁵.

All the samples were annealed at $500 \text{ } ^\circ\text{C}$ in N_2 ambient. The semi-insulating samples were annealed for times 0.5 – 10.0 h. Anneal times were chosen to see different points during the regrowth process when the regrowth evolution showed important changes. Since, the n and p-type dopants are known to increase planar regrowth rates²⁷, appropriate anneal times were chosen depending on the doping concentration to catch regrowth at similar points as the semi-

insulating case. XTEM imaging was used to image the 2D SPER process with XTEM specimens prepared via focused ion beam milling.

Fig. 6-1 shows the as-implanted XTEM image for the experiment that includes both n and p-type low resistivity wafers in addition to the semi-insulating (same as-implanted for all three cases). Figures 6-2 (a)-(c) show the regrowth of semi-insulating sample at $T = 500^{\circ}\text{C}$ and $t = 2.5\text{ h}$, 5.0 h and 10.0 h respectively (very similar to experiment in section 5.3). The sharpening of the concave corners and flattening of the convex corners is visible at 2.5 h. The pinching of the [111] corner leading to the formation of mask-edge defects can be observed at 5.0 h and 10.0 h. The regrowth however slows down as the interface approaches the surface at 10.0 h when compared to Figure 5-3 (d) where the bottom (001) front had reached the Si surface leaving behind two triangular α -Si regions. The presence of the thin Si_3N_4 in the unmasked region (something that was absent in Figure 5-3 (d)) is responsible for this slowing down. Saenger *et al.*⁴⁰ explained the slowing down of regrowth below a Si_3N_4 layer to the body effect (arising from the rigidity of Si_3N_4 layer) or a localized increase in α -Si hydrogen concentration. The presence of nitrogen recoils from the ion-implantation of Si is possibly responsible for the slowing down as well (since N is known to cause slow regrowth rate⁴⁶). However, the slowing down takes place closer to the surface that is far from the pinching concave corner (the region of interest) so it does not affect the validity of our results.

Figures 6-2 (d)-(f) show the regrowth of n-type sample at $T = 500^{\circ}\text{C}$ and $t = 1\text{ h } 40\text{ min}$, $3\text{ h } 20\text{ min}$ and 6 h respectively. The n-type dopant was Arsenic and the doping concentration was found to be $\sim 7 \times 10^{19}\text{ cm}^{-3}$ (from resistivity values). This resulted in a planar regrowth velocity enhancement of ~ 2 times²⁸. Hence, the regrowth times were chosen to be almost half of the semi-insulating case. The XTEM images showed no difference from the corresponding semi-

insulating case. The same amount of pinching was observed in the concave corners and the defects formed at the same depths.

Figures 6-2 (g)-(i) show the regrowth of p-type sample (B) at $T = 500^{\circ}\text{C}$ and $t = 40\text{ min}$, $1\text{ h } 20\text{ min}$ and $2\text{ h } 40\text{ min}$ respectively. The p-type dopant was Boron and the doping concentration was found to be $\sim 4 \times 10^{19}\text{ cm}^{-3}$. This resulted in a planar regrowth velocity enhancement of ~ 4 times. The XTEM images, like n-type case, showed no change in shape of regrowth. The defects still formed at the same depth. The last regrowth split at $2\text{ h } 40\text{ min}$. seems a little different from its counterparts because once the mask-edge defects are formed, the regrowth of the defective corner can have some variations. However, it is clear that the regrowth shapes that lead to the pinching of the corner are the same for all cases.

The charged defects that lead to the enhancement of regrowth rate enhancement are believed to come from the dopants. However, at higher processing temperatures the intrinsic carrier concentration (n_i) rises exponentially with temperature³ and the Fermi level (E_F) approaches the intrinsic Fermi level (E_i). Thus, it is important to confirm that the intrinsic carrier concentration and the Fermi level fall within reasonable assumptions of the GFLS model shown in Chapter 2. The computed n_i at $T = 500^{\circ}\text{C}$ (used in presented work) was $1.1 \times 10^{18}\text{ cm}^{-3}$ which is almost an order of magnitude lower than the dopant concentration of the n and p-type wafers used in the presented work. Thus, the enhancement in regrowth rate is dominated by the charged defects due to dopants.

The band gap of Silicon (E_G) at $T = 500^{\circ}\text{C}$ was found to be $\sim 0.96\text{ eV}$ that is less than 1.12 eV at room temperature (25°C). According to Johnson³, degenerate semiconductor statistics are required at the dopant concentrations used in the presented work and the Fermi level (E_F) was found to be $\sim 0.16\text{ eV}$ below the conduction band for Arsenic (As) with $\sim 7 \times 10^{19}\text{ cm}^{-3}$ doping

concentration at $T = 460^{\circ}\text{C}$. Interpolating from the graph shown in ³, the degeneracy factor (g) for As in the presented work is 0.5 and E_n^p , the defect energy level responsible for regrowth rate enhancement is ~ 0.15 eV below the conduction band edge. This makes sense since for a regrowth rate enhancement of ~ 2 from As, the $E_F - E_n^p$ needs to be ~ 0.015 eV. The case is similar for Boron.

6.3 Discussion

The implication of the SPER shapes being the same for all three cases (semi-insulating, n-type and p-type) is twofold:

- 1) Dopants increase the planar regrowth rate isotropically (Figure 6-3).
- 2) The electronic effect that is known to control the enhancement of regrowth rate due to dopants has to be independent of the curvature effect (Figure 6-4).

The first conclusion being that the enhancement is isotropic implies that the Csepregi's ¹³ regrowth data curve shifts upwards in the presence of dopants. It also suggests that the defects that are responsible for the rate enhancement are the same for all orientations. This conclusion is understandable because the enhancement is known to be a Fermi-level effect ^{28,29,47}. Since Fermi-level is known to be a function of the material and not the orientation, the results are in conformity with literature.

The second conclusion is that the curvature effect and the dopant “electronic” effect are independent of each other. Figures 6-4 (a)-(c) show the simulations of regrowth with varying curvature parameter $A = 4\text{e-}7$ cm, $6\text{e-}7$ cm and $8\text{e-}7$ cm respectively (keeping all other parameters constant). As the curvature parameter increases, the pinching of the corner reduces. No pinching implies no mask-edge defects. Experimentally, this was shown to happen in the presence of external in-plane uniaxial tensile stress ^{22,26,79} (higher stresses in corners because the

stress-curvature relationship implies stronger effect in the corners). However, no such effect was seen in the presence of dopants only. Hence, Equation 5-1 has been modified to include the effect of dopants as:

$$v(\theta, \kappa, \text{dopant}) = v_{[001]} f(\theta) F(\text{dopant}) (1 + A\kappa) \quad (6-1)$$

where, $F(\text{dopant})$ is the Fermi-level dependent regrowth rate enhancement given in Equation 2- , $v_{[001]}$ is the value of v along [001], $f(\theta)$ is the orientation dependent factor, κ is the localized curvature of the α -c interface and A is the curvature parameter. The dopant concentration for every node on the Level set grid is acquired at every time step to be fed into the $F(\text{dopant})$ factor. Thus, any changes in the dopant concentration due to diffusion or segregation are refreshed into the velocity expression to get an accurate dopant effect on rate enhancement.

The simulations showed that changing the parameter A from 2.0×10^{-7} cm to 4.0×10^{-7} cm did not make much difference in regrowth shape. However, increasing A beyond 4.0×10^{-7} cm changed the regrowth shape significantly as shown in Figure 6-4. When A reaches 8.0×10^{-7} cm (Figure 6-4 (c)), there is no pinching of the corner. Since the planar regrowth rate enhancement from Boron was ~ 4 times and no change in regrowth shape was seen, curvature effect can be said to be independent of the electronic effect within a reasonable error window. It would be nice to have a much higher dopant effect to make this error window smaller. However, with increased doping (for p-type dopants like Boron), stress effects from the dopants⁸³ can start affecting the regrowth as well and that will make it difficult to isolate the different effects.

6.3 Linking Diffusion and SPER

SPER for Si for temperatures in the range of 500-650 °C is much faster than dopant diffusion in crystalline Si²⁷. However, dopants like Boron have shown a significantly higher diffusivity in amorphous Si. The high diffusivity of Boron in amorphous Si makes diffusion a

competing process with the SPER and the combination of the two processes determines the final Boron profile after the SPER has completed. Boron segregation and clustering are also known to affect the final Boron profile, however concentration dependent diffusion has been known to be the most important factor in determining the final profile of the dopant^{30,31,82}. The capability of FLOOPS was used to simulate different diffusion on either side of the α -c interface, with negligible diffusion on crystalline side and concentration dependent diffusion on the amorphous side. The interface of the amorphous-crystalline Si moved simultaneously as time progressed (using Level set method).

Simultaneous implementation of Level set method and diffusion required the coupling of the time steps of the two processes. The level set time step was kept constant and limited by the stability condition (CFL stability criterion⁵⁸). The criterion states that for stability the time step cannot be big enough for the level set to move more than one grid spacing. The diffusion was manually initialized from a small time step that doubled in value if the initial guess was good and halved otherwise. The time steps of the two processes were looped so that the smaller time step controlled the simulation time. Furthermore, Level set was implemented on rectangular mesh as opposed to diffusion that used a triangular mesh from FLOOPS. Hence, after every time step, the level set values that represented the α -c interface were interpolated onto the FLOOPS grid for different diffusion in amorphous and crystalline Si. Also, the dopant profile from the FLOOPS grid was interpolated onto the Level set mesh to take into account dopant effect on regrowth velocity.

6.4 1D SPER and Diffusion

1D SPER represents regrowth of a planar α -c interface. Simulations were done to confirm the results of one of the prior experiments done by Jacques *et al.*^{30,31,82}. The experiment was done on (001) bulk Si wafer to compute the diffusivity of Boron in amorphous Si. The implant

conditions were Si^+ at 70 keV energy and $1 \times 10^{15} \text{ cm}^{-2}$ dose that formed an amorphous layer of 150 nm. Then, B^+ was implanted at 500 eV, $1 \times 10^{15} \text{ cm}^{-2}$ to get a very shallow boron profile (completely contained within the amorphous layer) as shown in Figure 6-5. A low temperature of 550°C for 30 mins was subsequently done to completely recrystallize the amorphous layer. The solid-solubility of Boron at this annealing temperature was found to be $2.3 \times 10^{20} \text{ atoms/cm}^3$ (any Boron concentration above this, did not diffuse). Boron diffusivity was found to be concentration dependent with $D_B = 3 \times 10^{-17} + 3 \times 10^{-37} \times C_B \text{ cm}^2/\text{s}$ in amorphous Si. Boron diffusion in crystalline Si was found to be negligible. The above given parameters were used to simulate diffusion along with SPER with a rate of 325 nm/h (determined by the temperature of regrowth, using equation 4-2). Simulated profile is shown along with the measured SIMS profile of Boron after annealing in Figure 6-5 and they seem to match up well. However, it was observed that the interplay between diffusion and SPER was not a lot because the Boron had mostly diffused by the time the α -c interface reached the Boron. Once, the interface reached the Boron profile, it regrew very quickly and no significant diffusion was observed during that time.

6.5 2D SPER and Diffusion

SPER, in the most general sense is a three-dimensional (3D) process but in case of one of the dimensions of the structure being very long, it effectively can be treated as a 2D process. The long dimension in our study corresponds to the dimension into the page in all of the figures (similar to Chapters 4 and 5). Simulations were done for the as-implanted profile of Boron from section 6.4 and a patterned amorphous region with amorphous depth of 150 nm (same as section 6.4) and width of 300 nm as shown in Figure 6-6 (b). It was observed that the regrowth for the same amorphous depth as planar case did not complete in 30 mins. This is attributed to the formation of fronts other than (001) which have slower regrowth velocities (as mentioned in

Chapter 4). The simulated regrowth fronts upto $t = 30$ mins. are shown in Figure 6-6 (b). The time for complete regrowth was found to be 1 h. from simulations.

Figure 6-6 (a) shows the as-implanted profile and annealed profile of Boron after 30 mins. for planar regrowth from Figure 6-5. In addition to those profiles, simulated profiles for Boron after annealing for 1 h. (that was required for complete recrystallization of patterned amorphous region) are shown. The two simulated profiles have been taken from different cutlines in the patterned region (green and red colored cutlines from the center and edge of the pattern respectively have their corresponding colored profile in 6-6 (a)). The simulated dopant profile at the center of the pattern ($t = 1$ h) matches well with the annealed SIMS profile ($t = 30$ mins). The reason being that the center of the pattern regrew almost fully after 30 mins. as shown in Figure 6-6 (b) and there was no Boron diffusion after that (since Boron diffusion in c-Si is comparatively negligible). On the other hand, the regrowth at the corners was incomplete at $t = 30$ mins. as shown in Figure 6-6 (b). Hence, the Boron was in the amorphous Si for more time and diffused further after $t = 30$ mins. as is evident in simulated profile in Figure 6-6 (a). Thus, the final Boron profile was found to be non-uniform in the patterned region. From device perspective, this result has a lot of significance as the non-uniform doping profile could lead to more leakage between source/drain regions.

6.6 Summary

In summary, a novel experiment was done to see the effect of p-type and n-type dopants on regrowth. It was concluded that dopants enhance the regrowth rate of Si isotropically. Furthermore, they were not found to affect the regrowth shapes and hence the mask-edge defects. The Level set model was expanded to incorporate the dopant dependent velocity enhancement factor. Furthermore, diffusion and SPER processes were linked in the FLOOPS simulator. This

allowed for the simultaneous simulation of the two processes that helped in simulating accurate dopant profiles.

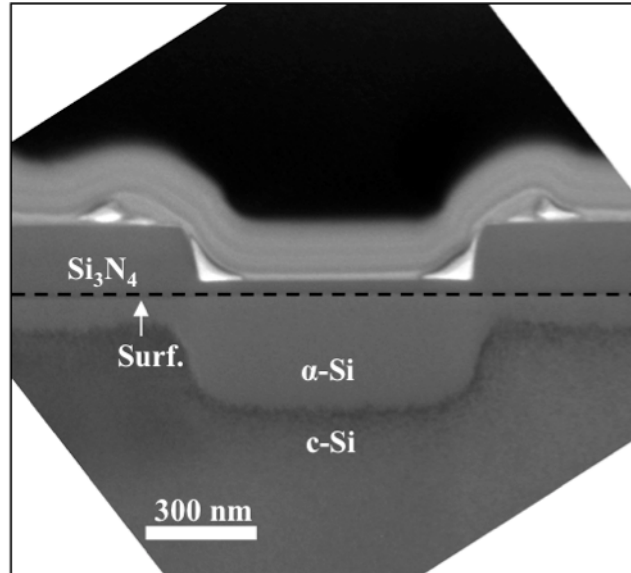


Figure 6-1. As-implanted α -c interface of Si for semi-insulating, n-type and p-type samples. Si_3N_4 mask patterned to get a patterned α -c interface.

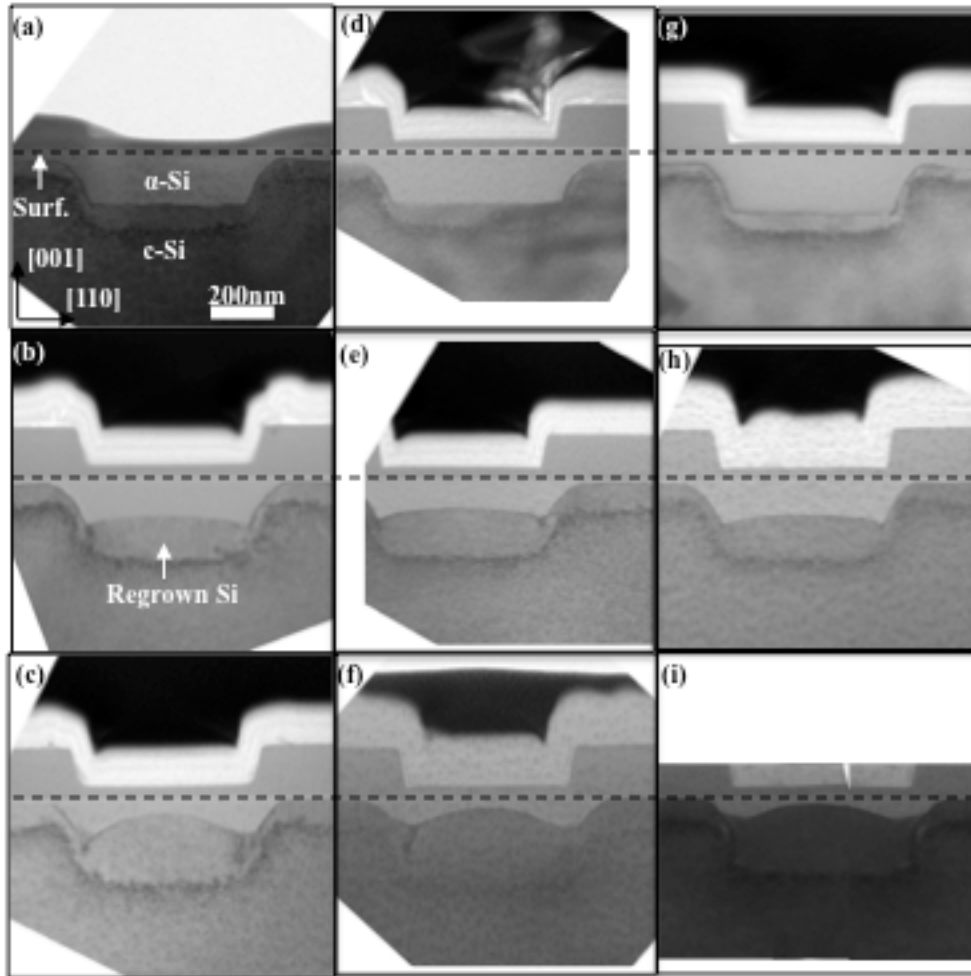


Figure 6-2. The observed 2D SPER process at $T=500\text{ }^{\circ}\text{C}$ with dopants: XTEM images of Semi-insulating (a-c), a) after annealing for 2h 30 min, b) after annealing for 5 h, and c) after annealing for 10 h; N-type As samples (d-f), d) after annealing for 1h 40min, e) after annealing for 3h 20min, and f) after annealing for 6 h; P-type B samples (g-i), g) after annealing for 40 min, h) after annealing for 1h 20min, and i) after annealing for 2h 40min.

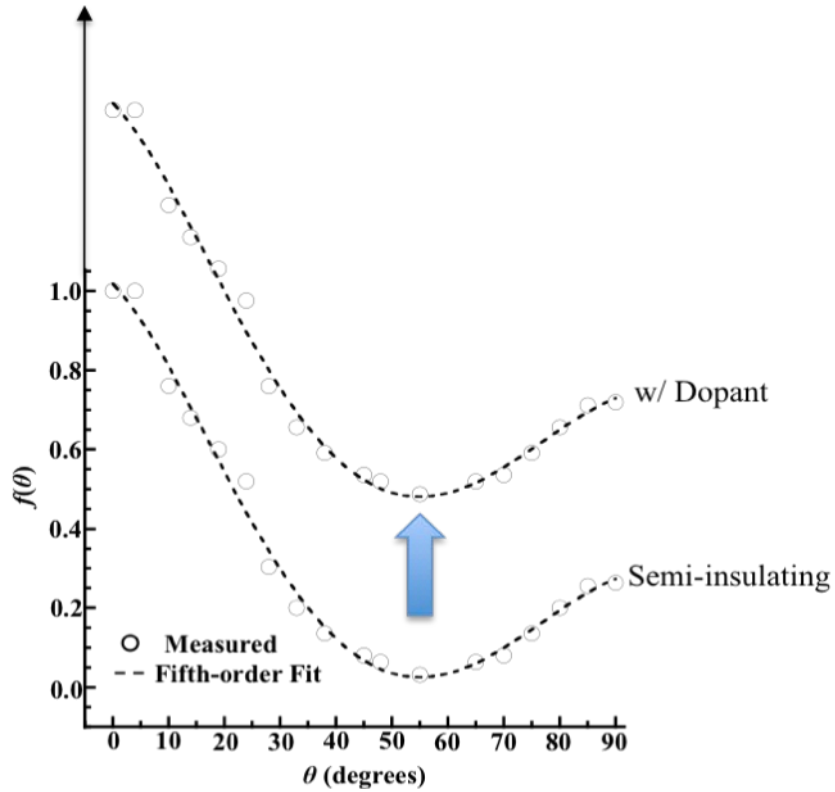


Figure 6-3. Figure shows the effect of dopants on Csepregi's ¹³ SPER data. Experimental results suggest shifting up of the data due to the isotropic SPER dopant enhanced velocity.

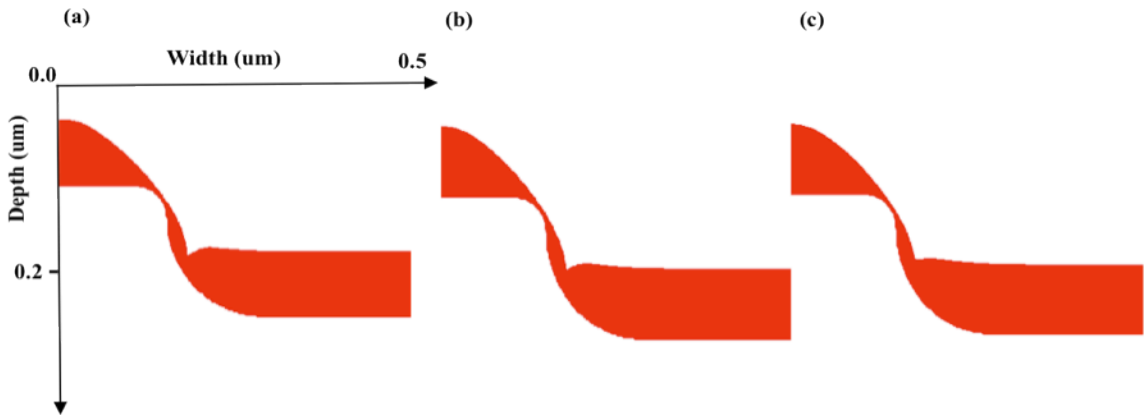


Figure 6-4. Level set simulations showing the effect of the curvature parameter "A" on the shape of regrowth for $t=5$ h. and $T=500$ °C. a) $A = 4.0 \times 10^{-7}$ cm (same as $A = 2.0 \times 10^{-7}$ cm), b) $A = 6.0 \times 10^{-7}$ cm shows less pinching of the concave [111] corner, c) $A = 8.0 \times 10^{-7}$ cm shows no pinching implying no mask edge defect formation.

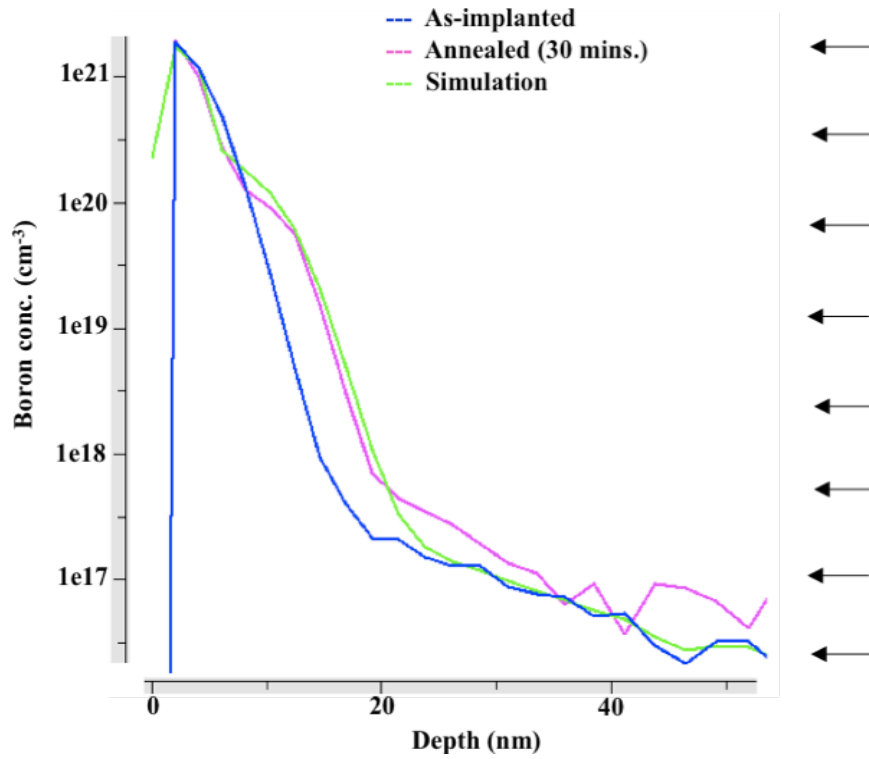


Figure 6-5. 1D diffusion of Boron during SPER. The figure shows the SIMS profile of Boron as-implanted and after annealing at $T=550^{\circ}\text{C}$ for $t=30\text{mins.}$ ^{30,82}. Simulation of the diffusion and SPER in FLOOPS is shown to match the SIMS profile.

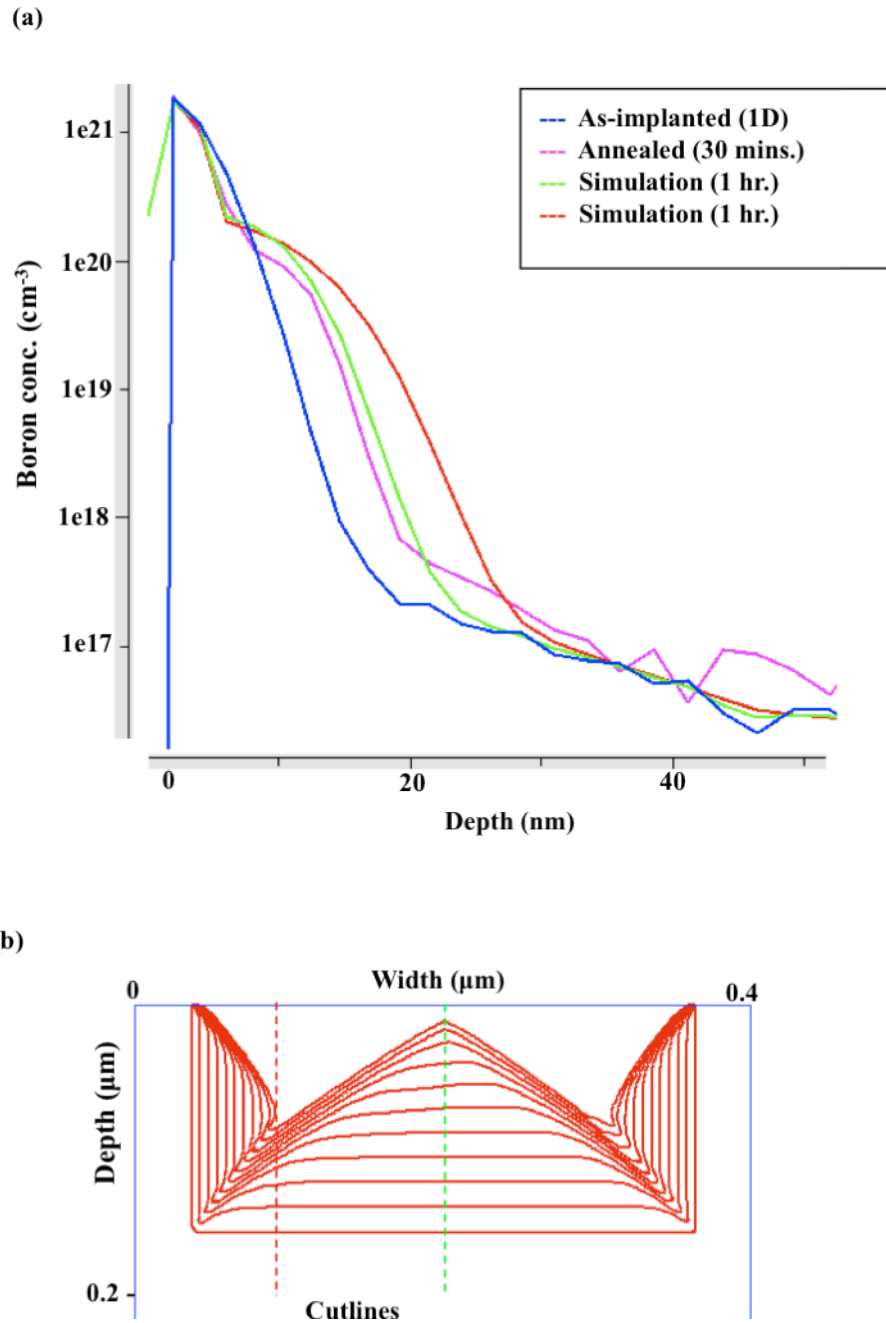


Figure 6-6. Figure shows the effect of 2D SPER on dopant profile. (a) shows the SIMS profile of Boron as-implanted and after annealing at $T = 550^{\circ}\text{C}$ for $t=30\text{mins}$.^{30,82} (same as figure 6-5). The simulation profiles show the profile of Boron after complete recrystallization of 2D amorphous trench shown in (b). The cutlines are taken at center and side of the trench. (b) shows the simulated SPER process ($T = 550^{\circ}\text{C}$) for a rectilinear amorphous region. The contours represent α -c interface at different times during regrowth.

CHAPTER 7 STRESS EFFECT ON SOLID PHASE EPITAXIAL REGROWTH OF SILICON

7.1 Introduction

Stress has known to play a major role in the SPER process^{33,34,37,41,49,53}. As explained in Chapter 2, externally applied out of plane compression and hydrostatic compression increase the planar SPER rate exponentially^{36,41}. This was attributed to the negative activation volume associated with conversion of α -Si into c-Si⁴¹. The converse was found to be true for tension. However, Rudawski *et al.*^{21,37,38,53} showed that the theory could not be extended to external in-plane stress. No increase in planar SPER rate was observed for uniaxial in-plane tension and the decrease in the planar SPER saturated at ~ 0.5 GPa. The results were explained by the nucleation and migration phenomena that control SPER⁵³. Nucleation was suggested to be the rate-limiting step. In-plane stress on the other hand affects the migration phenomena thus not affecting the SPER rate strongly. However, no model exists for patterned SPER in presence of in-plane stress. This Chapter explores the effect of uniaxial in-plane stress on patterned SPER. Experiments were done with in-plane uniaxial stresses upto ~ 1.5 GPa and their effect on SPER were studied.

Interface roughening (α -c Si) is another aspect of SPER that results from the application of in-plane compression during SPER^{34,49,51,57}. In-plane compression increases the interfacial roughening while no-stress or tensile stress reduces the roughness (details in Chapter 2). However, no models have been proposed to explain this phenomenon. Using level set methods approach and the curvature factor; this chapter aims to give possible explanations for interfacial roughening. This chapter also analyzes the physical reasons for the presence of curvature factor. Its relation to nucleation and migration processes is explained. The effect of stress on the curvature factor and encapsulation of stress in the curvature factor for patterned SPER is shown.

7.2 Interfacial Roughening During SPER

Section 2.2.2 showed the effect of uniaxial in-plane stress on the SPER of small amplitude sinusoidal shaped α -c Si interface. External compression tends to increase the amplitude of the shape while no-stress or tension tends to flatten it out. An experiment was done to confirm the experiments done by Barvosa-Carter *et al.*^{34,49} and also to see the effect of higher stresses on the regrowth of sinusoidal shaped α -c Si interface. Figure 7-1 shows the SPER under compression uniaxial in-plane stress applied using the novel bending apparatus as mentioned in section 3.1.3. Figure 7-1(a) shows the cartoon of as-implanted interface created by implanting Si⁺ at 20, 60, and 160 keV with doses of 1×10^{15} , 1×10^{15} , and 3×10^{15} cm⁻² to generate an undulating α -Si layer ~270 nm deep and in the shape of a sinewave with amplitude ~15 nm and wavelength ~500 nm. Figure 7-1(b) shows the SPER after 4h. at 525 °C under 250 MPa compression and Figure 7-1(c) shows SPER after 4h. at 525 °C under 500 MPa compression.

Figure 7-1(b) expectedly shows increase the interface shape amplitude under compression similar to prior work^{34,51}. However, Figure 7-1(c) shows interface roughening as well. Prior work did not show roughening at 500MPa though⁵¹. It is possible that the different techniques of applying and measuring the stress in the two experiments led to the error. Still, it's clear that stresses beyond a certain value (close to 500MPa) would start causing interfacial roughening.

Stress simulations were done using FLOOPS for calculating the stress on the sinewave interface between amorphous and crystalline Si. The amorphous Si was assumed to have a young's modulus half that of crystalline Si⁸⁴. Both materials were considered elastic for the simulations. The initial displacement of the wafer strip computed from the experiments was fed to the stress simulations. The stress simulation results showed the stress contours along the sinewave interface, implying no apparent difference in stress between peaks and valleys. Thus,

prior explanations^{34,49} of the sinewave amplitude getting affected due to unequal stresses in peaks and valleys cannot be substantiated. Moreover, the fact that even under no external stress, the amplitude of the interface decreases implies that curvature factor is responsible for this effect. It is intuitive that curvature effect would help flatten out the sinewave and the absence of it would lead to the amplitude increasing (due to orientation dependent velocity).

Crystalline Si is known to be denser than amorphous Si by ~3%⁵². Thus, as the α -Si is consumed by c-Si during SPER, there should be a stress build-up. However, since the top surface of Si is free, it leads to a relaxation of most of the out of plane stress. The effect of any stress that might be present in plane of the α -c Si interface is taken into account in the orientation dependent velocity. The planar regrowth experiment of different substrate orientation by Csepregi¹³ by default includes all the internal stresses while computation of orientation dependent velocity.

SPER with the orientation dependent velocity is capable of creating the interface roughening in the absence of curvature effect. This was shown by Level Set simulations of sinewave with different curvature factors (Figure 7-2). Figure 7-2(a) shows SPER at 525 °C after 1h with the curvature factor A (defined in Chapter 5) equal to zero. It is noticeable that in absence of curvature effect, the interface roughens up. The roughening can be attributed to the non-smooth as-implanted α -c Si interface. The rougher the starting interface, higher the interface roughening during SPER. It also implies that a rougher interface requires lower in-plane compression stress to start causing the roughening.

Figure 7-2(b), (c), (d) show SPER at 525 °C after 1h with $A = 1.5e-7, 2e-7, 4e-7$ cm respectively. The regrowth in all these cases is more than the case with $A=0$ because of lack of roughening. Roughening creates many slow regrowing $\{111\}$ fronts, thus leading to a reduction

in overall SPER rate. Stronger curvature (higher A) shows faster flattening of the sinewave and is thus closer to tension case. The above simulations are a clear indication that external in-plane stress modulates the curvature factor and is thus responsible for interfacial roughening or smoothing of the α -c Si interface during SPER.

The role of starting interface on the regrowing shape was demonstrated by Rudawski *et al.*⁵³. SPER under in-plane uniaxial stress for a planar α -c Si interface showed much more roughening for a rough starting interface. Figure 7-3(b), (c), (d) show SPER under 0.5GPa, 1GPa and 1.5GPa compression respectively at 525 °C for 1.3h (with starting interface at 7-3(a)). Figure 7-3(e) shows pre-annealing under no-stress for 0.7h to planarize the interface (for the same starting interface at 7-3(a)). Figure 7-3(f) shows the following SPER under 1.5GPa compression at 525 °C for 1.3h. All the samples had As-implant to increase the planar SPER rate. It shows very less roughening that is also demonstrated by less defect density (since these defects form due to the roughening of the interface⁵³). Moreover, it is almost impossible to get a perfectly smooth interface and thus there will always be some interfacial roughening after SPER under compression. The Level Set simulations are capable of capturing these results with rougher starting interfaces becoming even rougher in absence of the smoothing curvature effect.

7.3 In-Plane Uniaxial Stress Experiments

After exploring the effect of stress on relatively planar interfaces, it needs to be seen how the stress affect SPER of patterned trench regions α -Si that are known to create mask-edge defects. For consistency with experiments in Chapters 5 and 6, the as-implanted interface was created under similar experimental conditions. Some differences exist however. Instead of the 500 μ m thick Si wafers, ultra-thin (001) Si wafers (50 μ m thick) with double side polishing and high resistivity (\sim 250 Ω -cm) were used. This helped very clean cleaves of the wafer strips for

bending. Consequently, the wafer bending produced stresses upto 1.5GPa (as explained in Chapter 3). Si_3N_4 that was used for masking in experiments from Chapters 4,5 and 6 was not used because the stress from the deposited Si_3N_4 would have affected the total stress applied on the samples. Thus, PMMA was used as the mask that consisted of lines $\sim 0.5\mu\text{m}$ wide for etching Si $\sim 150\text{nm}$ deep. The lines were aligned along $\langle 110 \rangle$ in-plane directions. DRIE was used to etch Si anisotropically. However, some variations were noticed between the samples and the etch depth varied between 110-140 nm. Also, due to significant undercutting during DRIE, the masked lines were reduced to $\sim 0.2\text{-}0.3\mu\text{m}$ (Figure 7-4 (a) “surface”). It did not have any effect on the outcome of the experiment since similar results were observed for some test cases with wider lines ($\sim 1\mu\text{m}$). Subsequently, all the samples were Si^+ -implanted at 20, 60, and 150keV with doses of 1×10^{15} , 1×10^{15} , and $3 \times 10^{15} \text{ cm}^{-2}$ to generate an undulating α -Si layer of $\sim 110 \text{ nm}$ amplitude and $\sim 270\text{nm}$ depth from the surface. The as-implanted image is shown in Figure 7-4(a).

Some samples were allowed to regrow under no external stress conditions. They were annealed at $525 \text{ }^\circ\text{C}$ in N_2 ambient for 2h and 4h (Figures 7-4(b), (c) respectively). The SPER happens without the formation of mask-edge defect. This confirms the results from Chapter 5 where it was shown that the formation of defects was controlled not only the amplitude of α -Si undulation but also by the curvature of the as-implanted α -c interface (Figure 5-6). In the presented case, the corner is not as sharply curved when compared to experiments in Chapter 5 (Figure 5-3). Thus, SPER under no external stress does not result in formation of mask-edge defects. The SPER rate was found to be $\sim 100 \text{ nm/h}$ that is in conformity with previous works²⁷.

In-plane uniaxial stress was applied to the rest of the samples. Figure 7-5 (a), (b), (c) and (d) show partial SPER at $525 \text{ }^\circ\text{C}$ in N_2 ambient for 4h. under compression of 250 MPa, 500 MPa,

1.0 GPa and 1.5 GPa respectively. The planar part of the structure grew slower than the no-stress case. This was observed previously^{21,37,38} where the planar regrowth velocity reduces upto half under in-plane compression. Most noticeable is the formation of mask-edge defects in all the four compression cases. This can be attributed to a lower curvature effect, i.e. lower enhancement of the concave corner velocity and hence more pinching of the corner. For cases with higher compression (1GPa and 1.5GPa), interface roughening of the planar part was observed. The interface roughening also leads to formation of more defects as was observed by Rudawski *et al.*⁵³ in the planar regrowth studies.

In-plane uniaxial tension cases are shown in Figures 7-5 (e), (f), (g), (h). The anneals for tension cases were done for 2 h. at 525 °C so as to catch the regrowth at a similar position as the compression case anneals (tension SPER is twice as fast as compression). All the cases of tension look exactly the same and are no different from the no-stress case shown in Figure 7-4(b). This is similar to planar SPER where tension made no difference to the SPER rate⁵³. As shown in Chapter 2, tension has been known to help get rid of mask-edge defects^{19,22}. However, if no mask-edge defects exist in the no-stress case, then tension does not affect the SPER. This fact has been noticed in sinewave experiments of section 7.2 as well. The tension and compression cases shown in Figure 7-5 have some difference in the Si surface used for creating undulation of α -Si. The compression case seems to have a narrower line width (by ~100 nm) and a deeper etch (by ~40nm). However, the results don't get too strongly affected by it. This is further confirmed in the simulations as shown in section 7.4.

7.4 Simulation and Curvature Effect

Level set simulations were done with varying the curvature factor A to simulate experiments shown in section 7.4. Prior simulations in Chapters 4, 5 and 6 had initialized the simulations using geometrical functions to match the as-implanted α -c interface. However, to get

a more accurate initial interface, actual cross-section transmission electron microscopy (XTEM) images were fed to MATLAB and discrete x,y coordinates of the as-implanted interface were extracted. These were used for initializing the level set simulations. One of the benefits of using the actual XTEM image for initialization is the slight roughness present on the initial interface, something that actually exists in the structure. The previous geometrical arguments used for simulations considered the planar interface to be very smooth and hence interface roughening after SPER was not visible.

Figures 7-6(a), (b) and (c) show the simulations of SPER for the compression case. The simulations include orientation dependent velocity, varying curvature parameter (A) and SPER velocity computed at 525°C (and $t=4\text{h}$) for planar compression case (i.e. half the no-stress velocity). Figure 7-6(a) represents the case with $A=1.5\text{e-}7$ cm. The planar regions of the as-implanted α -c interface (on either side of the triangular region) do not regrow smoothly. They include interface roughening after SPER. Apart from that the notch and the triangular front as observed in experiments with compression are clearly noticeable in the simulation. Thus, it resembles cases of higher compression (1GPa and 1.5GPa). Figure 7-6(b) represents the case with $A=2\text{e-}7$ cm which resembles the lower compression cases (250MPa and 500MPa). The planar regions regrow do smooth out. The triangular region is visible with the notch on either side predicting the formation of defects. Figure 7-6(c) represents the case with $A=4\text{e-}7$ cm and clearly is not matching with any of the compression cases.

Figures 7-6(d), (e), (f) show simulations of SPER for the tension case (and also the no-stress case since it is same as tension) with SPER velocity computed at 525°C (and $t=2\text{h}$) for planar tension case (same as no-stress velocity). It is very evident that Figure 7-6(d) that

represents $A=2e-7$ cm does not match up with the observed results. Figures 7-6(e) and (f) that represent $A=4e-7$ cm and $6e-7$ cm are much closer to the XTEMs shown in Figures 7-5(e-h).

The above mentioned curvature factor of $A=4e-7$ cm and $6e-7$ cm fitting the observed results seems to be different than Chapters 5 and 6 where $A=2e-7$ cm was used. However, simulations done with $A=4e-7$ cm and $6e-7$ cm seem to fit the results in Chapters 5 and 6 as well (not presented). Thus, there seems to be an error window for the curvature factor. The factor can be between $4e-7$ cm and $6e-7$ cm. For cases where defects form (in no external stress case), even $A=2e-7$ cm would work. However, since that does not fit the cases where no defects form, implies A is between $4e-7$ cm and $6e-7$ cm. For compression cases though this value goes down to $A=2e-7$ cm for lower stress and $A=1.5e-7$ cm for higher stresses. For structures where no-stress case does not lead to defect formation, tension does not affect regrowth shapes and increasing A beyond $6e-7$ cm does not alter simulation results. Though for cases where defects do form for no-stress case, increasing A beyond $6e-7$ cm correctly predicts no defect formation as was observed in prior experiments^{19,22}.

7.4 Physical Explanation of Curvature Effect

Since the curvature effect plays a vital role in the SPER process, it is important to understand what physical mechanism is governing it. The information about the curvature factor that has been gathered from experiments and simulations in the presented work are the following:

1. Curvature factor plays a big role in determining the shape of patterned SPER. Curvature effect is also necessary for planarization of rough as-implanted interface (for no-external stress case).
2. Curvature effect is independent of the temperature dependence (similar to orientation effect).

3. Electronic processes that govern the enhancement of SPER due to dopants, do not affect curvature parameter.
4. Stress increases the curvature parameter for in-plane external tension and decreases the curvature parameter for in-plane external compression.

Apart from the above information, prior results confirm the two results as follows,

1. I-V pair (or bond defect) is believed to be responsible for amorphization and recrystallization⁶⁰ from Molecular Dynamics simulations. The theory of I-V pair recombination suggests a higher activation for recombination of I-V pairs (and thus for recrystallization) when one pair is surrounded by more of its kind. This is a clear proof of a curvature like effect playing an important role in SPER.
2. SPER has been analytically modeled as the combination of nucleation and migration time constants^{37,38,53}. For planar SPER, nucleation time constant is believed to be the rate-limiting step. Migration time-constant is affected by in-plane stress. In-plane tension reduces the time for migration but does not affect the process since nucleation is the rate limiter. However, in-plane compression increases the migration time-constant and reduces the overall SPER rate.

Curvature factor (as shown in section 7.3) is affected by stress as well.

In light of all the above observations, curvature factor should be a part of nucleation mechanism. Simulations suggest that the impact of curvature is higher for planes like $\{111\}$ and $\{011\}$ as compared to $\{001\}$ since the latter has a higher SPER rate. This is also confirmed by the prior theory⁸⁵ where the nucleation mechanism is most important for the fronts other than $\{001\}$. This was attributed to the fact that the formation of the six-member ring requires nucleation of three atoms for $\{111\}$ plane and two atoms for $\{011\}$ plane (and no nucleation of

{001} plane since it requires just one atom). The presence of concave curvature would help in the nucleation of these atoms. This supports the use of curvature factor in no external stress simulations (in Chapters 5,6 and 7).

Since, curvature is temperature independent, it should be a part of prefactor of the nucleation term just like the orientation dependent velocity factor is¹³. The curvature term should also play a role in the migration of the ledges since a concave curvature would provide with built-in ledges and migration would be faster. However, an analytical expression for the curvature factor in nucleation and migration processes has not been worked out.

7.5 Summary

In summary, the strong effect of curvature on smoothing out the interfacial roughening during SPER was shown. For in-plane compression, the reduction of curvature factor was shown to cause more roughening. Experiments were done with trench amorphous regions (~110-150nm perturbed) to explore the effect of large in-plane uniaxial stress on SPER. No defects were observed after SPER of no-stress case. This confirmed the simulation predictions from Chapter 5 where it was mentioned that initial curvature of the interface was as much responsible for creation of mask-edge defects as the trench depth. In-plane uniaxial tension upto 1.5GPa did not affect the SPER in any way (similar to planar case). However, in-plane uniaxial compression led to the formation of mask-edge defects. Higher compression (above 1GPa) caused the roughening of the planar regions of the α -c interface. Level set simulations predicted the observed results accurately by modulating the curvature factor (A) for different stresses. Tension was found to increase the curvature factor and compression reduced it. Thus, encapsulation of the stress effect in the curvature effect was shown. Physical interpretation of the curvature effect as part of nucleation and migration processes was proposed.

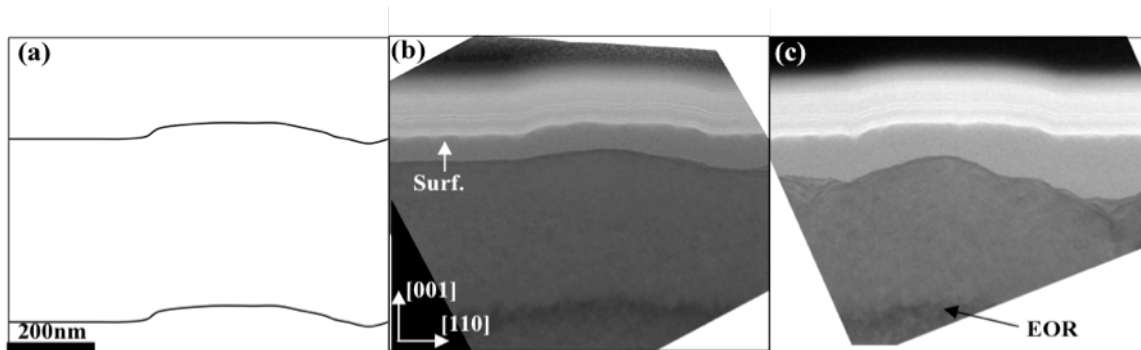


Figure 7-1. XTEM images of SPER under in-plane uniaxial compression : (a) shows cartoon of as-implanted α -c interface with perturbation of $\sim 15\text{nm}$. (b) shows SPER at $525\text{ }^{\circ}\text{C}$ for 4h. under compression with $\sigma_{11} = -250\text{MPa}$. (c) shows SPER at $525\text{ }^{\circ}\text{C}$ for 4h. under compression with $\sigma_{11} = -500\text{MPa}$.

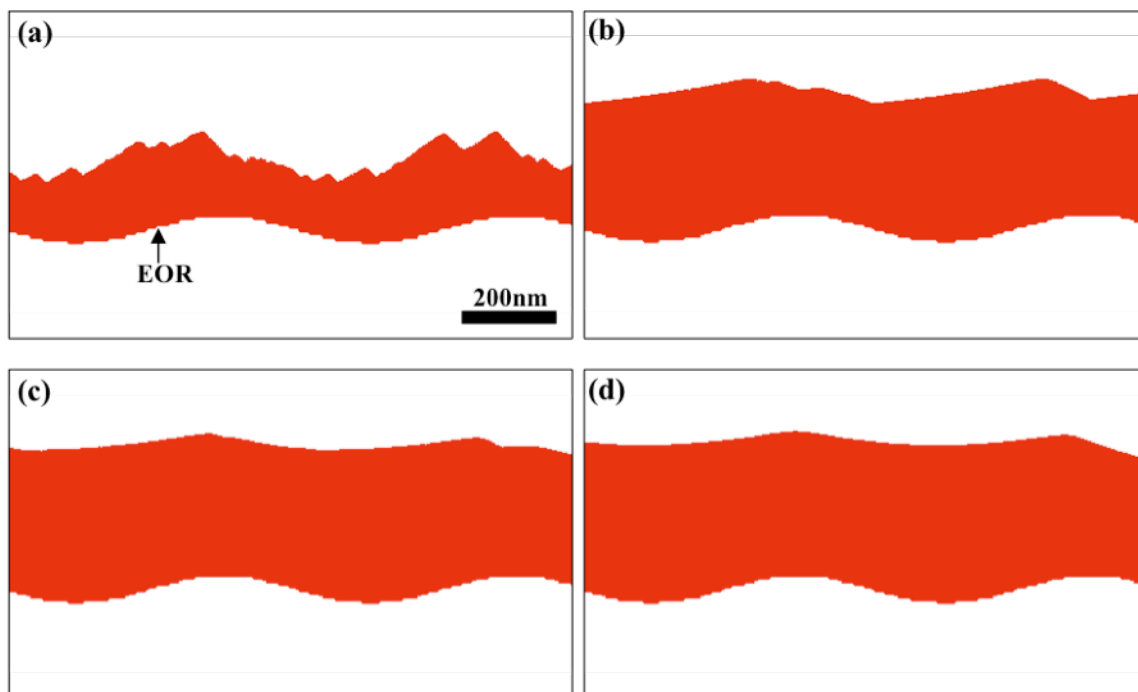


Figure 7-2. Level set simulations of SPER with varying curvature factor A . (a), (b), (c), (d) represent SPER after 1h. at $525\text{ }^{\circ}\text{C}$ with values of $A = 0, 1.5\text{e-}7, 2\text{e-}7, 4\text{e-}7\text{cm}$ respectively.

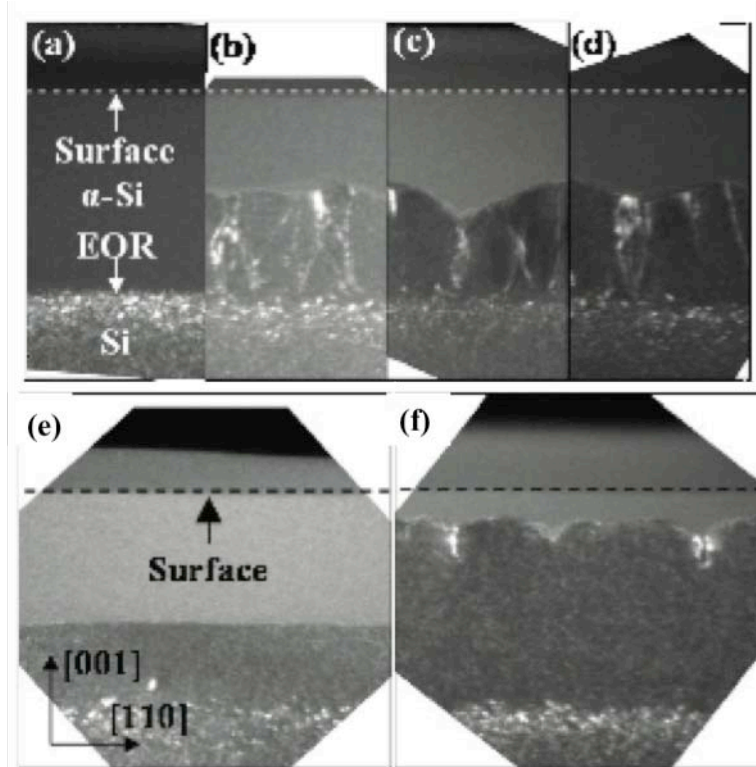


Figure 7-3. Weak beam dark field (WBDF)-XTEM images of the stress-influenced SPER process in As-doped specimens⁵³: a) WBDF-XTEM image of an as-implanted As-doped specimen. WBDF-XTEM images of As-doped specimens annealed at $T = 525$ °C for 1.3 h with $\sigma_{11} =$ b) -0.5, c) -1.0, d) -1.5GPa respectively. (e) WBDF-XTEM image after pre-annealing under no stress for $t=0.7$ h at $T = 525$ °C. (f) WBDF-XTEM image after annealing at $T = 525$ °C for 1.3 h with $\sigma_{11} = -1.5$ GPa (done after pre-annealing)⁵³. Reprinted with permission from Rudawski, PhD. Thesis, University of Florida. Copyright © 2008, Nicholas G. Rudawski.

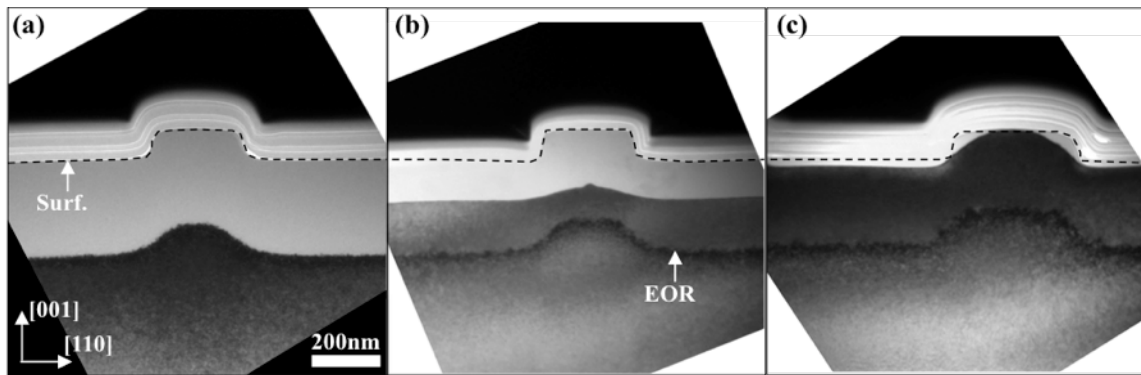


Figure 7-4. XTEM images of patterned SPER under no external stress: (a) shows the as-implanted α -c interface with perturbation of ~ 110 nm. (b), (c) show SPER at 525°C for 2h., 4h. respectively.

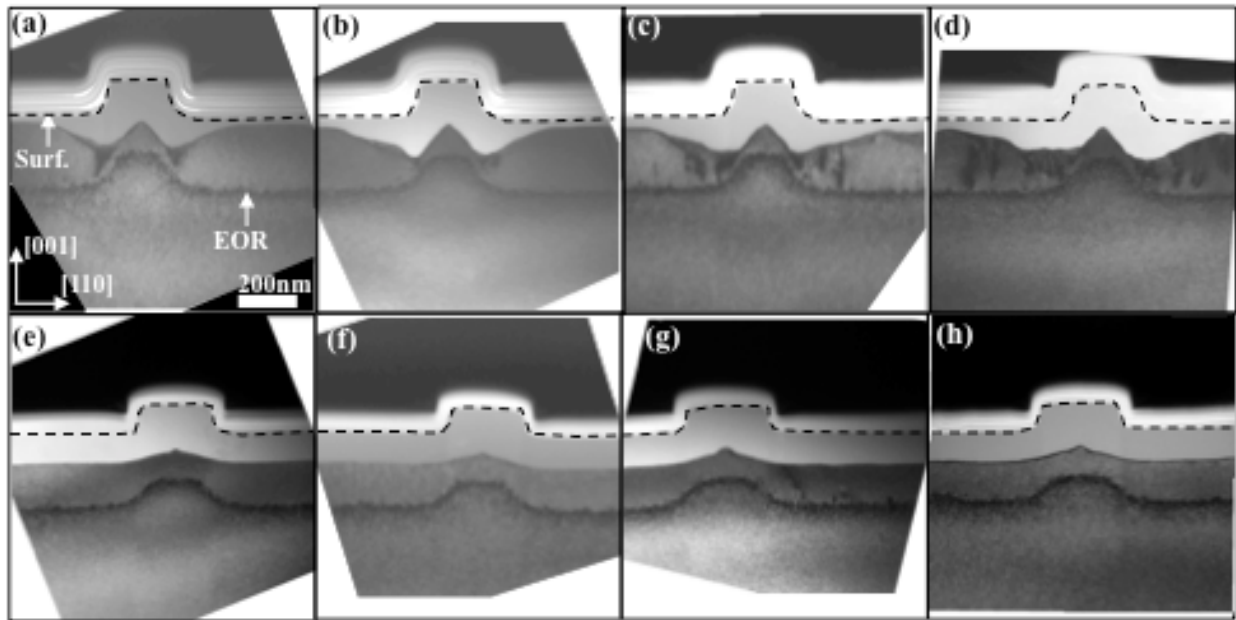


Figure 7-5. XTEM images of patterned SPER under in-plane uniaxial stresses: (a), (b), (c), (d) show SPER at $T = 525^{\circ}\text{C}$ for 4h. under compression with $\sigma_{11} = -0.25, -0.5, -1.0, -1.5$ GPa respectively. (e), (f), (g), (h) show SPER at $T = 525^{\circ}\text{C}$ for 2h. under tension with $\sigma_{11} = 0.25, 0.5, 1.0, 1.5$ GPa respectively. End of range (EOR) shows the position of as-implanted interface. Surface (Surf.) of the patterned Si is shown as well.

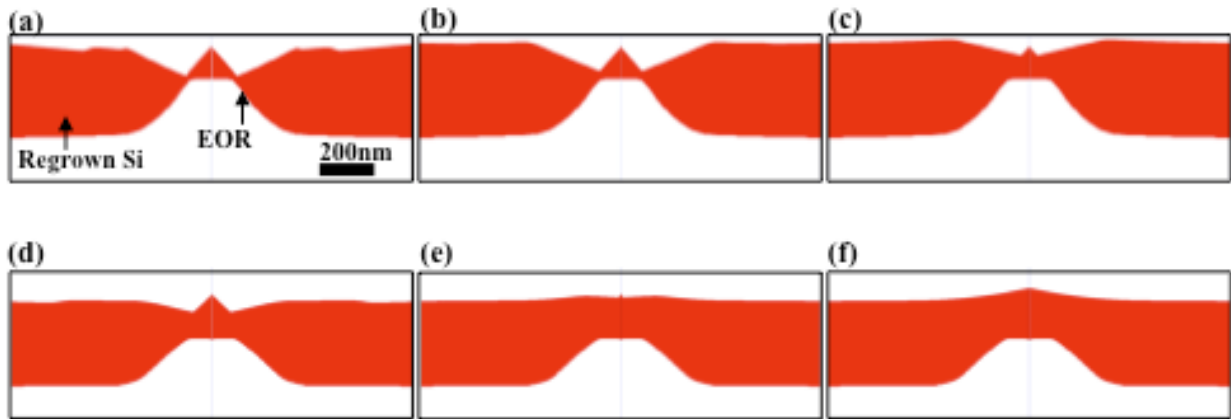


Figure 7-6. Level set simulations of SPER for matching the observations shown in Figure 7-5 by varying curvature factor A . (a), (b), (c) represent SPER after 4h. at 525°C with values of $A = 1.5\text{e-}7, 2\text{e-}7, 4\text{e-}7\text{cm}$ respectively. (d), (e), (f) represent SPER after 2h. at 525°C with values of $A = 2\text{e-}7, 4\text{e-}7, 6\text{e-}7\text{cm}$ respectively.

CHAPTER 8 SUMMARY AND FUTURE WORK

8.1 Overview of Results

The presented work has given a better understanding of the Solid Phase Epitaxial Regrowth (SPER) process for patterned amorphous regions in more detail than has been ever done before. Different aspects of SPER for patterned regions were studied that included the shape of initial α -c interface, dopant effect, in-plane stress. Simulations based on a complex mathematical technique called Level set methods were done to confirm and predict experimental results.

Level set model was initially implemented using regrowth velocity that included thermal activation²⁷ and substrate orientation dependent velocity (by encapsulating the orientation dependence data in a curve fitted factor, $f(\theta)$). However, it failed to accurately match the simulations to the observed cross sectional transmission electron microscopy (XTEM) images. The simulations showed some differences with the TEM images near the $\langle 111 \rangle$ corners and a variation in the velocity near the corners was insufficient to match up with observed results. Thus, a curvature factor was introduced that increased the velocity of concave corners and decreased for the convex. Modifying the orientation dependent regrowth model to be linearly dependent on local interface curvature did accurately account for regrowth evolution⁵⁶. The same curvature dependence was successful in predicting the regrowth evolution in structures with or without surface pinning of the interface.

The apparent linear dependence of regrowth kinetics on interface curvature was experimentally found to be temperature insensitive. The regrowth model was then used to predict the regrowth for different starting α -c interfaces. This included varying the initial curvature of the α -c interfaces and varying the width-to-depth (W/D) ratio of the amorphous region. The

simulations gave an insight about the evolution of regrowth shapes and how different starting α -c interfaces could be used for the betterment of device fabrication and performance. Simulations predicted lesser mask-edge defect formation if the initial curvature of the α -c interface was low (larger radius of curvature). This was experimentally confirmed in Chapter 7 when even a $\sim 110\text{nm}$ perturbed α -c interface did not create mask-edge defects (in absence of external stress) after SPER.

Regarding dopant effect on SPER, a novel experiment was done to see the effect of p-type and n-type dopants on patterned regrowth. Using low resistivity wafers (both p and n-type), SPER of patterned amorphous region showed that dopants enhance the regrowth rate of Si isotropically. Furthermore, they were not found to affect the regrowth shapes and hence the mask-edge defects. The Level set model was expanded to incorporate the dopant dependent velocity enhancement factor. Since, dopant related enhancement of SPER is known to be an electronic process, the experiment proved (within an error window) the dissociation of curvature factor from the electronic effect. Also, the diffusion capabilities of FLOOPS (Florida Object Oriented Process Simulator) simulator were used in conjunction with level set simulations to predict 2D dopant profiles during and after SPER.

Planar SPER has been known to create interface roughness in the presence of external in-plane compressive stress. Also, SPER of a small amplitude sinewave shaped α -c interface is known to increase in amplitude in presence of in-plane compression. This work attempted to see both interface roughness and amplitude increase in presence of in-plane compression on SPER of a sinewave shaped interface. Level set simulations and stress simulations were done together to draw inferences on the observed results. Prior theory related the increase amplitude due to in-plane compression to different stresses on peaks and valleys^{34,49}. However, stress simulations

done in this work showed no difference in stresses on peaks and valleys. Level set simulations emphasized the need for curvature factor to smooth out interface perturbation. Lack of curvature factor caused the orientation dependent velocity to cause amplitude increase and also interface roughening.

For the first time, experiments were done with patterned amorphous regions (110-150nm perturbation) to explore the effect of large ($\sigma_{11} = \pm 1.5\text{GPa}$) in-plane uniaxial stresses on SPER. No defects were observed after SPER of no-stress case. In-plane uniaxial tension upto 1.5GPa did not affect the SPER in any way (similar to planar case). However, in-plane uniaxial compression led to the formation of mask-edge defects. Higher compression ($|\sigma_{11}| \geq 1\text{GPa}$) caused the roughening of the planar regions of the α -c interface. Level set simulations predicted the observed results accurately by modulating the curvature factor (A) for different stresses. Tension was found to increase the curvature factor and compression reduced it. Thus, encapsulation of the stress effect in the curvature effect was shown. Physical interpretation of the curvature effect as part of nucleation and migration processes was proposed.

8.2 Future Work

The role of stress on SPER is complex. The effects of out-of-plane stress and in-plane stress have been known to be vastly different^{21,41}. However, the role of both the in-plane stress directions is believed to be same on SPER. This has been shown to be true of planar SPER with both the in-plane directions being $\langle 011 \rangle$. Some recent experiments (unpublished) have studied the effect of in-plane stress in direction parallel to the patterned lines, i.e. into the page of all the figures (as opposed to perpendicular to the lines shown in Chapter 7).

Figure 8-1 shows SPER at 525 °C for 4h. under uniaxial in-plane compression parallel to lines ($\sigma_{22} \approx -300\text{MPa}$). The end of range (EOR) in the figures show the as-implanted α -c

interface. The line structure for patterning was repetitive and Figures 8-1(a), (b), (c) and (d) show different line structures as observed in cross-section transmission electron microscopy (XTEM). Different lines showing different SPER implies that over the width of the lines (into the page of the figure), the defects randomly form and they show up in some lines (since XTEM takes a sample slice of ~100nm in the width direction). It would be more conclusive to do plan view transmission electron microscopy (PTEM) to further confirm the presence of random defects over the width of the lines in the future.

Figure 8-1(a) shows no mask-edge defects that were observed due to in-plane compression in Figure 7-5(a) (with $\sigma_{11} = -250\text{MPa}$). Rudawski *et al.*^{21,53} showed that in-plane compression reduced the migration of the ledges in the direction of stress. This suggests that migration of ledges is affected in the width direction for the case presented in Figure 8-1. This would lead to roughening of the interface in that direction. From curvature factor perspective, the curvature in the width direction would control the defects in that direction. In the plane of the page, the curvature factor would not be influenced since the stress is in the perpendicular direction. However, more work needs to be done to confirm this theory by implementing 3-D Level set simulations.

SPER in Figure 8-1(a) was faster than what was observed in Figure 7-5(a) (for the same time-temperature anneal). Thus, to confirm that the compressive stress applied was not negligible, the same bend was applied perpendicular to the lines and the annealing was done for 4h. at 525 °C (as shown in Figure 8-2(a)). The formation of mask-edge defects and higher SPER of the planar regions showed that the stress was applied correctly; it was probably a temperature variation between the samples that led to faster regrowth in Figures 8-1 and 8-2. Bending of the samples for this experiment was done using a different quartz tray than the one used for

experiments in Chapter 7. Thus, there was a definite possibility of a variation in positioning of the samples for the two different trays. Figure 8-2(b) shows SPER for 2h. at 525 °C under uniaxial in-plane tension ($\sigma_{22} \approx 300\text{MPa}$) parallel to the lines (into the page of figures). Tension did not affect the regrowth when compared to no-stress case or when compared to tension in the direction perpendicular to the lines (not presented).

Regarding the mask-edge defects, it is still not clear as to what their effect is on relieving the stress on the α -c interface. The regrowth of the pinched corners after the formation of defects also needs to be explored more. Some experimental results²³ show that the regrowth at the corners after the defect formation becomes faster due to formation of planes with orientations other than $\langle 111 \rangle$. This observation led to Saenger *et al.*²³ proposing a nano-facet model for SPER. However, the nano-facet model is very simplistic and more work is required to quantitatively describe the SPER of corners after defect formation.

Chapter 6 dealt with issues of B diffusion during SPER and integrated the diffusion model with regrowth model to get a more accurate B profile after SPER. However, some dopants like As exhibit segregation at the α -c interface²⁷. The final profile of As after SPER is strongly affected by the segregation effect. Thus, segregation model needs to be added to the regrowth model to more accurately predict dopant profiles after SPER.

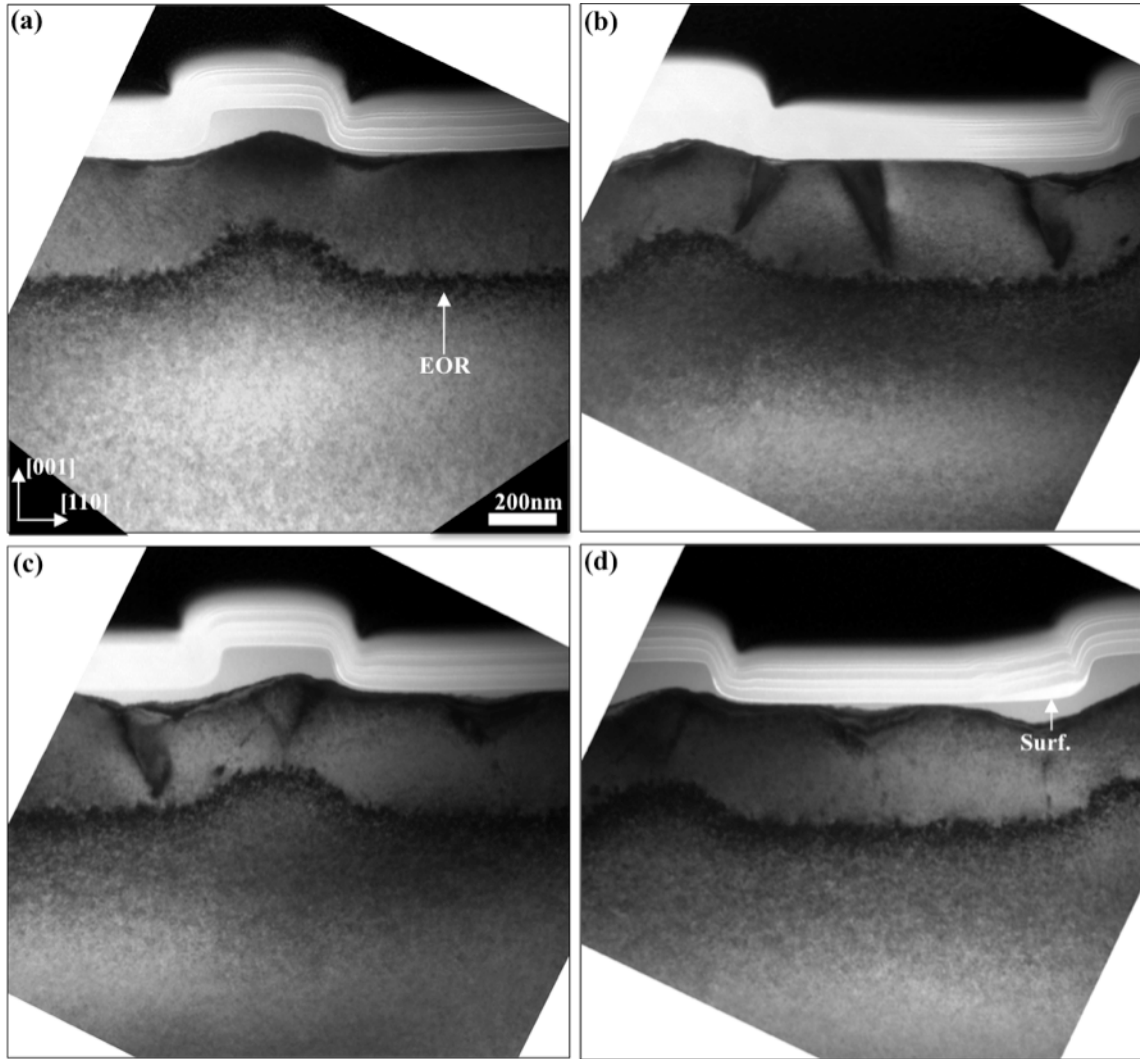


Figure 8-1. XTEM images of SPER at 525 °C for 4h. under uniaxial in-plane compression into the page of the figure (or parallel to lines $\sigma_{22} \approx -300\text{MPa}$). (a), (b), (c), (d) show variation of regrowth for different lines.

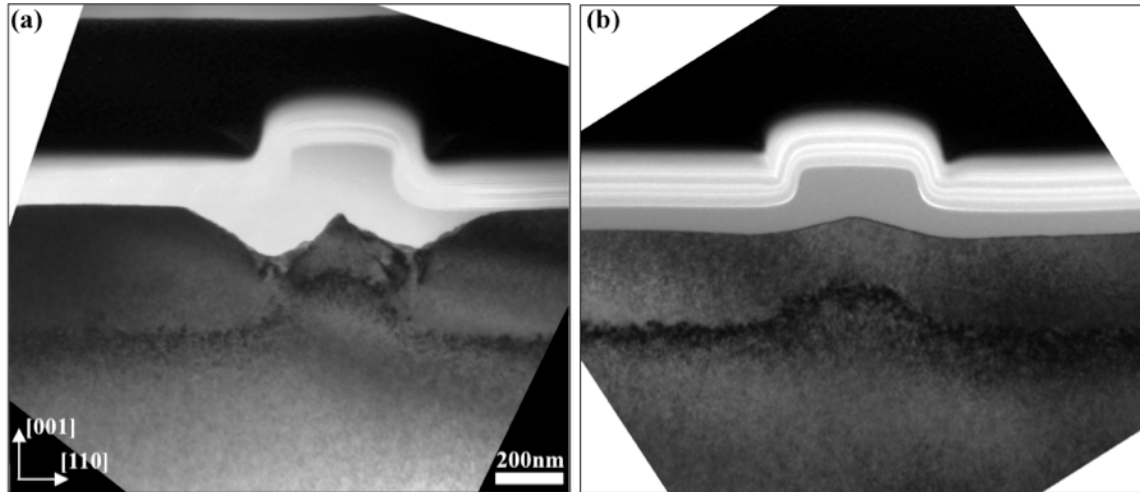


Figure 8-2. XTEM images of SPER under uniaxial in-plane stresses into the page of the figure (or parallel to lines $\sigma_{22} \approx \pm 300\text{MPa}$). (a) shows SPER under compression for 4h. at $525\text{ }^{\circ}\text{C}$, (b) shows SPER under tension for 2h. at $525\text{ }^{\circ}\text{C}$

LIST OF REFERENCES

- 1 G. E. Moore, *Electronics* **38**, 114-117 (1965).
- 2 D. M. Camm, J. C. Gelpey, T. Thrum, G. C. Stuart, and S. McCoy, *Jom* **58**, 32-34 (2006).
- 3 S. E. Thompson, M. Armstrong, C. Auth, S. Cea, R. Chau, G. Glass, T. Hoffman, J. Klaus, Z. Y. Ma, B. McIntyre, A. Murthy, B. Obradovic, L. Shifren, S. Sivakumar, S. Tyagi, T. Ghani, K. Mistry, M. Bohr, and Y. El-Mansy, *Ieee Electron Device Letters* **25**, 191-193 (2004).
- 4 S. Ito, H. Namba, T. Hirata, K. Ando, S. Koyama, N. Ikezawa, T. Suzuki, T. Saitoh, and T. Horiuchi, *Microelectronics Reliability* **42**, 201-209 (2002).
- 5 A. Al-Bayati, L. Washington, M. B. L. Xia, Z. Yuan, M. Kawaguchi, F. Nouri, and R. Arghavani, in *Semiconductor Fabtech; Vol. 26* (2005).
- 6 T. I. H. Nishi, T. Sakurai, T. Kaneda, T. Hisatsugu, and T. Furuya, *Journal of Applied Physics* **49**, 608-613 (1978).
- 7 M. T. Robinson and O. S. Oen, *Applied Physics Letters* **2**, 30-32 (1963).
- 8 A. Bousetta, J. A. Vandenberg, R. Valizadeh, D. G. Armour, and P. C. Zalm, *Nuclear Instruments & Methods in Physics Research Section B-Beam Interactions with Materials and Atoms* **55**, 565-568 (1991).
- 9 H. Nishi, T. Sakurai, and T. Furuya, *Journal of the Electrochemical Society* **125**, 461-466 (1978).
- 10 J. J. Hamilton, E. J. H. Collart, B. Colombeau, C. Jeynes, M. Bersani, D. Giubertoni, J. A. Sharp, N. E. B. Cowern, and K. J. Kirkby, *Nuclear Instruments & Methods in Physics Research Section B-Beam Interactions with Materials and Atoms* **237**, 107-112 (2005).
- 11 K. Ota, K. Sugihara, H. Sayama, T. Uchida, H. Oda, T. Eimori, H. Morimoto, and Y. Inoue, *IEDM Tech. Digest* **27** (2002).
- 12 P. Morin, C. Ortolland, E. Mastromatteo, C. Chaton, and F. Arnaud, *Materials Science and Engineering B-Solid State Materials for Advanced Technology* **135**, 215-219 (2006).
- 13 L. Csepregi, E. F. Kennedy, J. W. Mayer, and T. W. Sigmon, *Journal of Applied Physics* **49**, 3906-3911 (1978).
- 14 S. Morarka, N. G. Rudawski, and M. E. Law, *Journal of Vacuum Science & Technology B* **26**, 357-361 (2008).
- 15 K. L. Saenger, K. E. Fogel, J. A. Ott, D. K. Sadana, and H. Yin, *Journal of Applied Physics* **101**, 104908 (2007).
- 16 H. Cerva, *Defect and Diffusion Forum* **148**, 103-121 (1997).

- 17 H. Cerva and W. Bergholz, *Journal of the Electrochemical Society* **140**, 780-786 (1993).
- 18 H. Cerva and K. H. Kusters, *Journal of Applied Physics* **66**, 4723-4728 (1989).
- 19 C. Ross and K. S. Jones, *Mat. Res. Soc. Symp. Proc.* **810**, C10.4 (2004).
- 20 N. G. Rudawski, K. S. Jones, and R. G. Elliman, *Journal of Vacuum Science & Technology B* **26**, 435-438 (2008).
- 21 N. G. Rudawski, K. S. Jones, and R. Gwilliam, *Applied Physics Letters* **91**, 172103 (2007).
- 22 N. G. Rudawski, K. N. Siebein, and K. S. Jones, *Applied Physics Letters* **89**, 082107 (2006).
- 23 K. L. Saenger, J. P. de Souza, K. E. Fogel, J. A. Ott, C. Y. Sung, D. K. Sadana, and H. Yin, *Journal of Applied Physics* **101**, 024908 (2007).
- 24 Y. G. Shin, J. Y. Lee, M. H. Park, and H. K. Kang, *Japanese Journal of Applied Physics Part 1-Regular Papers Short Notes & Review Papers* **40**, 6192-6197 (2001).
- 25 Y. G. Shin, J. Y. Lee, M. H. Park, and H. K. Kang, *Journal of Crystal Growth* **233**, 673-680 (2001).
- 26 Y. G. Shin, J. Y. Lee, M. H. Park, and H. K. Kang, *Journal of Crystal Growth* **231**, 107-114 (2001).
- 27 G. A. Olson and J. A. Roth, *Materials Science Reports* **3**, 1-78 (1988).
- 28 B. C. Johnson and J. C. McCallum, *Physical Review B* **76**, 045216 (2007).
- 29 J. S. Williams and R. G. Elliman, *Physical Review Letters* **51**, 1069-1072 (1983).
- 30 J. M. Jacques, L. S. Robertson, K. S. Jones, M. E. Law, M. Rendon, and J. Bennett, *Applied Physics Letters* **82**, 3469-3471 (2003).
- 31 J. M. Jacques, PhD thesis Thesis, University of Florida, 2006.
- 32 M. E. Law, in *Florida Object Oriented Process Simulator* Release 2002 ed. (2002).
- 33 W. Barvosa-Carter and M. J. Aziz, *Applied Physics Letters* **79**, 356-358 (2001).
- 34 W. Barvosa-Carter, M. J. Aziz, L. J. Gray, and T. Kaplan, *Physical Review Letters* **81**, 1445-1448 (1998).
- 35 G. Q. Lu, E. Nygren, M. J. Aziz, D. Turnbull, and C. W. White, *Applied Physics Letters* **54**, 2583-2585 (1989).
- 36 E. Nygren, M. J. Aziz, D. Turnbull, J. M. Poate, D. C. Jacobson, and R. Hull, *Applied Physics Letters* **47**, 232-233 (1985).

- 37 N. G. Rudawski, K. S. Jones, and R. Gwilliam, *Materials Science & Engineering R-Reports* **61**, 40-58 (2008).
- 38 N. G. Rudawski, K. S. Jones, and R. Gwilliam, *Physical Review Letters* **100**, 165501 (2008).
- 39 N. G. Rudawski, K. S. Jones, and R. Gwilliam, *Journal of Materials Research* **24**, 305-309 (2009).
- 40 K. L. Saenger, K. E. Fogel, J. A. Ott, J. P. de Souza, and C. E. Murray, *Applied Physics Letters* **92**, 124103 (2008).
- 41 M. J. Aziz, P. C. Sabin, and G. Q. Lu, *Physical Review B* **44**, 9812-9816 (1991).
- 42 G. Q. Lu, E. Nygren, and M. J. Aziz, *Journal of Applied Physics* **70**, 5323-5345 (1991).
- 43 F. A. Cotton and G. Wilkinson, 3rd ed. (Interscience, New York, 1972).
- 44 J. Narayan, *Journal of Applied Physics* **53**, 8607-8614 (1982).
- 45 L. Csepregi, E. F. Kennedy, T. J. Gallagher, J. W. Mayer, and T. W. Sigmon, *Journal of Applied Physics* **48**, 4234-4240 (1977).
- 46 E. F. Kennedy, L. Csepregi, J. W. Mayer, and T. W. Sigmon, *Journal of Applied Physics* **48**, 4241-4246 (1977).
- 47 J. C. McCallum, *Nuclear Instruments & Methods in Physics Research Section B-Beam Interactions with Materials and Atoms* **148**, 350-354 (1999).
- 48 K. T. Ho, I. Suni, and M. A. Nicolet, *Journal of Applied Physics* **56**, 1207-1212 (1984).
- 49 W. Barvosa-Carter, M. J. Aziz, A. V. Phan, T. Kaplan, and L. J. Gray, *Journal of Applied Physics* **96**, 5462-5468 (2004).
- 50 N. G. Rudawski and K. S. Jones, *Scripta Materialia* **61**, 327-330 (2009).
- 51 J. F. Sage, W. Barvosa-Carter, and M. J. Aziz, *Applied Physics Letters* **77**, 516-518 (2000).
- 52 J. S. Custer, M. O. Thompson, D. C. Jacobson, J. M. Poate, S. Roorda, W. C. Sinke, and F. Spaepen, *Applied Physics Letters* **64**, 437-439 (1994).
- 53 N. G. Rudawski, PhD thesis Thesis, University of Florida, 2008.
- 54 K. S. Jones, S. Prussin, and E. R. Weber, *Applied Physics a-Materials Science & Processing* **45**, 1-34 (1988).
- 55 N. Burbure, N. G. Rudawski, and K. S. Jones, *Electrochemical and Solid State Letters* **10**, H184-H185 (2007).

- 56 S. Morarka, N. G. Rudawski, M. E. Law, K. S. Jones, and R. G. Elliman, *Journal of Applied Physics* **105**, 053701 (2009).
- 57 A. V. Phan, T. Kaplan, L. J. Gray, D. Adalsteinsson, J. A. Sethian, W. Barvosa-Carter, and M. J. Aziz, *Modelling and Simulation in Materials Science and Engineering* **9**, 309-325 (2001).
- 58 J. A. Sethian, *Level set methods and fast marching methods : evolving interfaces in computational geometry, fluid mechanics, computer vision, and materials science*, 2nd ed. (Cambridge University Press, Cambridge, U.K. ; New York, 1999).
- 59 B. Drosd and J. Washburn, *Journal of Applied Physics* **51**, 4106-4110 (1980).
- 60 L. A. Marques, L. Pelaz, M. Aboy, L. Enriquez, and J. Barbolla, *Physical Review Letters* **91**, 135504 (2003).
- 61 L. A. Marques, L. Pelaz, J. Hernandez, J. Barbolla, and G. H. Gilmer, *Physical Review B* **6404**, 045214 (2001).
- 62 M. J. Tang, L. Colombo, J. Zhu, and T. D. delaRubia, *Physical Review B* **55**, 14279-14289 (1997).
- 63 L. Pelaz, L. A. Marques, M. Aboy, J. Barbolla, and G. H. Gilmer, *Applied Physics Letters* **82**, 2038-2040 (2003).
- 64 P. Rai-Choudhary, *Microlithography, Micromachining and Microfabrication*, Vol. 1, 1st ed. (SPIE-International Society for Optical Engineering, Bellingham, Washington, 1997).
- 65 L. Ren and B. Chen, in *Solid-State and Integrated Circuits Technology, 2004. Proceedings; Vol. 3* (2004).
- 66 Wikipedia, in http://en.wikipedia.org/wiki/Reactive-ion_etching, date accessed October 1, 2009.
- 67 Wikipedia, in http://en.wikipedia.org/wiki/Deep_reactive-ion_etching, date accessed October 1, 2009.
- 68 G. H. Kinchin and R. S. Pease, *Reports on Progress in Physics* **18**, 1-51 (1955).
- 69 D. R. Myers, R. G. Wilson, and J. Comas, *Journal of vacuum Science & Technology* **16**, 1893 (1979).
- 70 M. T. Robinson and I. M. Torrens, *Physical Review B* **9**, 5008-5024 (1974).
- 71 L. A. Christel, J. F. Gibbons, and T. W. Sigmon, *Journal of Applied Physics* **52**, 7143-7146 (1981).
- 72 K. S. Jones, D. K. Sadana, S. Prussin, J. Washburn, E. R. Weber, and W. J. Hamilton, *Journal of Applied Physics* **63**, 1414-1418 (1988).

- 73 J. G. Pellerin, D. P. Griffis, and P. E. Russell, *Journal of Vacuum Science & Technology B* **8**, 1945-1950 (1990).
- 74 H. Yamaguchi, A. Shimase, S. Haraichi, and T. Miyauchi, *Journal of Vacuum Science & Technology B* **3**, 71-74 (1985).
- 75 B. C. Johnson and J. C. McCallum, *Journal of Applied Physics* **96**, 2381-2385 (2004).
- 76 B. C. Johnson and J. C. McCallum, *Journal of Applied Physics* **95**, 4427-4431 (2004).
- 77 N. Bernstein, M. J. Aziz, and E. Kaxiras, *Physical Review B* **58**, 4579-4583 (1998).
- 78 F. Spaepen, *Acta Metallurgica* **26**, 1167-1177 (1978).
- 79 N. G. Rudawski, K. S. Jones, S. Morarka, M. E. Law, and R. G. Elliman, *Journal of Applied Physics* **105**, 081101 (2009).
- 80 J. Damiano, in *VLSI Tech* (1998), p. 212.
- 81 C. Zechner, D. Matveev, and A. Erlebach, *Materials Science and Engineering B-Solid State Materials for Advanced Technology* **114-15**, 162-165 (2004).
- 82 J. M. Jacques, K. S. Jones, L. S. Robertson, A. Li-Fatou, C. M. Hazelton, E. Napolitani, and L. M. Rubin, *Journal of Applied Physics* **98**, 073521 (2005).
- 83 P. J. Halfpenny, in *Journal of Materials Science: Materials in Electronics; Vol. 3* (Springer New York, 1992), p. 107-112.
- 84 L. B. Freund and S. Suresh, *Thin film materials*, 1st ed. (Cambridge University Press, Cambridge, UK, 2003).
- 85 R. Drosd and J. Washburn, *Journal of Applied Physics* **53**, 397-403 (1982).

BIOGRAPHICAL SKETCH

Saurabh Morarka was born in Jaipur, India. He attended the Bhartiya Vidya Bhavan's School in Jaipur from 1989 until 2001. He completed his Bachelor of Technology from Institute of Technology, Banaras Hindu University in electronics engineering in 2005. During the first year studies, he received award for academic excellence for four consecutive years. He then joined the University of Florida to study device and process simulations of Metal oxide semiconductor (MOS) devices. The graduate research involved amorphous regrowth, boron diffusion in silicon and effect of stress on regrowth.